



University of Bahrain

College of Science

Department of Physics

Characterization of Geomagnetic Pulsations in Corroboration with Solar wind Parameters

By: Amal Ali Marzooq

Student ID Number: 202003891

Supervised By:

Prof. Ashwini Kumar Sinha

This project report is submitted in partial fulfillment of the requirements for
the B.Sc. Degree at the Department of Physics At the

University of Bahrain

First Semester

ِفَاطِمَةَ، يَا ابْنَاهَا، يَبْعَلِمَهَا، يَبْنِيهَا
بِالسِّرِّ الْمُسْتَوْدِعِ فِيهَا

إِلَى السَّيِّدَةِ الزَّهْرَاءِ عَلَيْهَا السَّلَامُ

Abstract

The Earth's geomagnetic field is a vast and complicated system that requires the contribution of various fields and expertise in physics to explain its sophisticated couplings and fascinating events. Over the decades, space weather has significantly influenced our life on the planet Earth in numerous ways. Geomagnetic pulsations in the ultra-low frequency range (1 mHz to more than 10 Hz) are important to diagnose the continuously disturbed magnetic field of the Earth. This study aims to investigate the Sun-Earth coupling through observational evidence in geomagnetic ground stations and solar wind parameters collected by instruments onboard satellite at the L1 point. The features of the March 2015 intense solar storm phases showed a great agreement with the IMF B_z and the anti-sunward solar wind speed V_x variations. Pi2 signals were seen to overlap with a Pc4 pulsation during the SSC. The Pi2 pulsations were also observed and corroborated with the AL index as indicators of the initiation of the solar substorm expansion phase. A field line resonance feature was detected at the ground station Ascension (ASC) island on 16th of March Pc3 range data and exhibited the expected behaviour of decreasing power of pulsation of higher harmonics eigenfrequencies. The distribution of the continuous geomagnetic pulsations of Pc3, Pc4, and Pc5 have shown a subsolar bow-shock dominance suggesting that their origin is from direct solar wind pressure variations. The correlation of the solar wind parameters with the continuous pulsations waves amplitude using the Welch method showed a good dependence of amplitudes on the solar wind speed, IMF magnitude, and solar wind dynamic pressure with no significant distinction among the Pc3-Pc5 types.

Keywords: ULF waves, geomagnetic pulsations, solar storm, solar wind, Alfvén waves, compressional waves, magnetic local time, Welch method.

Acknowledgments

Here I stand, reflecting on the journey that shaped the older version of that enthusiastic physicist.

First and foremost I would like to thank God for all the blessings and guidance that this humble being has received throughout her entire life.

I want to express my gratitude towards my supervisor Prof Ashwini Kumar for all his sincere efforts throughout these semesters. He provided me with the best help and guidance that a student could get in a research journey. Thank you for teaching me how to be a good scientist!

I cannot forget the other amazing instructors who exposed me to the true beauty of my major: Dr Walid for his amazing and joyful classes, Dr Abdulmunem for all his care and kindness, Dr Khalil for his sincere efforts, Dr Jawad, for teaching me to view life through the lens of a physicist, Dr Karim for teaching me how to stand for my ideas and thoughts, and Dr Qurrat Ul Ain for being one of my life-changing instructors.

My friends! I would not have the best memories in my journey without being surrounded by you. Our shared joy, enthusiasm, and the challenges we overcame together are priceless to me.

And last but not least, my family! Thank you for providing me with the love and care to grow and become the person I am today. Thank you for all the things that are still in my heart, but I did not have the chance to share how I feel about them with you. Thank you from the depth of my heart!

Yes, written with eyes brimming with tears.

Table of Contents

1	Introduction	9
1.1	Origin of Earth's Geomagnetic Field	10
1.2	Earth's Magnetosphere Morphology	11
1.3	Current Systems	13
1.4	Magnetic Reconnection	14
1.5	Kelvin-Helmholtz Instability (KHI)	14
1.6	Solar Storms	15
1.7	Solar Substorms	16
1.8	The Magnetohydrodynamic (MHD) Model	17
1.8.1	Wave Modes and Dispersion Equation	18
1.9	Field Line Oscillations and String Analogy	20
1.9.1	Flux Tubes and Magnetic Disturbances	21
1.10	The Magic Resonant Frequencies	24
1.11	Ultra-Low Frequency Geomagnetic Pulsations	24
1.12	Aim of the Study	25
2	Methodology	27
2.1	Coordinate Systems	27
2.1.1	XYZ-Component System	28
2.1.2	HDZ-Component System	28
2.2	Magnetic Local Time (MLT)	28
2.3	Geomagnetic Indices	29
2.4	Data Selection and Constraints	29
2.5	Filters and Parameters	31
2.6	Pulsations Extraction Procedure	31
2.7	Solar Wind Parameters Fitting	32

3 Results and Discussion	33
3.1 Features of March 2015 Solar Storm	33
3.1.1 The Double Structure of the Storm Main Phase	33
3.1.2 The SSC and the Upstream Solar Wind Speed	35
3.1.3 Pi2s Associated with SSC	35
3.1.4 Pi2s as Substorms Precursor	37
3.2 Field Line Resonance Signature	37
3.3 Statistical Analysis of Continuous Pulsations	38
3.3.1 MLT Distribution of Pulsations	39
3.3.2 Parameters Analysis	40
4 Conclusion	45
Appendices	47
A The Ionosphere	49
A.1 Ionospheric Layers	50
B Other Coordinate Systems	51
B.1 The Dipole Coordinate System (r, θ, ϕ)	51
B.2 Local Magnetic Field-aligned Coordinates (v, μ, ϕ)	52
C Brief Introduction to Plasma Physics	53
C.0.1 What is a Plasma?	53
C.0.2 Plasma Motion	53
D The MHD Wave Equation	57
E EM Waves Reflection	61
F Digital Signal Processing (DSP)	65
F.1 Digitizing the Analog Signal	66
F.1.1 Nyquist Sampling Theorem	66
F.2 Signal Filtering	69
F.2.1 Low-pass Filter	69
F.2.2 High-pass Filter	69
F.2.3 Band-pass Filter	69
F.2.4 Band-stop Filter	70
F.3 Filters Characteristics	70
F.4 Smoothing and Noise Reduction	71

TABLE OF CONTENTS

7

F.5	Transforming Signals	71
F.6	FFT and STFT Algorithms	72
F.7	Welch's Method	73
G	Supplementary Codes	75

Introduction

The power transmission system ‘Quebec Interconnection’ one of the largest hydroelectric power producers on global demand, and the main power supplier in Canada (see Figure 1.1) had a 9 hours blackout on March 1989 (Heyns et al., 2020). This was the result of an intense geomagnetic storm that caused damage to the transmission lines via the geomagnetically induced currents on the ground. The hazardous effects of this storm were further extended as deficiencies in the power plants of the United States, United Kingdom, and Sweden during the main phase of the storm (Boteler, 2019). Although over 30 years have passed, this particular geomagnetic storm is still open for extensive research!

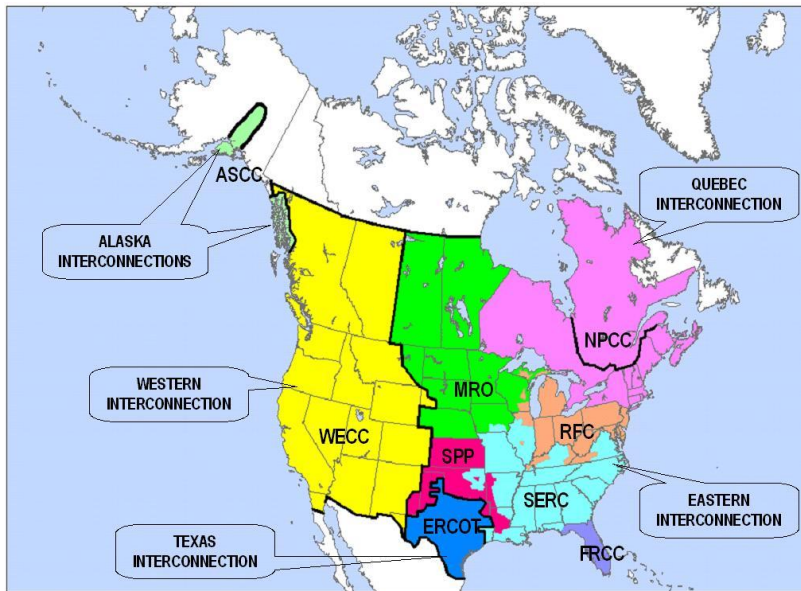


Figure 1.1: The transmission systems of the North American Electric Reliability Corporation. Source: en.wikipedia.org

This event -and many others- triggered a remarkable interest in the scientific community to study the space weather and the overall diagnostics of the gigantic geomagnetic field.

The versatility of the field and the complexity of the different systems and their coupling exhibit the essence of domain knowledge of different fields of physics to tip-toe the geomagnetic research ocean.

1.1 Origin of Earth's Geomagnetic Field

When one considers the problem of the Earth's magnetic field, many constraints arise because of the lack of understanding of its generation mechanism. To have an insight into the difficulty of this problem, we should look for its underlying challenges.

The interior of Earth's surface contains four main layers; the inner core, the outer core, the mantle and the crust (see Figure 1). The inner core contains solidified iron and other heavy elements under very high pressure and temperature¹ (Dormy, 2006).

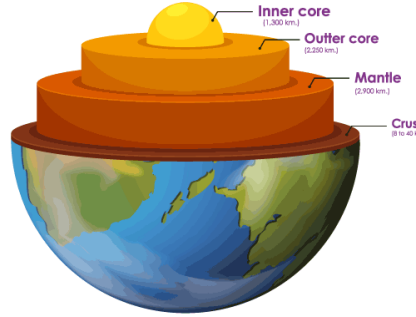


Figure 1.2: The four main layers of Earth. Source: byjus.com

The outer core's temperature can go as high as 3000° K, which way exceeds the Curie temperature². Another challenge yields from the Ohmic dissipation that suppresses electrical currents that are not sustained. The motion of the Earth around its axis generates the Coriolis force that together with Lorentz force affects the turbulence of molten iron. Another problem arises from the paleomagnetic evidence that the Earth's magnetic field reversed its direction several times in the past, making it harder for scientists to explain the generation mechanism of this magnetic field. To the best of the current knowledge, the dynamo theory explains the generation mechanism as the effect of interior convection of the molten iron inducing a magnetic field that is governed by the induction equation of the conductive fluid (Sisan et al., 2003):

$$\frac{\partial \mathbf{B}}{\partial t} = \eta \nabla^2 \mathbf{B} + \nabla \times (\mathbf{u} \times \mathbf{B}), \quad (1.1)$$

¹This high-temperature results from heat released upon the crystallization of some elements, the decay of radioactive sources, conversion of gravitational potential energy to thermal energy, etc.

²The Curie temperature is the temperature above which the ferromagnetic material loses its magnetic properties (i.e. where the magnetic moments are no longer aligned).

where B is the magnetic field, η is the magnetic diffusivity³, and u is the fluid center of mass velocity.

For the dynamo effect to maintain a magnetic field, the motion of the fluid must be strong enough compared to the viscous effects to overcome the magnetic dissipation. This is measured by the *Magnetic Reynolds Number*, defined as the ratio of the second term to the first term on the right-hand side of the induction equation (Uruba, 2018). The first term on the right-hand side is the advection of the magnetic field, while the second term is the diffusion of the magnetic field.

1.2 Earth's Magnetosphere Morphology

If the Earth were to be isolated from the solar system, the magnetosphere would have taken the shape of a dipole, which is spherically symmetric. However, the supersonic solar wind (about 400 km/s (Ganushkina et al., 2018)) forces the shape of the magnetosphere to be close to that of a comet. The solar wind is a supersonic bulk that transfers plasma, magnetic field, energy, and momentum to the Earth's magnetosphere. When it reaches the magnetosphere, a shock wave is formed upstream to the solar wind and a long tail that extends to a distance of $1000 R_E$ (Earth radii) called the "Magnetotail" is formed anti-sunward (Akay et al., 2019). The resulting shape is a magnetosphere that is compressed in the sunward direction (dayside) and elongated in the anti-sunward direction (nightside) as seen in Figure 1.3. The magnetosphere is in dynamic equilibrium and its boundary is decided by the balance between the pressure of the solar wind and the magnetic pressure of the geomagnetic field.

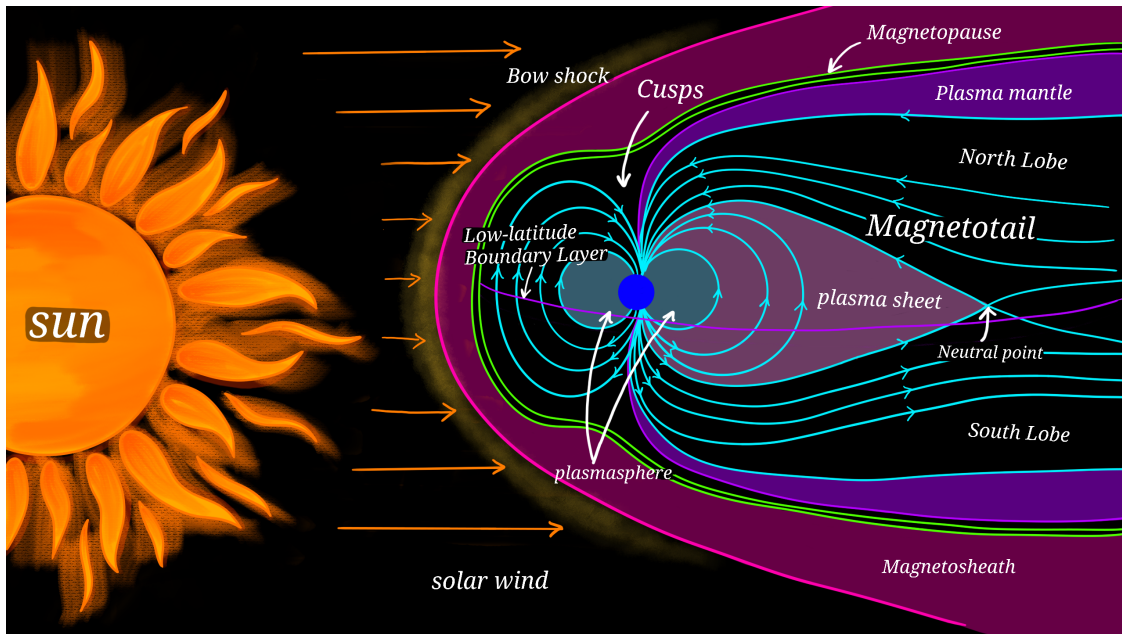


Figure 1.3: The different regions of the magnetosphere.

³notice that $\eta = 1/\sigma\mu$, where σ and μ are the electric conductivity and permeability respectively.

The magnetosphere consists of different important regions (shown in Figure 1.3). Each region has its own unique characteristics and role in some of the geomagnetic important events. These regions include (Borovsky & Valdavia, 2018):

- **Bow Shock:** is the region formed when the supersonic solar wind reaches the Earth's magnetic field, the cold plasma in the solar wind gets heated and energized and then deflects around the magnetosphere to be part of the magnetosheath.
- **Magnetopause:** is the most outer layer attached to Earth's magnetosphere.
- **Low Latitude Boundary Layer (LLBL):** is the low latitude plasma just inside the magnetopause.
- **Mantle:** the plasma layer in the high latitude region just inside the magnetopause.
- **Dipolar Region (or Inner Magnetosphere):** is the inner region of the magnetosphere where the geomagnetic field is predominantly dipolar having magnitude proportional to $1/r^3$, where r is the radial distance from the Earth's center.
- **Plasmasphere:** is the region above the ionosphere where dense cold plasma is in a doughnut shape around the Earth.
- **Plasma Sheet:** is the region anti-sunward where hot and dense plasma with closed magnetic field lines separates the North and South lobes.
- **North and South Lobes:** are the regions in the plasma sheet where the magnetic field lines connect to Earth at one end and to the interplanetary magnetic field on the other (Coxon et al., 2016).
- **Outer and Inner Radiation Belts:** are the regions where relativistic plasma (mostly of solar wind origin) is trapped at a high altitude in inner and outer doughnut-shaped regions (Houston, 2023) (see Figure 1.4).
- **Cusps:** are the magnetic null points regions near the North and South poles where solar wind plasma can penetrate and reach the Earth. Also, sometimes they are defined as the regions where the compressed dayside and elongated nightside magnetic fields come close to the geomagnetic dipole (Pitout & Bogdanova, 2021).

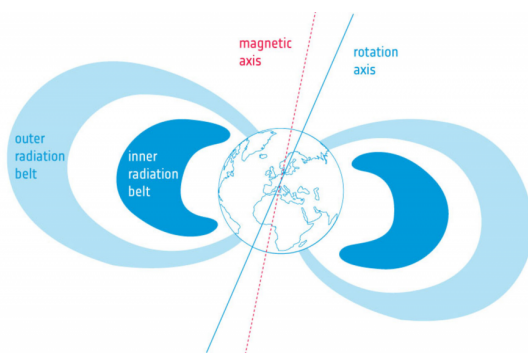


Figure 1.4: Van Allen radiation belts. Source: blogs.esa.int

1.3 Current Systems

The current systems of the Earth's magnetosphere play an important role in the transportation of charge, momentum, mass, and energy in the magnetosphere. These systems disturb the magnetic field by inducing additional magnetic fields, which ride over the ambient geomagnetic field as a response to any perturbation. In this section, the large-scale current systems are discussed briefly with the discussion relying extensively on (Ganushkina et al., 2018).

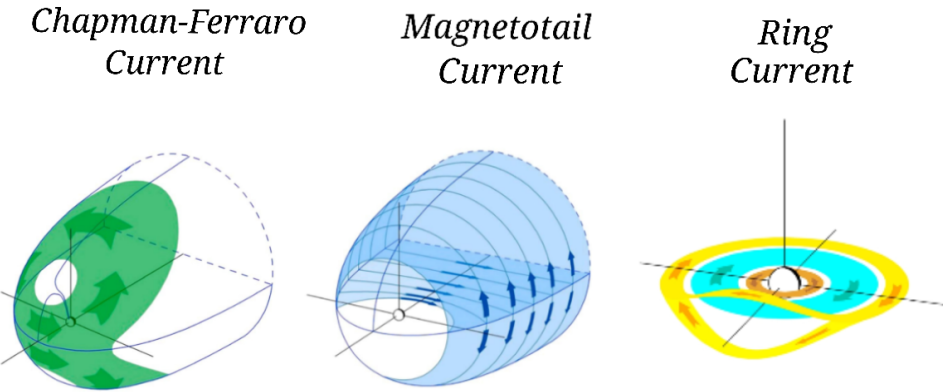


Figure 1.5: The large-scale current systems in the magnetosphere.

- **Chapman-Ferraro Magnetopause Currents:**

When the solar wind is at the bow shock, the pressure exerted by the solar wind plasma induces an extensive current called the *Chapman-Ferraro Current*. This current flows from dawn to dusk in the equatorial magnetopause and in the opposite direction at the high latitudes circulating the cusps of the geomagnetic field (see Figure 1.5).

- **Tail Current With the Return Current on the Magnetopause:**

The Greek letter θ shaped current flowing in the equatorial sheet that separates the Sunward magnetic field region and the anti-sunward magnetic field region. This field closes on the magnetopause with opposite circulation for both regions as seen in Figure 1.5.

- **Ring Current:**

The drifts of the particles in the magnetosphere result in the clockwise and the anti-clockwise ring current⁴. The dayside ring current splits into two branches while the nightside ring current flows on the same equatorial plane. This current system is shown in Figure 1.5.

⁴See Section 1.6 and Subsection C.0.2 in Appendix C for the details of its generation.

1.4 Magnetic Reconnection

Magnetic reconnection is one of the most important processes in the magnetosphere. It is responsible for the large-scale convection of plasma and is an essential stage for coupling mass, momentum, and energy during the solar wind-Earth interactions in the dayside magnetosphere.

When anti-parallel magnetic fields come close to each other they shear and merge in an x-shaped geometry heating and jetting the plasma away as illustrated in Figure 1.6.

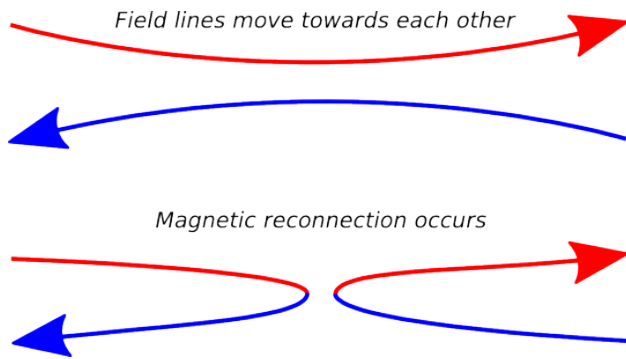


Figure 1.6: The magnetic reconnection of opposite magnetic field lines. Source: tumblr.com

When a Southward interplanetary magnetic field (IMF) encounters the Earth's magnetic field, a dayside magnetic reconnection opens the magnetic field lines energizing the plasma (the magnetic energy is converted into thermal energy) and convecting it to the nightside Magnetotail. Again, another reconnection occurs in the Magnetotail region energizing the plasma into much higher energy. The plasma is then convected along the field lines and goes through the injection process. A fraction of energy is also transported across the field by compressional waves which can couple with inner field lines to form the guided Alfvén waves propagating along the field line.

1.5 Kelvin-Helmholtz Instability (KHI)

A process with similar signatures of the magnetic reconnection is the Kelvin-Helmholtz instability (KHI). This instability occurs when the solar wind plasma reaches the bow shock, it gets slowed before it is heated and gradually increases its speed again reaching the solar wind velocity (Nykyri, 2024). The magnetosheath plasma will have much faster plasma compared to the plasma contained in the Earth's magnetosphere. Just like the surface waves on seawater, the KHI occurs when two fluids one is slow and the other is fast; shear causing a gradient in pressure on the boundary forming ocean-like waves. When a non-linear growth of pressure gradient evolves, the waves will roll up in vortices at the boundary. Figure 1.7 taken from (Gilbert, 2017) illustrates the process of KHI and the development of the vortices.

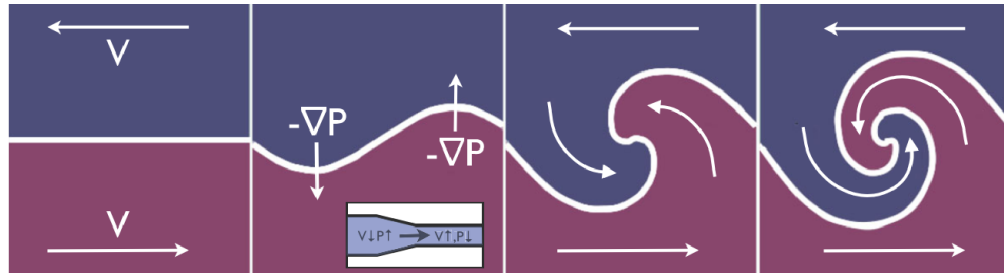


Figure 1.7: The steps for the formation of the Kelvin-Helmholtz wave.

Even though one wishes that the process is that easy, in reality, the KHI in the magnetosphere is much more complicated and contains turbulent cascades and secondary KHI. One method for energy dissipation of such waves would be through magnetic reconnection in small regions of the turbulence cascades near the flanks. Another way would be the tendency of the unstable non-Maxwellian plasma to grow waves upon any slight plasma disturbances.

Unlike the process of magnetic reconnection in Section 1.4, the initiation of the KHI does not require a Southward solar wind magnetic field. Both Southward and Northward IMF B_z showed to be inducing the KHI (Nykyri, 2024) in the dawn-dusk vicinity of the Earth. This suggests that this instability is responsible for the ultra-low frequency pulsations⁵ in the dawn-dusk regions.

1.6 Solar Storms

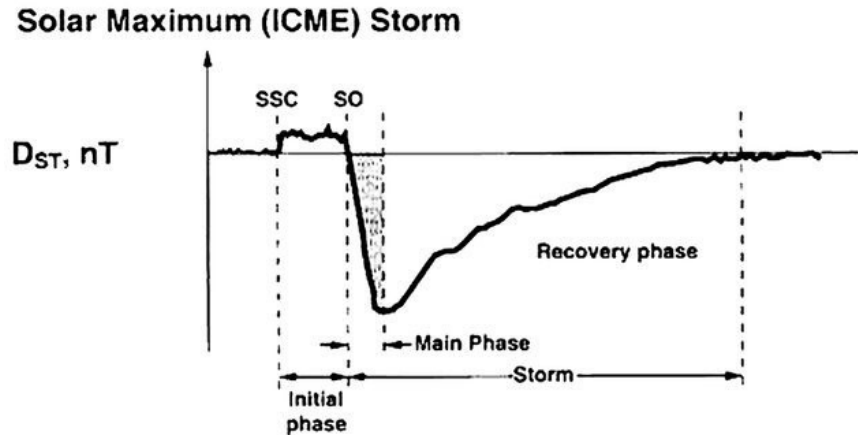


Figure 1.8: The different phases of the solar storm. Source: (Singh, 2019)

After the occurrence of the Magnetotail reconnection as discussed in Section 1.4, it should be noted that sometimes the plasma particles acquire a very high energy allowing them to propagate across the field lines of the Earth. As they propagate across the magnetic field lines, they experience a grad B force ($\vec{\nabla}B$) that will make them drift around

⁵These pulsations will be discussed in Section 1.11.

the Earth creating a current called *ring current*. This current will decrease the horizontal component of the Earth's magnetic field (Ganushkina et al., 2018) generating a geomagnetic storm. The phases of the solar storm are shown in Figure 1.8 and are adapted from (Kamide et al., 1998).

- **Storm Sudden Commencement (SSC):**

When the supersonic solar wind exerts pressure on the magnetopause, it enhances the currents in the magnetosphere which will induce additional fields. This results in the increase of the horizontal component of the geomagnetic field seen as a positive bay. This process is called *the storm sudden commencement (SSC)*.

- **Initial Phase:**

During this phase, the continuous pressure of the solar wind leads to a sudden increase in the horizontal component of the magnetic field from its value prior to the SSC.

- **Main Phase:**

An intense decrement of the H component of the geomagnetic field starts with the storm onset (SO) as the result of the enhanced westward ring current in the equatorial region. The solar storms are classified based on the minimum value of the Dst index⁶ during the main phase as: (Dst > -50 nT) is weak, (-50 > Dst > -100 nT) is moderate, and (Dst < -100 nT) is intense.

- **Recovery Phase:**

When the IMF B_z turns Northward, then the recovery phase initiates. This causes the ring current to gradually decay, and the H component of the magnetic field to return to its pre-storm value. This phase can last for several days. It is worth noting that the ULF pulsations⁷ are dominant during the recovery phase of the solar storm.

The phases of the different solar storms are similar, except that not all solar storms have SSC and initial phase.

1.7 Solar Substorms

Solar storms necessarily have substorms associated with them -not to confuse this with the fact that they are different phenomena⁸- . The main phases of a substorm are the growth phase, the expansion phase, and the recovery phase (Rostoker et al., 1980). Insights in this section are derived based on (D. N. Baker et al., 1996).

- **Growth Phase:**

It is defined by the enhancement of magnetic energy accumulation in the magnetotail (as loading of magnetotail lobes flux) due to the solar wind-Earth interaction. This interaction is a result of Southward IMF causing a reconnection at the subsolar region. This allows the elongation of the magnetotail making the magnetosphere unstable and causing compressional waves and shear plasma flows to propagate in the magnetosphere (Song & Lysak, 2023).

⁶The geomagnetic indices will be discussed in Section 2.3.

⁷That will be discussed in Section 1.11

⁸i.e. we can have substorms without the occurrence of a solar storm.

- **Expansion Phase:**

Observations showed that the plasma of the plasma sheet propagates tailwards as a *plasmoid* making the near-Earth field more dipolar and thinning the plasma sheet. Near Earth, reconnection causes explosive dissipation when particles are accelerated and injected into the auroral regions, and ring current injection initiates.

- **Recovery Phase:** In this phase, the unloading process starts to recover the negative bays by rapid thickening of the plasma sheet which eventually returns the magnetosphere to its original state.

1.8 The Magnetohydrodynamic (MHD) Model

The general behaviour of plasma⁹ can be explained when it is assumed to be a conducting fluid under adiabatic conditions (no energy transfer by heat)¹⁰ and having a frequency much lower than the smallest ion species frequency present ($\omega_i \gg \omega_p$). These assumptions result in the MHD equations (Koskinen & Kilpua, 2021):

The Continuity Equation:

$$\frac{\partial \rho_m}{\partial t} + \vec{\nabla} \cdot (\rho_m \vec{V}) = 0, \quad (1.2)$$

The Equation of State:

$$\frac{d}{dt} \left(\frac{\vec{P}}{\rho_m^\gamma} \right) = 0 \rightarrow \vec{P} = C \rho_m^\gamma, \quad (1.3)$$

The Equation of Motion:

$$\rho_m \left(\frac{\partial \vec{V}}{\partial t} + (\vec{V} \cdot \vec{\nabla}) \vec{V} \right) = \vec{J} \times \vec{B} - \vec{\nabla} P, \quad (1.4)$$

Ampere's Law:

$$\vec{\nabla} \times \vec{B} = \mu_0 \vec{J}, \quad (1.5)$$

Faraday's Law:

$$\vec{\nabla} \times \vec{E} = - \frac{\partial \vec{B}}{\partial t}, \quad (1.6)$$

Ohm's Law:

⁹A brief introduction to plasma physics is explained in Appendix C.

¹⁰This can only be a valid approximation if the plasma motion was perpendicular to the magnetic field.

$$\vec{E} + \vec{V} \times \vec{B} = \eta \vec{J}, \quad (1.7)$$

Where ρ_m is the mass density, \vec{V} is the centre of mass velocity, \vec{P} is the pressure, γ is the ratio of the specific heat under constant pressure to the specific heat under constant volume (C_p/C_v), \vec{J} is the current density, \vec{B} is the magnetic field, \vec{E} is the electric field, η is the resistivity, and μ_0 is the permeability of free space.

Using these equations, one can derive the MHD wave equation¹¹:

$$\boxed{\frac{\partial^2 \vec{v}}{\partial t^2} - v_s^2 \vec{\nabla}(\vec{\nabla} \cdot \vec{v}) + v_A \times (\vec{\nabla} \times \vec{\nabla} \times \vec{v} \times v_A) = 0} \quad (1.8)$$

where \vec{v} is the velocity perturbation, v_s is the speed of sound, and $v_A = \vec{B}_0 / \sqrt{\mu_0 \rho_0}$ is the *Alfven velocity*.

1.8.1 Wave Modes and Dispersion Equation

When the perturbations are assumed to have planar wave variations ($\sim e^{i(\vec{k} \cdot \vec{r} - \omega t)}$), the wave equation in Equation (1.8) gives¹²:

$$\boxed{-\omega^2 \vec{v} + \vec{k}(\vec{k} \cdot \vec{v})(v_s^2 + v_A^2) - (\vec{k} \cdot v_A) [\vec{k}(v_A \cdot \vec{v}) - \vec{v}(\vec{k} \cdot v_A) + v_A(\vec{k} \cdot \vec{v})] = 0} \quad (1.9)$$

which is the *Dispersion Equation* of ideal MHD waves.

It is worth noting that if the angular frequency of the plasma waves (ω) is complex, the imaginary part determines whether the wave will be unstable and exponentially grow (if $\text{Im}(\omega) > 0$) or if it will be damped as it loses energy overtime (if $\text{Im}(\omega) < 0$) (Anderson, 1990).

Now, following (Chen, 1984) and (Koskinen & Kilpua, 2021) to find some of the types of waves present under the planar velocity perturbation assumption:

Parallel to B_0 Propagation

When the wave propagates parallel to the unperturbed magnetic field B_0 , two waveguide modes exist.

- When the perturbation velocity is parallel ($\vec{v} \parallel \vec{B}_0 \parallel \vec{k}$):

$$-\omega^2 \vec{v} + k^2 \vec{v} (v_s^2 + v_A^2) - k^2 v_A^2 \vec{v} = 0 \rightarrow -\omega^2 \vec{v} + k^2 v_s^2 \vec{v} = 0,$$

¹¹The derivation is discussed in Appendix D.

¹²The identity $A \times B \times C = B(A \cdot C) - C(A \cdot B)$ was applied twice.

$$\boxed{\frac{\omega}{k_{||}} = v_s} \quad (1.10)$$

which is a *sound wave*.

- When the perturbation velocity is perpendicular ($\vec{v} \perp \vec{B}_0 \parallel \vec{k}$):

$$-\omega^2 \vec{v} + \vec{v}(kv_A)^2 = 0,$$

$$\boxed{\frac{\omega}{k_{||}} = v_A} \quad (1.11)$$

which is the *Alfven wave* (or *shear Alfven wave*).

Perpendicular to B_0 Propagation

In this case ($\vec{v} \parallel \vec{k} \perp \vec{B}_0$) the wave mode takes the following dispersion relation:

$$-\omega^2 \vec{v} + k^2 v(v_s^2 + v_A^2) = 0,$$

$$\boxed{\frac{\omega}{k_{\perp}} = \sqrt{v_s^2 + v_A^2}} \quad (1.12)$$

which is a *compressional wave* (or, *fast Alfven wave*).

Oblique Propagation

Since the problem is three-dimensional, only the final result is presented here¹³:

$$\boxed{\frac{\omega}{k} = v_A \cos \theta} \quad (1.13)$$

this can be considered as a generalization for the *shear Alfven wave* with an angle relative to B_0 .

In reality, the ambient field in the inner magnetosphere cannot be assumed homogeneous nor the perturbations be of planar waveform. Hence, the wave equation becomes very hard to solve analytically.

On the other hand, if standing waves of perfectly transverse perturbations were assumed, the solution yields two modes of oscillations: toroidal mode, and poloidal mode. These modes will be further discussed in the next section.

¹³You can refer to (Koskinen & Kilpua, 2021) for the derivation.

1.9 Field Line Oscillations and String Analogy

To have a physical intuition of what is going on in the magnetosphere, it is useful to start with the simple physics of a musical chord. Be noted that the content of this section primarily stems from (Anderson, 1990).

In a guitar, for instance, the two ends of the chord are fastened in such a way that the tension in each chord leads to different sound wave frequencies. This is because the waves along the cord perturb the air molecules and these perturbations get amplified by the cavity of the guitar travelling as an audible sound wave. An exaggerated illustration of waves along the chords is shown in Figure 1.9.

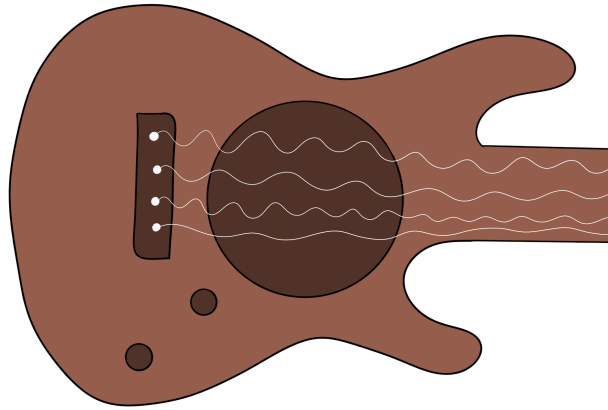


Figure 1.9: The different waves supported by the musical chords.

The wave equation for the disturbances of the musical cord is:

$$\frac{\partial^2 \psi}{\partial x^2} - \frac{1}{v^2} \frac{\partial^2 \psi}{\partial t^2} = 0, \quad (1.14)$$

where ψ is the disturbance function, and v is the speed of the wave given by $v = \sqrt{T/\rho}$ where T is the tension force, and ρ is the linear mass density along the chord.

When there is a wave moving along the chord in one direction, and another wave moving in the opposite direction, the superposition of the two waves results in destructive interference when the peak of one wave adds up with a valley of another. On the other hand, a constructive interference occurs when two peaks add up as shown in Figure 1.10.

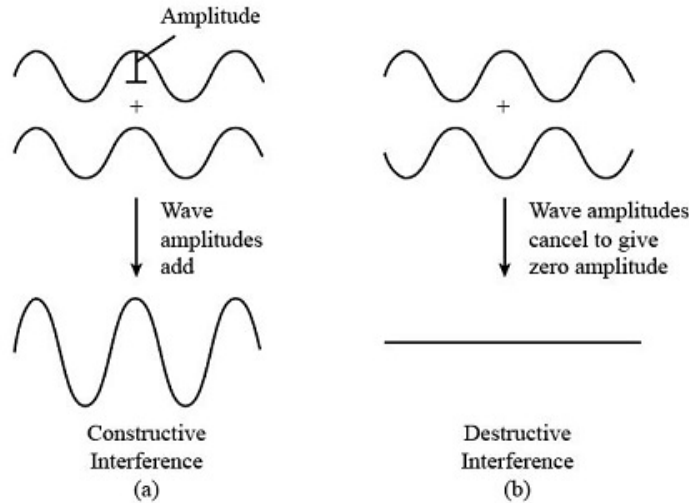


Figure 1.10: The superposition of waves. Source: homework.study.com

A special case of such waves interfering can occur when the interference yields a stationary appearing wave called a *standing wave*. These standing waves occur at discrete frequencies called *resonant frequencies* or *eigen frequencies* that obey the following condition:

$$f_n = \frac{nv}{2l}, \quad (1.15)$$

where n is an integer representing the harmonic of the oscillation ($n = 1, 2, 3, \dots$), and l is the length of the chord.

Likewise, a similar model can now be applied to the magnetosphere. Assuming a dipolar magnetic field with the field-lines represented as flux tubes -frozen in plasma concept- that do not interact with each other (i.e. a perturbation in a magnetic field-line does not affect the ones nearby¹⁴). The infinitely conductive field lines are assumed to be fastened in the Northern and Southern poles at the ionosphere¹⁵, where it is assumed to have an infinite conductivity ($\sigma \rightarrow \infty$) under the *equinoctial* boundary condition¹⁶. This assumption makes the ionosphere act like a perfectly reflecting mirror¹⁷ where no waves can propagate through (i.e. no energy loss).

1.9.1 Flux Tubes and Magnetic Disturbances

The relationship between the flux tube displacement and the resulting magnetic perturbation using Ohm's law in Equation (1.7) under the same assumption of infinite conductivity,

¹⁴Although in reality, this assumption is not possible.

¹⁵See Appendix A for further details on the ionosphere.

¹⁶Other boundary conditions also exist, like the *free-end* solstice condition when the inclination of the Earth's rotation axis is taken into account, making only one end to have $\sigma \rightarrow \infty$.

¹⁷Refer to Appendix E for the discussion of EM waves reflection from a perfectly conducting boundary.

$$\vec{E} = -\vec{v} \times \vec{B}_0 \rightarrow \vec{E} = -\frac{\partial \vec{\xi}}{\partial t} \times \vec{B}_0.$$

Where $\vec{\xi}$ is the field line displacement or the perturbation of the flux tube.

Now, taking the curl of both sides and using Faraday's law in Equation (1.6),

$$\vec{\delta b} = B_0 \frac{\partial \vec{\xi}}{\partial s}, \quad (1.16)$$

where s is the direction along which the wave propagates.

The perturbations of the electric field can also be found in the disturbance of the flux tube directly from Ohm's law as:

$$\vec{E} = -\frac{\partial \vec{\xi}}{\partial t} \times \vec{B}_0. \quad (1.17)$$

It is worth noting that the magnetic field disturbance and the induced electric field are 90° out of phase. Notice that Equation (1.16) implies that when ξ disturbance has a local maximum, then the magnetic field perturbation has a node. This can visually be seen in Figure 1.11.

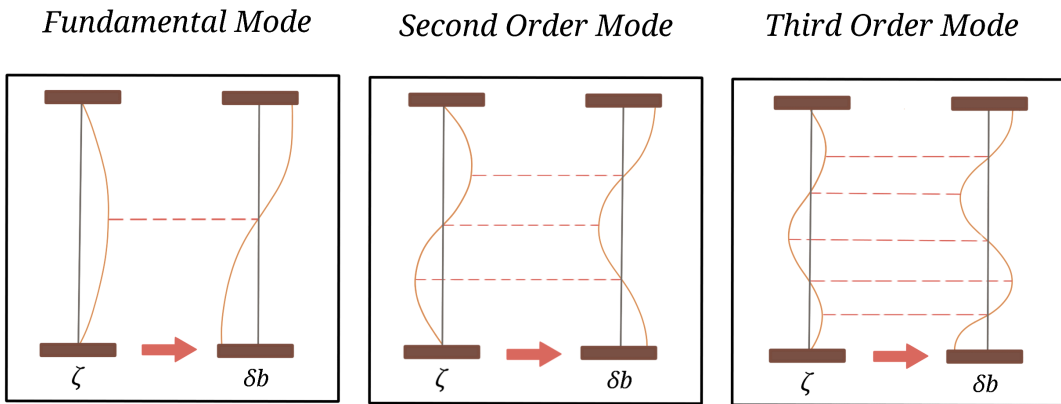


Figure 1.11: The disturbances in the field-line and their reflection on the magnetic field disturbance.

This demonstrates that when the oscillation modes are odd (symmetric modes), there is a node in magnetic field perturbation at the equator, and when the modes are even (asymmetric modes), there is an anti-node in the magnetic field perturbation at the equator. In other words, if the measurements of the magnetic field variation along a line of stations of the same magnetic longitude showed very low amplitudes of fundamental mode waves at equatorial regions, then one can deduce that the source of disturbance is at the equator!

Now, since only the transverse Alfvén waves are of interest in this discussion, the plasma pressure term (the second term) in the ideal MHD wave equation in Equation (1.8) can be neglected:

$$\frac{\partial^2 \vec{v}}{\partial t^2} + v_A \times (\vec{\nabla} \times \vec{\nabla} \times \vec{v} \times v_A) = 0.$$

Taking the cross product of the equation with B_0 ,

$$\frac{\partial^2}{\partial t^2} (\vec{v} \times \vec{B}_0) - v_A \times v_A \times \vec{\nabla} \times \vec{\nabla} \times (\vec{v} \times \vec{B}_0) = 0,$$

Using Ohm's law, we get the wave equation in \vec{E} :

$$\frac{\partial^2 \vec{E}}{\partial t^2} - v_A \times v_A \times \vec{\nabla} \times \vec{\nabla} \times \vec{E} = 0. \quad (1.18)$$

Notice the similarities between this wave equation and the wave equation in Equation (1.14)¹⁸.

Now, to get a solution for such an equation, a *perfectly* transverse wave must be assumed with two extrema¹⁹ depending on the azimuthal²⁰ wave number (\vec{k}_ϕ):

- **Poloidal mode:** when the oscillation is mainly radial δb_v and \vec{E}_ϕ ($k_\phi \rightarrow 0$).
- **Toroidal mode:** when the oscillation is mainly azimuthal δb_ϕ and \vec{E}_v ($k_\phi \rightarrow \infty$).

These oscillation modes are shown in Figure 1.12.

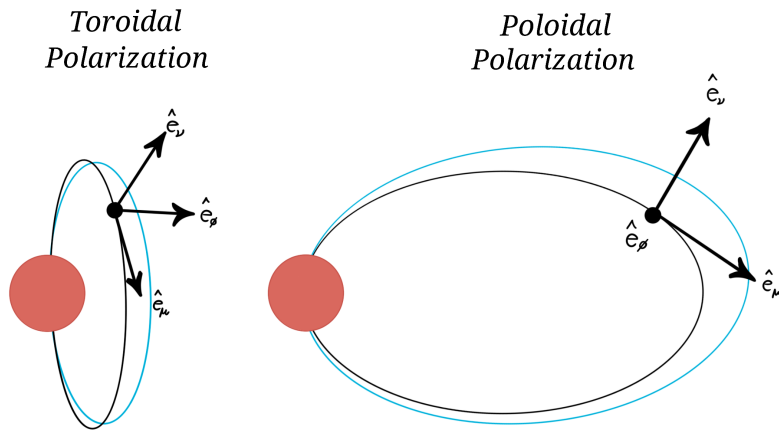


Figure 1.12: The fundamental mode of the poloidal and toroidal oscillations. Notice that here \hat{e}_i refers to the unit vector in the i th direction of field line disturbance and *not* to the direction of electric field perturbation.

¹⁸Although this equation is much more complicated!

¹⁹If this assumption was not introduced, both polarization modes will be coupled.

²⁰See Section B.2 in Appendix B for the local magnetic field-aligned coordinates.

Just like the chord of a guitar, this cavity supports eigenfrequencies as in Equation (1.15) with the exception that here the Alfvén velocity is introduced:

$$f_n = \frac{nv_A}{2l} = \frac{nB_0}{2l\sqrt{\mu_0\rho_m(r)}}, \quad (1.19)$$

where $\rho_m(r)$ is the plasma mass density along the field line and is the function of the radial distance r from the Earth's centre.

Now, the complexity of finding these exact eigenfrequencies becomes evident as $\rho_m(r)$ is usually represented by numerical model (Hruška, 1969) as $\rho_m(r) = \rho_{m_0}(r/r_0)^q$ where ρ_{m_0} is the linear mass density at the equator, r_0 is the equatorial distance to the field line, and q is a number determined by the model.

1.10 The Magic Resonant Frequencies

There are many sources of geomagnetic disturbances categorized into direct energy transfer from *magnetic reconnection* (Dungey, 1961), *sudden impulse of solar wind dynamic pressure* (Sinha & Rajaram, 2014), *solar wind-magnetosphere interactions* and the *plasma instabilities* (e.g. the Kelvin-Helmholtz instability near the flanks (Southwood, 1968)) in the magnetosphere (Anderson, 1990). Earlier studies of ultra-low frequency geomagnetic disturbances showed that there are seemingly preferred excitation frequencies (these frequencies have typical values of few mHz (Sinha et al., 2005), (Kepko et al., 2002)) of field-line resonances (Kivelson & Southwood, 1985). This was later explained by a global cavity model (Kivelson & Southwood, 1986) where compressional waves are contained between the magnetopause and an inner magnetospheric layer (e.g. the equatorial ionosphere). The coupling between the global cavity modes and the individual field-line resonances causes some resonant frequencies to decay and others to be sustained. Another well-established study in later years showed that these magic frequencies astonishingly align with the solar wind dynamic pressure frequency (Kepko et al., 2002) proving the association of solar wind events with geomagnetic disturbances.

1.11 Ultra-Low Frequency Geomagnetic Pulsations

The ultra-low frequency (ULF) variations (from 1 mHz to greater than 10 Hz (Moura et al., 2023)) of the geomagnetic field are called *geomagnetic pulsations* or sometimes *micro pulsations*. The semi-sinusoidal continuous variations are named *continuous geomagnetic pulsations* (Pcs) and are categorized as Pc1, Pc2, Pc3, Pc4, and Pc5 depending on their frequencies as shown in Table 1.1 taken from (Kozlovskaya & Kozlovsky, 2012). On the other hand, the irregular variations of the geomagnetic field are called *irregular pulsations* and are typically categorized as Pi1 and Pi2 pulsations based on their corresponding frequencies in Table 1.1. It is worth noting that Pi and Pc waves can also overlap (eg. during the SSC and the positive magnetic bays) (Kamide et al., 1998).

Pulsations	T (s)	f	Amplitudes (nT)
Pc1	0.2–5	0.2–5 Hz	0.01–0.1
Pc2	5–10	0.1–0.2 Hz	0.1–1
Pc3	10–45	22–100 mHz	1–10
Pc4	45–150	7–22 mHz	5–50
Pc5	150–600	2–7 mHz	50–500
Pi1	1–40	0.025–1 Hz	0.2–1
Pi2	40–150	2–25 mHz	10–100

Table 1.1: The characterizing values of geomagnetic pulsations.

1.12 Aim of the Study

As the ULF waves represent the response of the Earth's magnetic field to any external or internal disturbing variations, they are often used to diagnose the magnetosphere during the disturbance by assessing the plasma density, which is closely related to the observed frequency. Hence, study of geomagnetic pulsations in terms of ULF waves is an integral part of *Space Weather Research*.

This study aims to highlight the observational evidence of the influence of solar wind on geomagnetic events like the intense solar storm. Then, the focus will shift to investigate the overall distribution of Pcs and correlate them with the solar wind parameters; as only a few studies of the equatorial region (like (Liu et al., 2009) and (Bulusu et al., 2020)) try to quantify their corroboration as a potential method to distinguish their different -but poorly understood-generation mechanisms.

Chapter 2

Methodology

2.1 Coordinate Systems

Defining a unified coordinate system is the first step for any collaborative work. There exist some conventions for data collection among geomagnetic stations defined by the *International Association of Geomagnetism and Aeronomy* (*IAGA*).

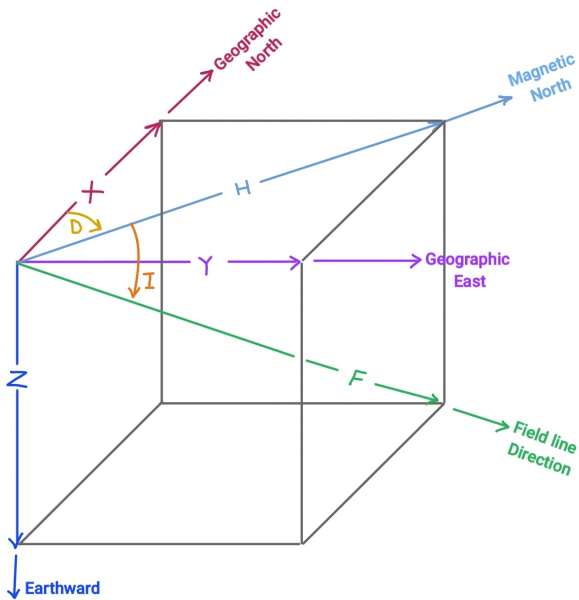


Figure 2.1: The magnetic coordinate systems in use by the geomagnetic stations.

The two frequently used right-handed magnetic coordinate systems are the XYZ-component, and the HDZ-component systems (Takahashi & Heilig, 2019) shown in Figure 2.1 re-drawn from (Campbell & Banerjee, 1998).

2.1.1 XYZ-Component System

This system has X, Y, and Z components of the magnetic field (XYZ-component), where the X positive direction is along the geographic North direction, Y positive direction is along the geographic East direction, and Z is along the downward direction towards the Earth.

2.1.2 HDZ-Component System

The HDZ coordinate system involves the H, D, and Z components of the magnetic field (HDZ-component), where H is the horizontal component of the magnetic field (towards the geomagnetic North), D is the declination angle measured from the geographic North to the geomagnetic North, and the Z component is towards the Earth.

Another often used angle is the *declination angle* (*I*) sometimes called the *dip angle*, which is the angle of Earth's magnetic field with the horizontal.

From simple trigonometry, the conversion between both systems is as follows:

$$X = H \cos(D),$$

$$Y = H \sin(D),$$

$$F = \sqrt{X^2 + Y^2 + Z^2} = \sqrt{H^2 + Z^2},$$

$$I = \tan^{-1} \left(\frac{Z}{H} \right),$$

$$H = \sqrt{X^2 + Y^2},$$

$$D = \tan^{-1} \left(\frac{Y}{X} \right).$$

2.2 Magnetic Local Time (MLT)

Another well-known system of 24 hours starting from the midnight sector is called the *magnetic local time* (MLT) and is used to represent the time relative to the Sun. An hour in this system measures 15° in geomagnetic longitude (Laundal & Richmond, 2016). There exist many models to compute the MLT, but the most straightforward one is given by (K. B. Baker & Wing, 1989) as:

$$\text{MLT} = \text{UT} + \frac{(\phi + \Phi_N)}{15}, \quad (2.1)$$

Where ϕ is the geomagnetic longitude, Φ_N is the geographic longitude of the geomagnetic North pole in a centred dipole coordinate, and UT is the universal time.

2.3 Geomagnetic Indices

Geomagnetic indices are used to describe the activity of the geomagnetic field upon transient variations. Recognized indices by the IAGA (International Association of Geomagnetism and Aeronomy) include Kp, Ap, Cp, AL, AU, AE, Dst, SYM-H, and more, which are currently in use for different purposes. Some of these indices are of interest in this study. These indices are available online in *WDC for Geomagnetism, Kyoto* website.

Based on the descriptions provided by (*GEOMAGNETIC INDICES BULLETIN*, 2010) and (Mayaud, 1980), the Kp, Dst, and auroral indices are introduced in this section.

- **The Kp Index:**

The K index is a 3-hour index of the disturbed H-component of the magnetic field related logarithmically to the amplitude. The value of the K index ranges from 0 (for the least disturbed) to 9 (for the most disturbed). The Kp index is the average of the K index of 11 sub-auroral stations.

- **The Dst Index:**

The disturbance storm time index (Dst) provides an hourly measure of the equatorial region H-component averaged from 4 equatorial geomagnetic stations.

- **The Auroral Indices (AU, AL, AE):** The auroral indices are used for the auroral region disturbances of the H-component of 12 stations in the Northern Hemisphere. A baseline of the average of the five quietest days of the month is subtracted from the 1-minute data of the H-component recorded. The AU index represents the Eastward electrojet, the AL index represents the Westward electrojet, and the AE index is the difference between the AU and AL indices. It should be noted that a geomagnetic storm is described by the Dst index while the solar substorm is described by the auroral indices AL, AU and AE.

2.4 Data Selection and Constraints

For the basics of digital signal processing (DSP), you are highly encouraged to read Appendix F.

The data used in this study is taken from the global network of observatories INTERMAGNET. Four longitudinally distributed stations (refer to Table 2.1 for the stations coordinates) are selected to span the days 14-18 of March 2015. The conversion from geographic to geomagnetic coordinates is performed using the World Data Center for

Geomagnetism, Kyoto (WDC, Kyoto). The analysis and plots in this study are done using Python programming language in Jupyter Notebook¹.

Station	Geomagnetic Latitude	Geomagnetic Longitude
GUAM (GUA)	5.76N	143.51W
DALAT (DLT)	2.19N	178.93W
ASCENSION Island (ASC)	2.73S	57.47E
KOUROU (KOU)	14.27N	20.46W

Table 2.1: The coordinates of the four geomagnetic stations.

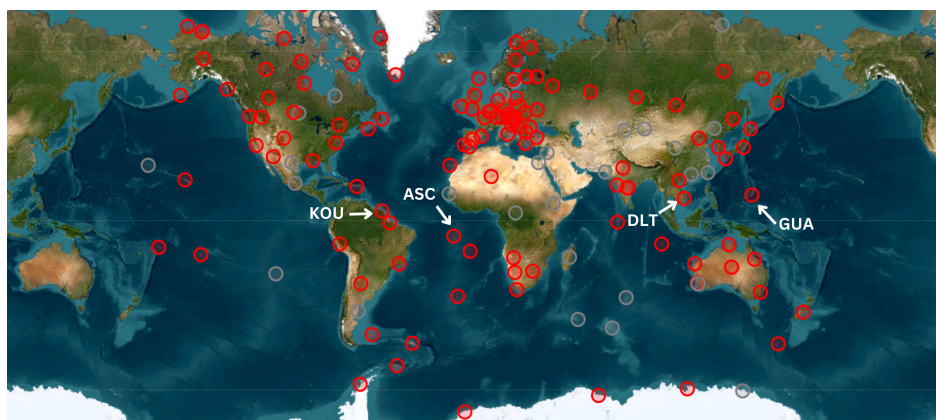


Figure 2.2: The geomagnetic stations on the map. Source: INTERMAGNET.

The stations are selected based on their relative distribution and data availability collected at 1 Hz sampling frequency for the days mentioned above. A map showing these stations is in Figure 2.2. The selection of dates is made to constrain a few pre-storm days and the main phases of the storm. The plot showing the Dst index of the storm is shown in Figure 2.3.



Figure 2.3: The Dst index data plot of March 2015. The storm phases are highlighted in yellow.

¹ You can find the full code in Appendix G.

Since the original sampling frequency is 1 Hz, the information that could be extracted from the data must have frequencies less than 0.5 Hz following the Nyquist criteria². Hence, according to Table 1.1, high-quality information can be obtained for the Pc3, Pc4, Pc5, and Pi2 pulsations only.

The solar wind parameters (i.e. IMF magnetic field magnitude, solar wind velocity, dynamical pressure³, and the solar wind temperature) of 1-minute resolution is taken from *omniweb.gsfc.nasa.gov* which provides time-shifted data to the Earth's bow shock nose based on ACE, Wind and IMP 8 spacecraft.

2.5 Filters and Parameters

It is a common practice in ULF waves analysis to use the Butterworth filter⁴ with different orders. In this study, a Butterworth filter of order 4 is used. The short-time Fourier transform (STFT) is performed using the following parameters: $f_s = 1$ Hz, $n_{\text{fft}} = 512$, and $n_{\text{overlap}} = 230$.

2.6 Pulsations Extraction Procedure

For a pulse to be recorded as a continuous pulsation, a minimum of three cycles is required to record the pulsations of threshold amplitude:

- ($\text{kp} < 4$, Quiet): $\text{pc3} = 0.1$ nT, $\text{pc4} = 0.3$ nT, and $\text{pc5} = 0.5$ nT.

The choice of these amplitudes is made to prevent pulses from being misclassified due to ambient fluctuations. It is worth noting that there are no fixed standards of threshold amplitudes in the literature, and the values are determined based on visual inspection of pulses.

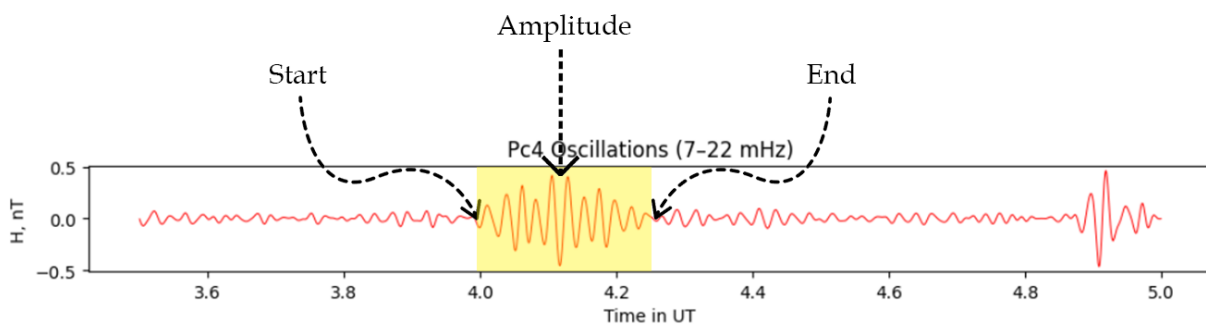


Figure 2.4: The method of recording the pulsations.

For each pulse, the beginning, the end, and the median amplitude are recorded (see Figure 2.4). The Kp index and the MLT assigned to each pulse are based on the central point of the pulse. This method will solely be used for counting

²See Subsection F.1.1 in Appendix F.

³Which is defined as $P = \frac{1}{2}\rho V_x^2$.

⁴Either as a low-pass filter for reducing the high-frequency noise, or as a band-pass filter for each class (see Section F.2 in Appendix F).

the pulsations and investigating their distribution around the Earth.

2.7 Solar Wind Parameters Fitting

To fit the solar wind parameters with the Pcs, the Welch method⁵ is applied on every 1-hour segment with 512 overlapping⁶ data points at 1 Hz sampling frequency of ASC station. The magnitude of the IMF, the speed of the solar wind, the dynamical pressure, and the plasma temperature are averaged over the period of each segment (1 hour). This method is followed by (Liu et al., 2009) where the amplitude of the magnetic field disturbance is determined as in the following equation:

$$\delta B = \sqrt{\int_{f_1}^{f_2} PSD_B(f)df}, \quad (2.2)$$

where f_1 and f_2 are the minimum and maximum frequencies of each Pc type range.

Using this method of fitting avoids the significant impact of human error in quantifying the correlations.

⁵see Section F.7 in Appendix F.

⁶The choice of the number of data points was made to capture the periodicity of signals.

Chapter 3

Results and Discussion

3.1 Features of March 2015 Solar Storm

The phases of the geomagnetic storm discussed in 1.6 can be seen in March's 2015 storm in Figure 3.1. This geomagnetic storm is classified as an intense solar storm with a minimum Dst of -234 nT. The SSC started on the 17th of March 2015 at around 4.8 UT. The initial phase is not clear in the Dst plot due to the 1-Hour resolution of the Dst index¹.

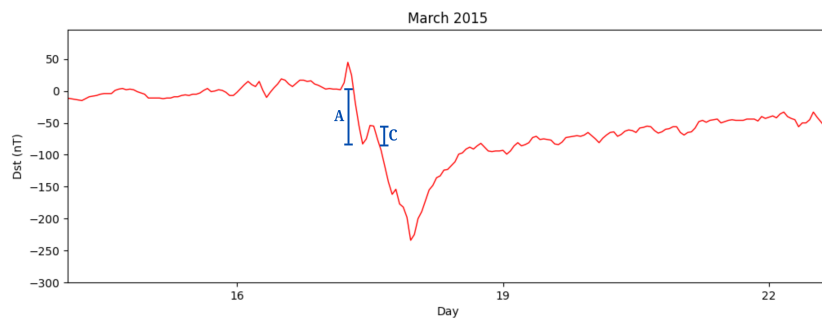


Figure 3.1: The Dst of the development of the solar storm with the double structure in the main phase.

The main phase of the storm initiates around 6.0 UT and lasts up to 23.0 UT when the recovery phase starts -with the decay of the ring current- and reaches an end on approximately the 22nd of March.

3.1.1 The Double Structure of the Storm Main Phase

An interesting feature in this storm is the double structure in the main phase (the non-smooth second Dst decay from around 12.0 UT). About 67% of intense geomagnetic storms exhibit this two-step decrease in the Dst index (i.e. two-step increase in the westward ring current) (Kamide et al., 1998). As described in (Kamide et al., 1998), the C/A factor

¹However, it will be clear in the records of the H-component of the geomagnetic stations discussed later

(see Figure 3.1) is 0.414 suggesting that this structure cannot be attributed to substorms effects on the Dst records, but it is an actual rise in the storm time ring current. One of the suggested hypotheses to explain this feature is that some of the intense solar storms are the result of the superposition of two subsequent geomagnetic storms. This hypothesis is supported by the IMF B_z data that shows a double reversal of the Northward IMF B_z into a Southward IMF B_z at 6.1 UT and 11.8 UT respectively.

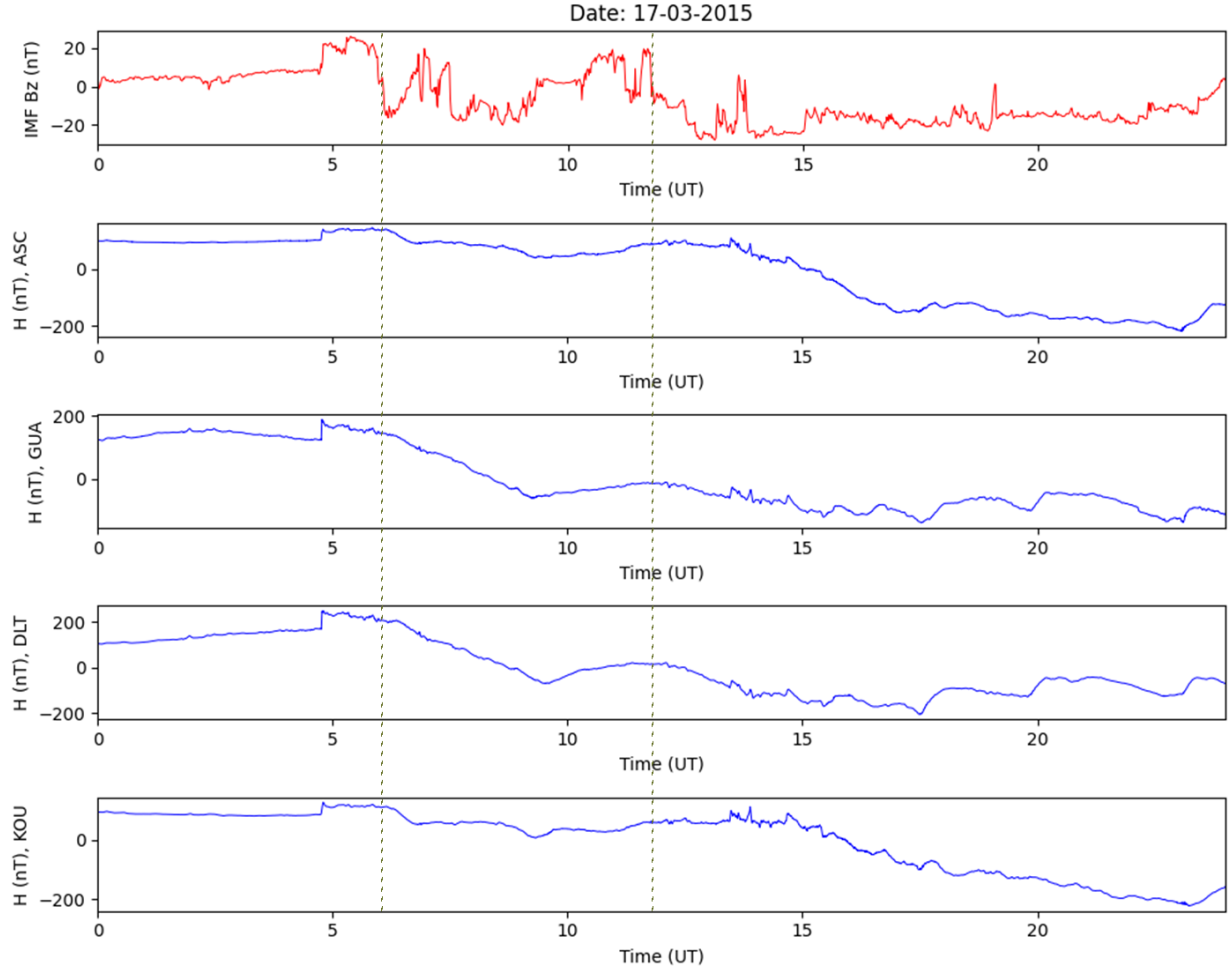


Figure 3.2: The variations of the North-South component of the interplanetary magnetic field compared to the station's H-component data. The dashed lines mark the reversal of the IMF B_z direction.

Again, the small deviations of the features occurrence in the Dst index data compared to those in the IMF data are due to the limited resolution of the Dst compared to the 1-minute data resolution of the IMF. A better comparison of the solar wind parameters with the storm phases can be done using the H-component data of the geomagnetic stations as in Figure 3.2. It is worth noting that the SSC also matches the arrival of higher amplitude IMF at around 4.8 UT.

3.1.2 The SSC and the Upstream Solar Wind Speed

The increase in the solar wind speed upstream of the bow shock (i.e. the increase in the geomagnetic field compression in the dayside) also is in sync with the enhancement of the H-component recorded by the geomagnetic stations as seen in Figure 3.3 .

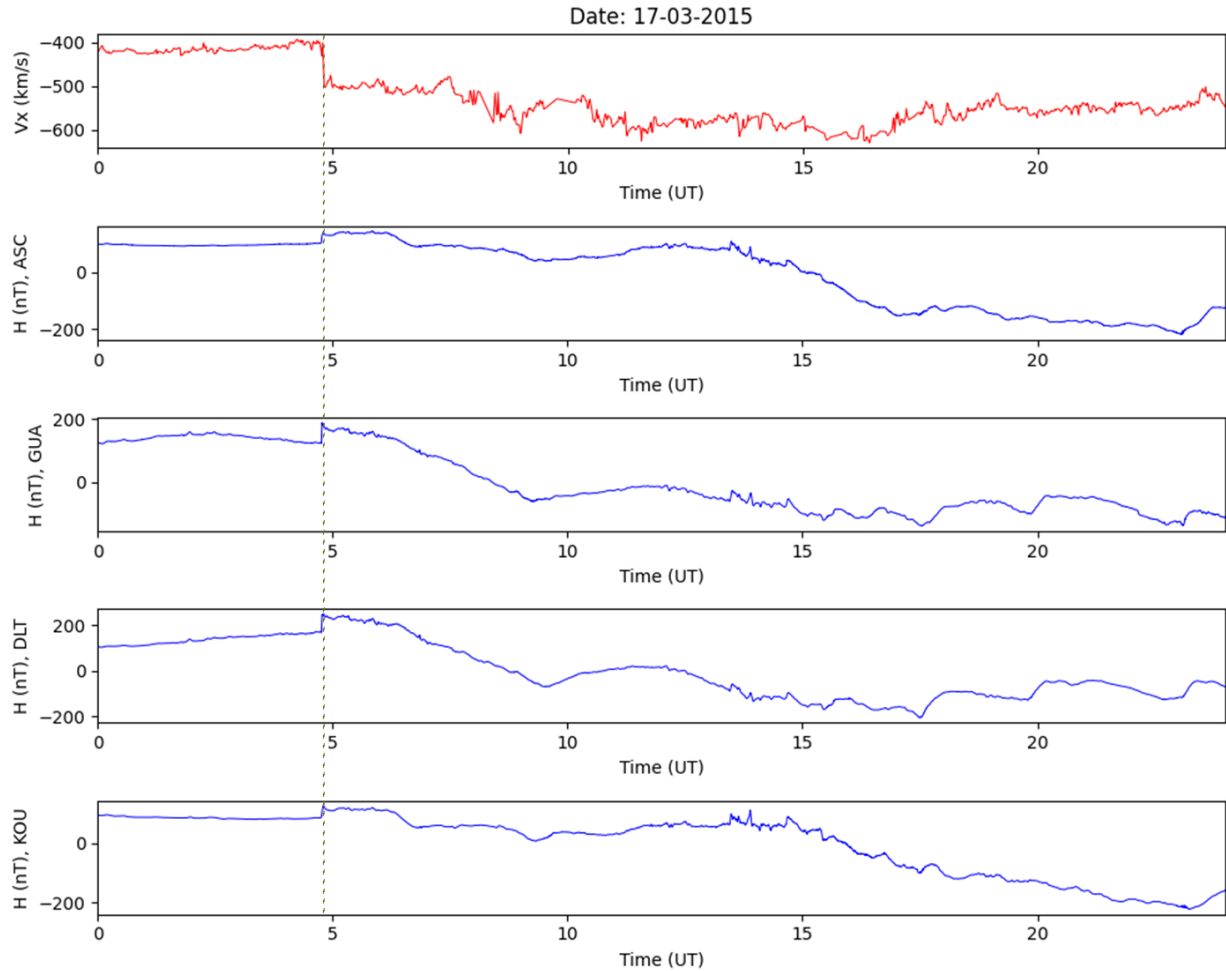


Figure 3.3: The geomagnetic observatories records of the SSC occurrence with the sudden increase in the Earthward solar wind speed.

3.1.3 Pi2s Associated with SSC

In the SSC of geomagnetic storms irregular Pi2 pulsations can be seen to overlap with a Pc4 pulsation (see Figure 3.4) as Pi2s are usually activated by impulsive sources² (Simha C et al., 2023). Another thing to notice is the variation of the SSC Pi2 peak-to-peak amplitude with the MLT (see Figure 3.5) of each of the corresponding stations (18 nT for ASC, 52.0 nT for GUA, 59.5 nT for DLT, and 18.8 nT for KOU). This suggests that the pressure exerted by the solar wind in the bow shock region enhances the subsolar currents, inducing a larger magnetic field proportional to the

²Hence, Pis usually appear as sudden bursts in the dynamic spectrum.

exerted pressure.

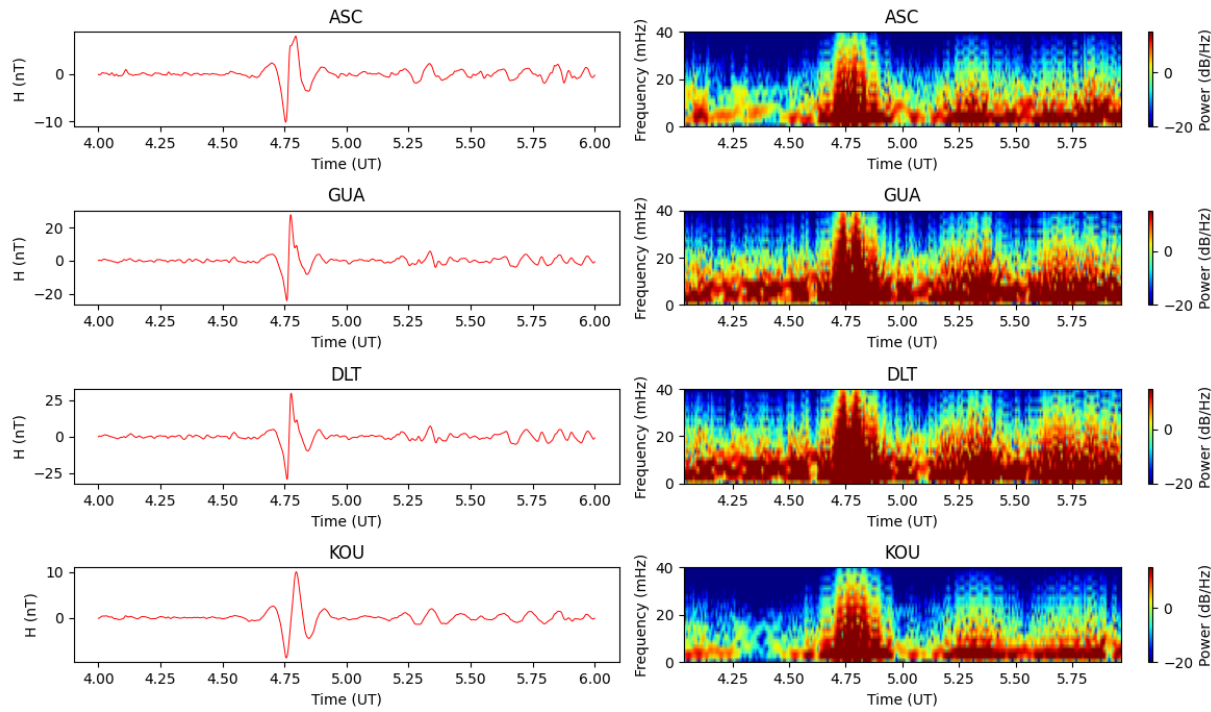


Figure 3.4: The Pi2 overlapping a Pc4 pulsation during the SSC.

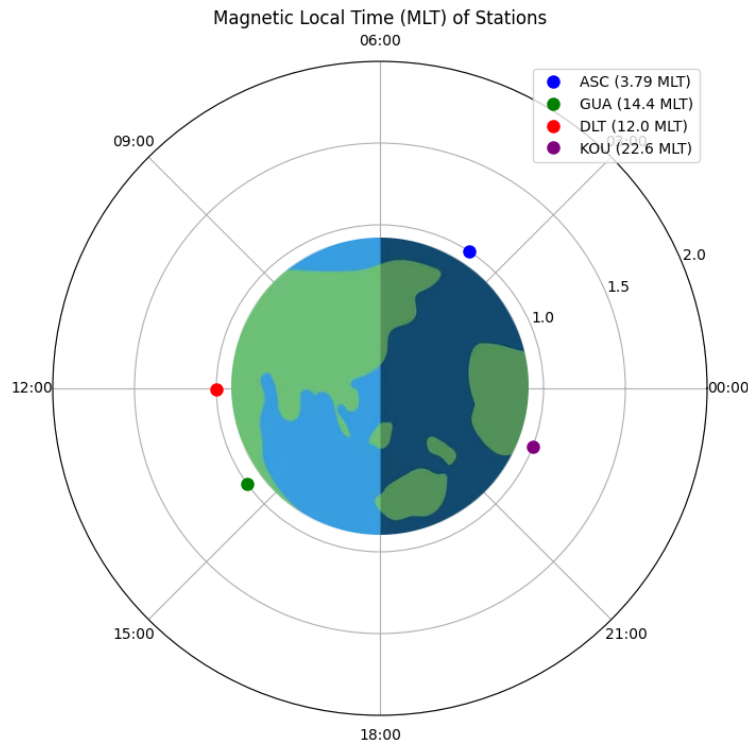


Figure 3.5: The MLT of the geomagnetic stations at 4.8 UT during the SSC.

3.1.4 Pi2s as Substorms Precursor

Pi2 events are also known to be precursors of geomagnetic substorms as they mark the onset of the expansion phase of the substorm³. In the pre-storm days, for instance, the Pi2 signal observed on the 16th of March at 3.6 UT exhibits a good concordance with the AL index⁴ seen in Figure 3.6. However, the decrease of the AL index appears slightly at a later time as the auroral currents take some time to develop and induce a magnetic field in the auroral region.

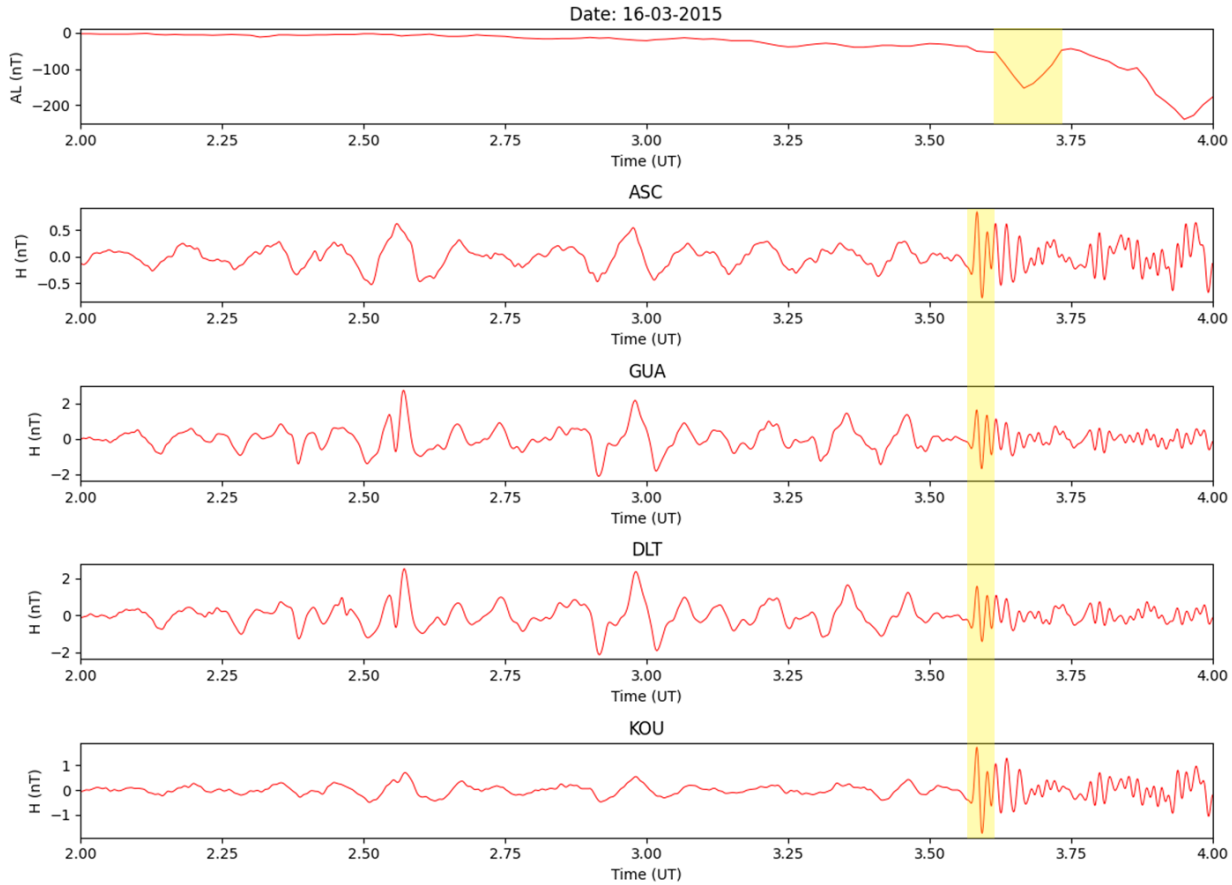


Figure 3.6: The MLT of the geomagnetic stations at 4.8 UT during the SSC.

3.2 Field Line Resonance Signature

The generated spectrogram in 3.7 of the smoothed pc3 pulsations⁵ at the ASC station on the 16th April shows a clear field-line resonance feature excited by a broadband impulsive source. The dynamic spectrum in Figure 3.7 nicely show the evenly spaced frequencies corresponding to the harmonics of field line resonance modes. The amplitude of the pulsations at each of the resonance frequencies decreases for higher harmonics as expected; as exciting higher-order modes require higher energy sources. This is essential in identifying the density of the plasma at the location of the

³When the Earth's magnetic field changes its shape into a more dipolar form (Thomas et al., 2019).

⁴Which provides a measure of the substorm activity.

⁵Using Savitzky-Golay filter of third order polynomial, 51 data point window, and multiplied by the amplitude optimization factor.

field-line⁶ (i.e. at the L-value of the field-line) simply by using Equation (1.19).

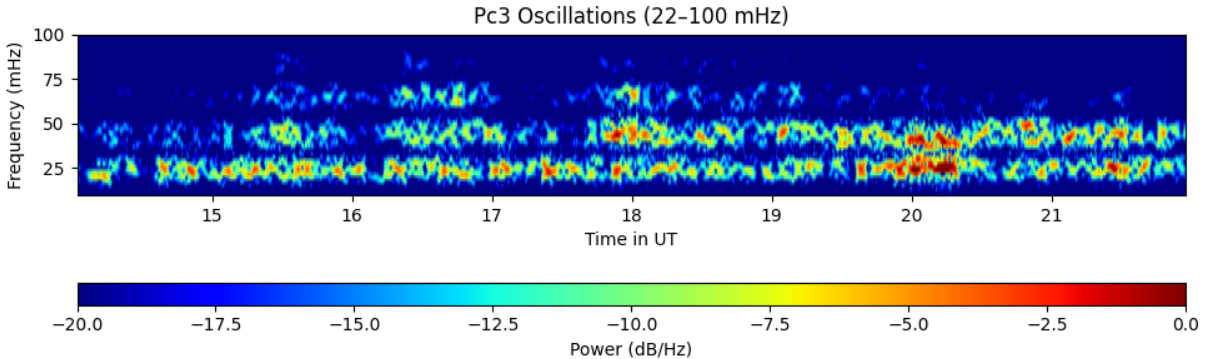


Figure 3.7: The dynamic spectrum of ASC station on the 16th of March 2015 showing the resonant eigenfrequencies due to an impulsive source.

3.3 Statistical Analysis of Continuous Pulsations

A total number of 358 continuous geomagnetic pulsations pc3-pc5 was recorded from the four different stations: ASC, DLT, GUA, and KOU. The continuous pulsations during active times ($K_p \geq 4$) were excluded in this part of the analysis as it is quite challenging to accurately define the pulsations during geomagnetically disturbed times (see Figure 3.8 and Figure 3.9 of Pc3 for comparison).

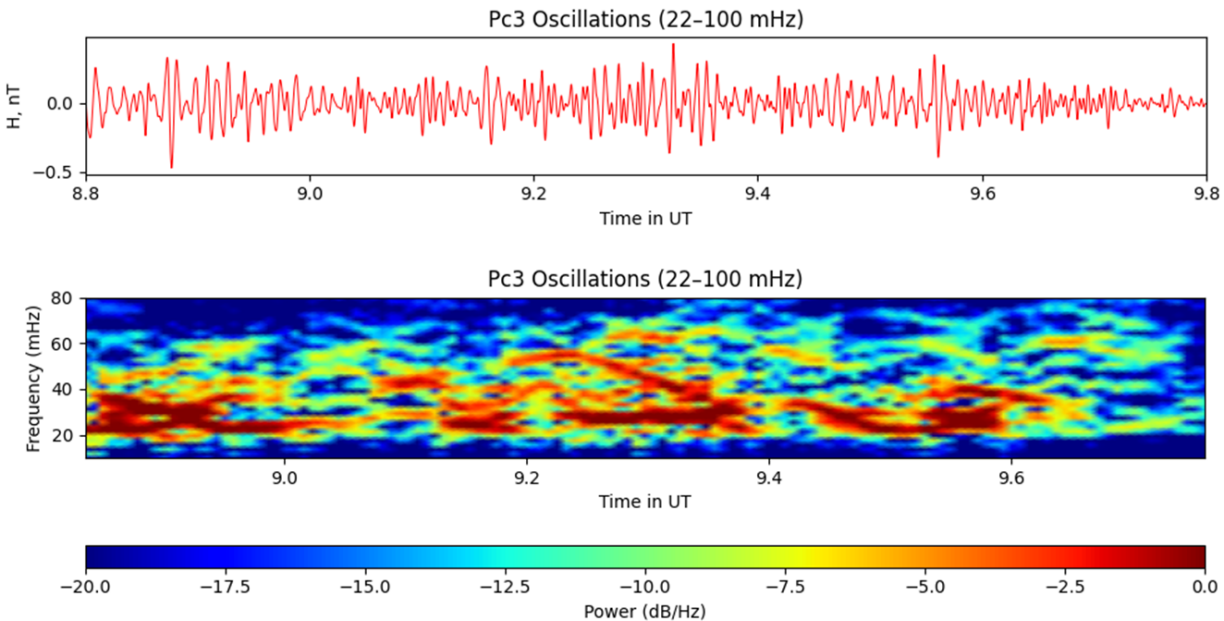


Figure 3.8: A sample of the disturbed time Pc3 on the 17th of March in DLT record.

⁶See the discussion in B.1.

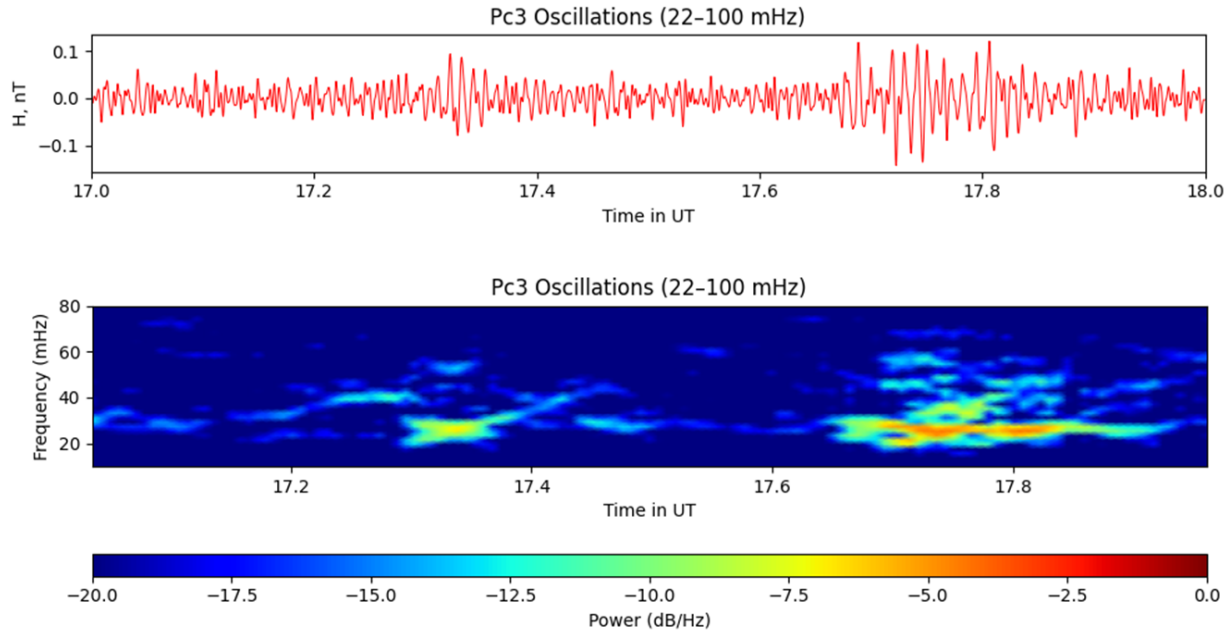


Figure 3.9: A sample of the quiet time Pc3 on the 15th of March in DLT record.

3.3.1 MLT Distribution of Pulsations

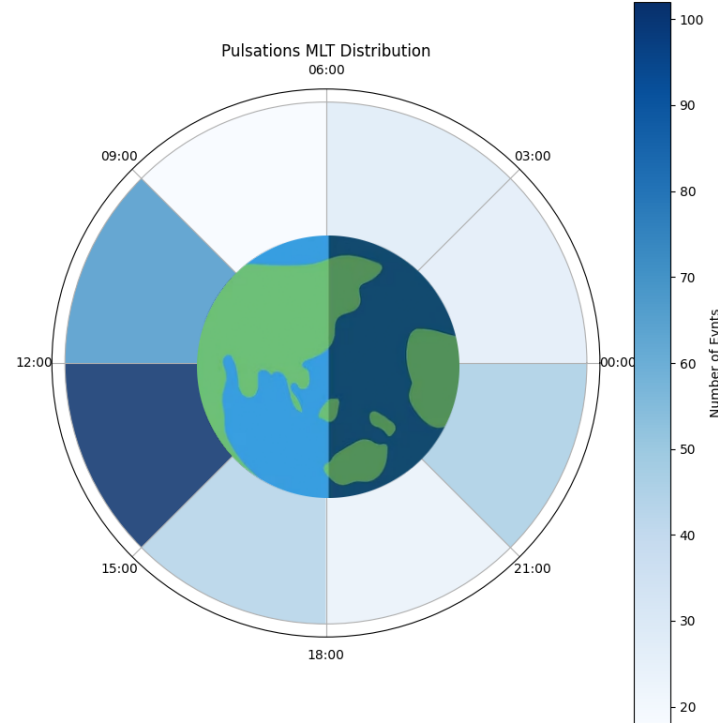


Figure 3.10: The geomagnetic pulsations distribution in MLT.

According to (Kivelson & Zu-Yin, 1984), (Anderson, 1990), (Regi, 2016), (Heyns et al., 2020), (Moura et al., 2023), and many other research papers, the ULF geomagnetic pulsations generated by the Kelvin-Helmholtz instability⁷ are dominant in the dawn-dusk flanks regions. However, as seen in Figure 3.10, the recorded pulsations seem to have dayside bow-shock preference. This suggests that the ULF pulsations in this analysis are directly generated from the solar wind time-varying compressions in the subsolar region of the magnetosphere (Borovsky & Valdavia, 2018). An additional notable aspect of the distribution in Figure 3.10 is its strong agreement with the expected arrival of the solar wind from the dusk side, propagating through the dayside, and continuing toward the dawn side as shown in Figure 3.11.

On the other hand, it should be emphasized that the method employed in the events selection is highly affected by human error as it primarily depends on the visual inspection of pulsations. Other techniques using machine learning algorithms can provide automated events selection with the minimal involvement of the researcher in the extraction procedure as in (Zanandrea et al., 2000), (Rabie et al., 2020), and in (Kim et al., 2013) and (Guo et al., 2021) implemented in whistler mode chorus waves distribution study. Additionally, further investigations should consider different models described in (Laundal & Richmond, 2016) of computing the MLT of pulsations to confirm the findings of Figure 3.10.

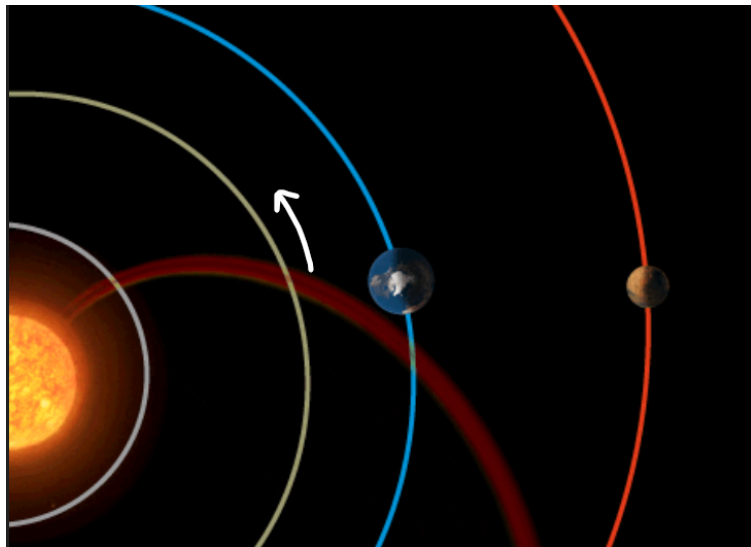


Figure 3.11: Solar wind propagation path in the subsolar region.

3.3.2 Parameters Analysis

For the different types of waves Pc3-Pc5 (see the Figures 3.12-3.14), the linear regression shows a clear correspondence (with p-value < 0.001) between the waves amplitudes and the solar wind speed, IMF B magnitude, and solar wind dynamic pressure with an average R^2 values of 0.2099, 0.4491, 0.4318 respectively. These results agree well with (Liu

⁷See Section 1.5.

et al., 2009) and (Bulusu et al., 2020). The solar wind temperature on the other hand exhibited a minimal association with $R^2 = 0.0743$ for Pc3, $R^2 = 0.0814$ for Pc4, and $R^2 = 0.1218$ for Pc5. The strong relationship between the waves amplitude and the solar wind dynamic pressure supports the results of Figure 3.10 and the suggestion that the pulsations are excited by direct pressure variations. An intriguing observation is that for all three types of Pcs, not many Pcs exist in the range of 400-500 km/s solar wind speed. It is important to also recognize that the relative amplitudes of Pcs increase from Pc3 to Pc5 as expected. This validates the pre-determined thresholds of the manual records of pulsations described earlier. Nevertheless, the overall features do not show significant distinction between the different types of pulsations.

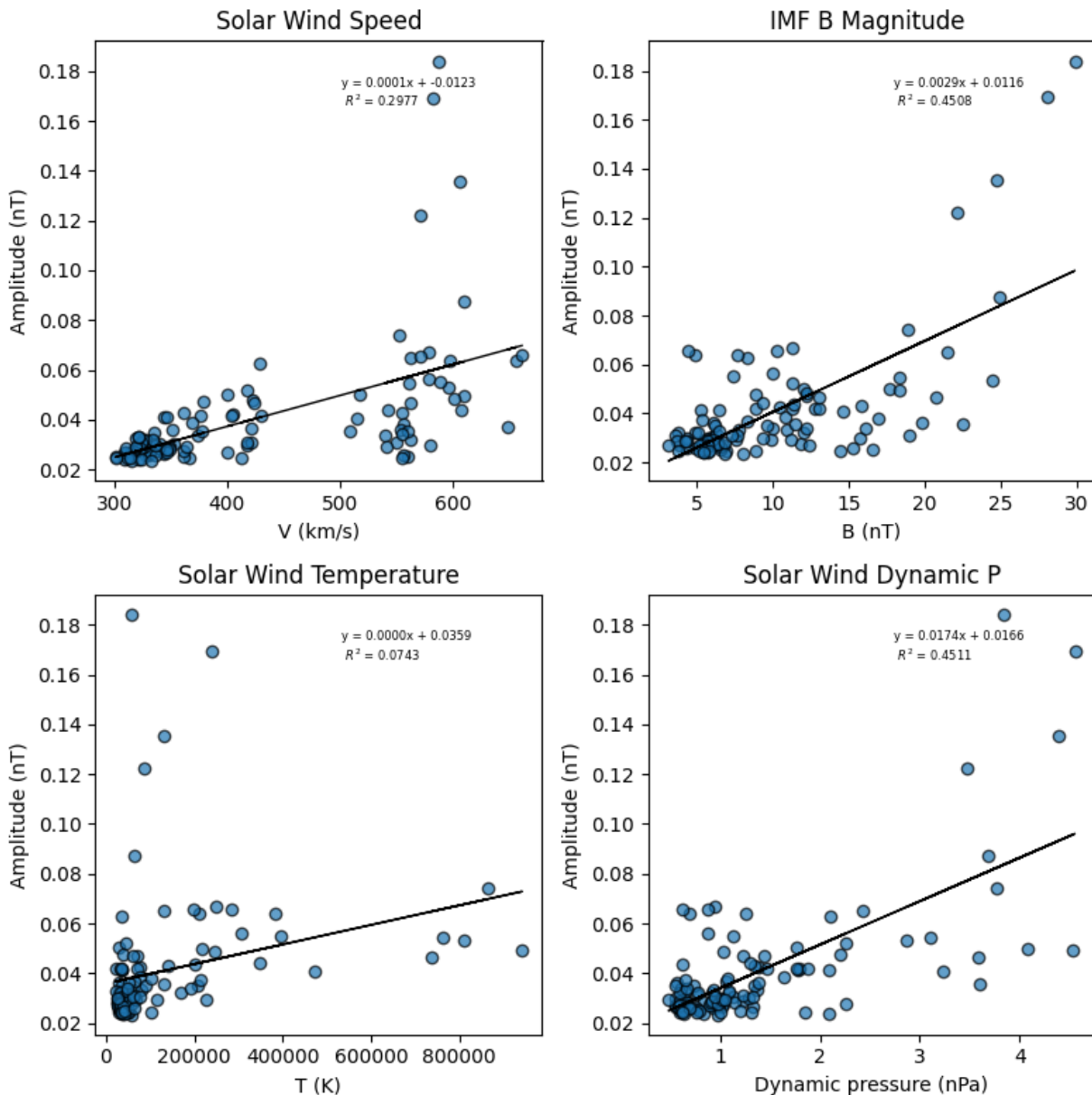


Figure 3.12: The amplitudes of Pc3 waves in ASC station data fitted with the solar wind parameters.

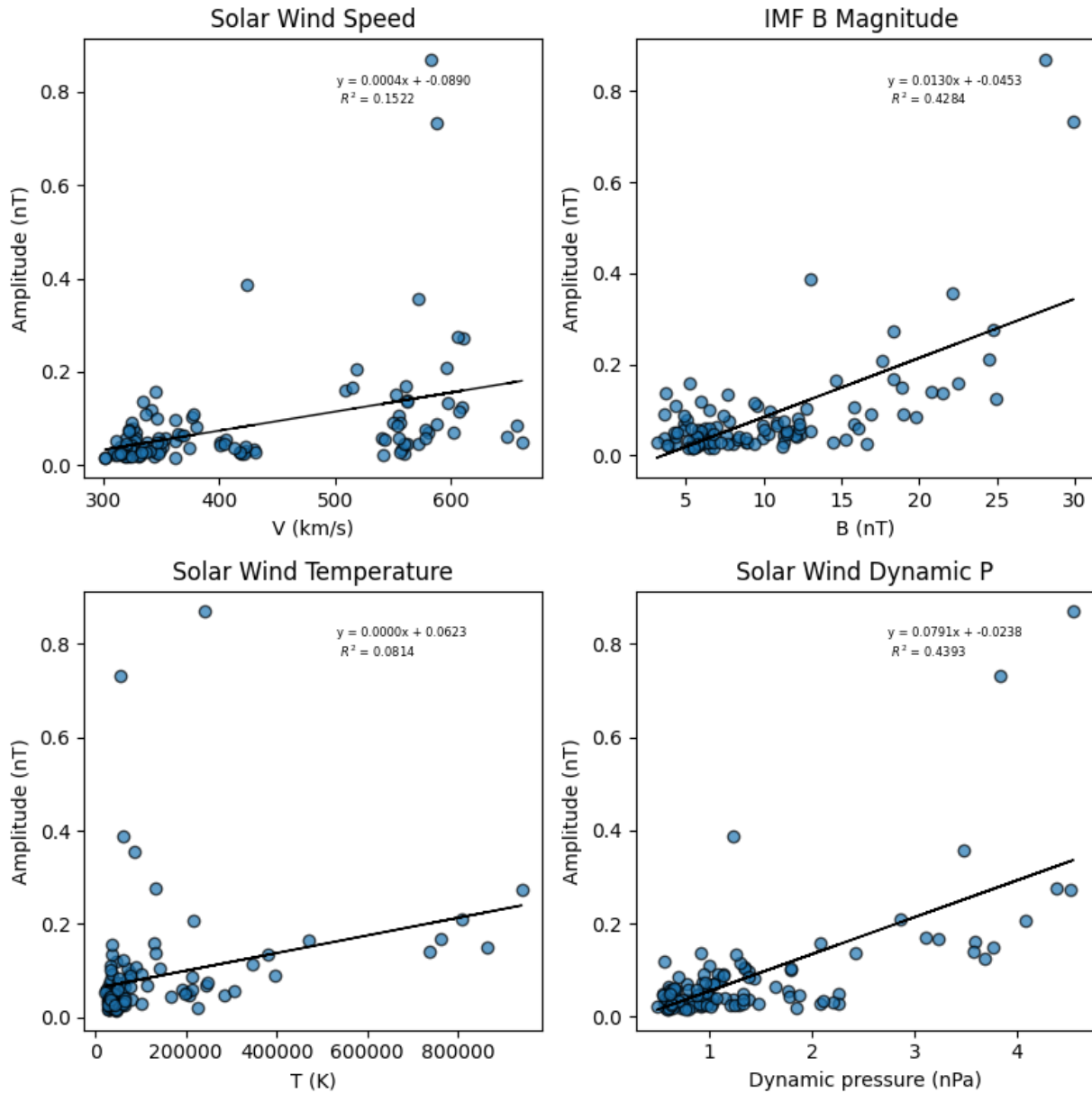


Figure 3.13: The amplitudes of Pc4 waves in ASC station data fitted with the solar wind parameters.

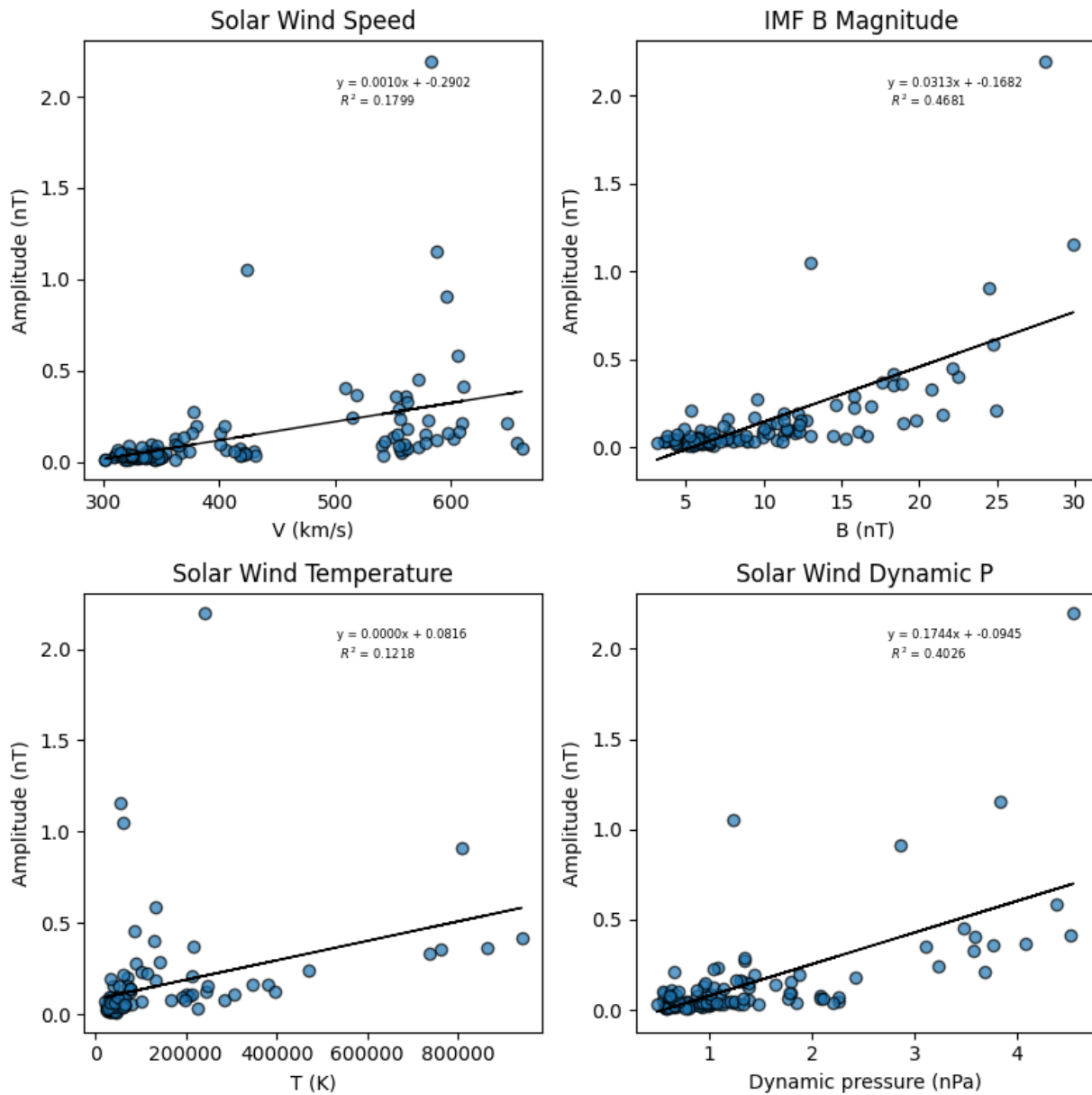


Figure 3.14: The amplitudes of $Pc5$ waves in ASC station data fitted with the solar wind parameters.

However, further investigations involving the cone angle ($\theta = \cos^{-1} \frac{B_x}{B}$) of the IMF are required to confirm that the upstream compressional waves are indeed the primary sources of the studied geomagnetic pulsations as it is well established that the upstream waves can generate Pc4 and Pc5 waves if the IMF has a low cone angle (i.e. $\theta < 45^\circ$) (Bulusu et al., 2020). Future investigations should be made to examine the solar cycle dependence of the distribution of pulsations in MLT and if the generation of Pc3-Pc5 waves can change in accordance with the sun's activity. On the other hand, a better analysis could be achieved using satellite in-situ data, because the amplitudes of the geomagnetic pulsations significantly reduce as they reach the ground stations (Gough & Orr, 1984) which can potentially affect the accuracy of the obtained results. Incorporating latitudinally distributed stations data can also narrow down the driving mechanisms of Pcs. This would help pinpoint the driving sources of each type based on the latitudinal variation of pulsations amplitude.

Chapter 4

Conclusion

In this study, the observational aspects of the solar wind-Earth coupling were investigated for the intense geomagnetic storm of March 2015. The field line resonance signature was also detected. The MLT distribution of Pcs and their correlations with the solar wind parameters were examined.

The overall features of the March 2015 double storm exhibited a strong correlation with the IMF B and V_x variations. The change in the direction of the IMF B from northward to southward was identified as the benchmark for the solar storm's onset. SSC-associated Pi2 pulsation overlapping a Pc4 signal was observed . The association of Pi2 signals with solar substorms initiation was confirmed by the subsequent decrement in the AL index making them stand as substorms precursors. On the 16th of April ASC data, a field line resonance feature was detected with the expected fall of power as the eigenfrequency increased. The investigation of the continuous pulsations distribution in MLT exhibited their dominance in the subsolar region. This suggests that these pulsations are driven by upstream solar wind compressional variations. This was supported by the strong correlation of the solar wind dynamical pressure with Pc3-Pc5. However, further conclusions about specific mechanisms differentiating each type of pulsations should be a task of future studies.

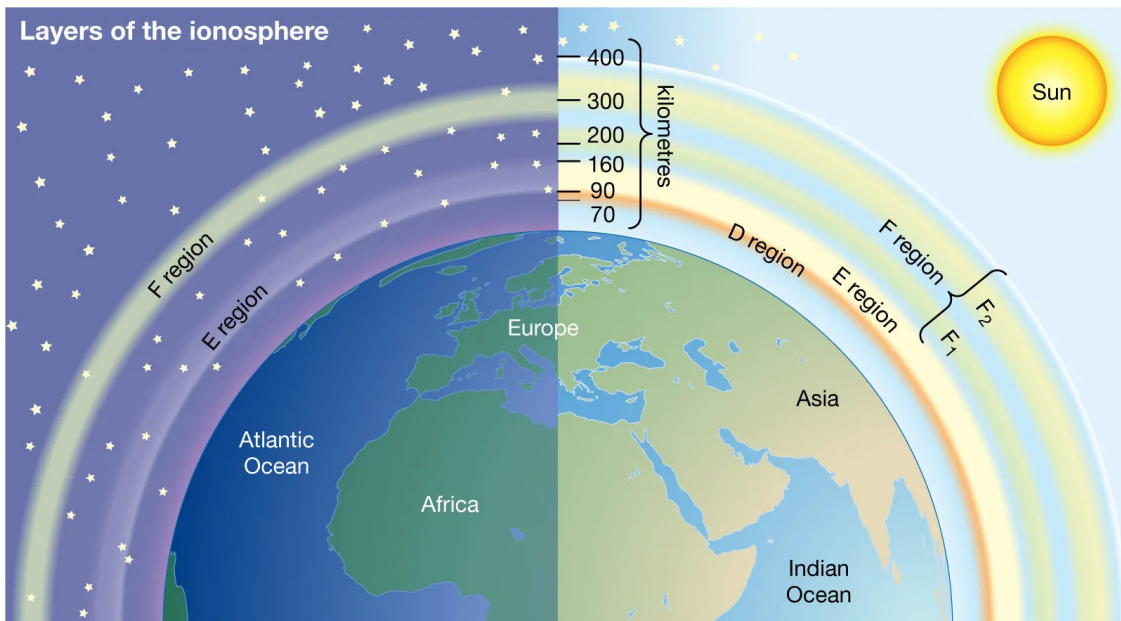
Incorporating the cone angle of the IMF, examining the solar cycle dependence of Pcs distribution, using satellite magnetic data, and investigating the longitudinally distributed stations data can significantly improve the results of future analysis and help in drawing better conclusions on the generating mechanisms of ULF geomagnetic pulsations. To avoid human error in pulsations global distribution, machine learning algorithms can be used to automate the pulsations selection process.

The findings of this project illuminate the necessity of interdisciplinary methods for unravelling the complexity of the Sun-Earth interactions and the determination of the origin of continuous geomagnetic pulsations.

Appendices

The Ionosphere

The ionosphere¹ is defined as the region within the Thermosphere that extends from around 50 km to 200-600 km above the Earth's surface. This appendix draws heavily from (Haq Wani et al., 2021) and (Haralambous & Papadopoulos, 2009).



© 2012 Encyclopædia Britannica, Inc.

Figure A.1: The ionospheric layers during day and night time. Source: britannica.com

¹Fun story: when the ionosphere was first discovered by Oliver Heaviside in 1902 he gave this layer his name "Heaviside Layer". Today, we call this particular layer of the ionosphere the E-Layer, where E is taken from the 'E' in -Electrical layer- and for his hard luck not many people know its original name.

A.1 Ionospheric Layers

Based on the level of ionization², the ionosphere is divided into three main regions: D-Layer, E-Layer, and F-Layer. The thickness of all three layers increases during the day and decreases during the night time. However, it is worth noting that during the daytime the F-Layer can be subdivided into F₁-Layer and F₂-Layer while D-Layer almost disappears at night (see Figure A.1).

- **D-Layer:**

This layer extends from 48-90 km from sea level. The ionization of NO molecules is governed by the Hydrogen's Lyman- α radiation, while N₂ and O₂ ionization is caused by high-energy X-rays of solar radiation. Also, for low altitudes of the D-layer, the dominant ionization source is due to the cosmic rays. However, in this layer, the recombination rate of ions is high in a way that it vanishes during the night-time. This layer also applies some constraints on HF radio wave propagation. Medium and low-frequency HF radio waves are absorbed in this region due to the dragged free electrons collisions with neutral molecules.

- **E-Layer:**

The E-layer is the middle layer of the ionosphere where the sources of O₂ and NO ionization are mainly the soft X-rays and UV-rays from the sun. Because solar radiation is the main source of ionization of this layer, it significantly decreases in thickness during the night time. Also, it is worth mentioning that the HF radio waves can be reflected in this layer with a small fraction being absorbed.

- **F-Layer:**

It is the upper-most layer where maximum ionization takes place. Ionization here is dominated by extreme UV-rays and X-rays from solar radiation. Due to its high electron density and good reflection ability, it plays a major role in HF radio wave reflection.

²The atom is said to be ionized when sufficient energy is given to the outer-shell electron knocking it out of the atom and leaving it with a positive charge.

Appendix **B**

Other Coordinate Systems

This Appendix is primarily informed by (Campbell & Banerjee, 1998) and (Koskinen & Kilpua, 2021), with the figures adapted from (Campbell & Banerjee, 1998).

B.1 The Dipole Coordinate System (r, θ, ϕ)

To relate different points on Earth on a large scale, a dipole approximation can be applied. However, this can only be a valid approximation for the low-latitude inner magnetospheric regions.

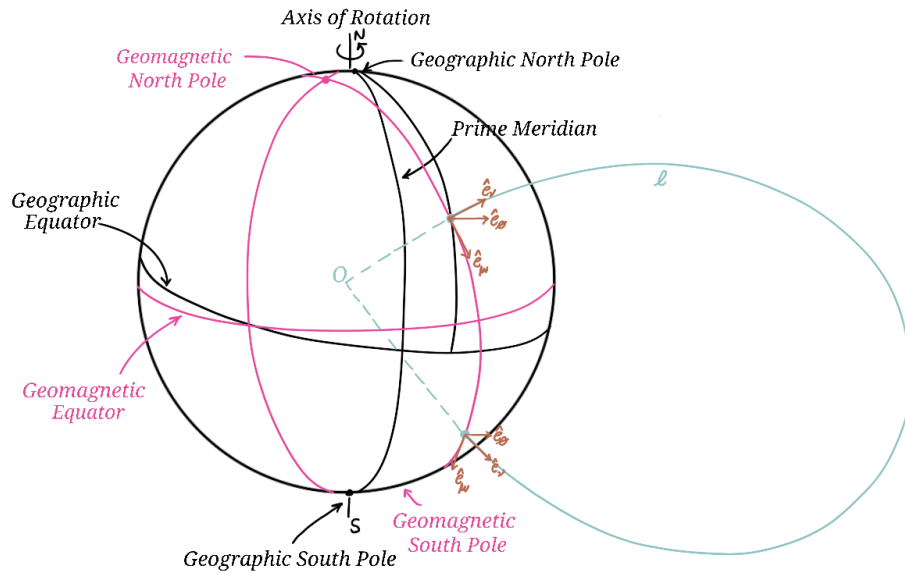


Figure B.1: The projection of the geomagnetic coordinate system on the geographic coordinate system.

Using the dipole coordinate system (r, θ, ϕ) the same way as the geographic coordinate system (GCS), r represents the radial distance in the direction of the field line from the centre of the Earth, θ is the polar angle in degrees

measured from the geomagnetic North pole (it is the geomagnetic colatitude¹) along a longitudinal field line, and ϕ is the azimuthal angle in degrees (it is the geomagnetic longitude) along the same latitudinal line. This is illustrated in Figure B.1. It is worth noting that many more complex and numerical models exist to find more accurate and representative geomagnetic coordinates (you may want to see (Laundal & Richmond, 2016)). A useful parameter to define in this discussion is called the *L-value* (or L-shell or sometimes the McIlwain parameter). Different L-values define different regions in the centered dipole approximation. It can be found as:

$$L = \frac{r}{\cos^2(\lambda)}, \quad (\text{B.1})$$

where r is the distance from the Earth's center in Earth radii unit (R_e) and λ is the geomagnetic latitude.

For the near-Earth region, the L-value can be approximated to be the distance in R_e to the field-line (i.e. an L-value = 1 is at the surface of the Earth).

B.2 Local Magnetic Field-aligned Coordinates (v, μ, ϕ)

Figure B.1 also shows the unit vectors assigned to the points along a certain magnetic field line in what is commonly called the *field-aligned coordinates*. The positive v direction is radially anti-Earthward, μ is along the magnetic field direction, and ϕ is the azimuthal angle Eastward.

¹To find the latitude, latitude = $90^\circ - \text{colatitude}$.

Brief Introduction to Plasma Physics

Hannes Alfvén got his Nobel prize in 1970 due to his discovery of the Alfvén waves *in less than a half-page paper* published in 1942! (Alfvén, 1942)¹ To appreciate this discovery and explore its' great implications, one has to go through the brief story of plasma physics and the MHD model.

This Appendix is written based on: (Anderson, 1990), (Chen, 1984), and (Koskinen & Kilpua, 2021).

C.0.1 What is a Plasma?

In introductory classes to the states of matter, plasma is usually introduced as the matter consisting of an ionized gas. However, not all ionized gasses are plasma. The more accurate definition of plasma is *a quasi-neutral gas exhibiting collective behaviour*. Quasi-neutrality refers to the fact that the charge density of the overall ions and electrons in a plasma at equilibrium cancels each other to produce a semi-neutral matter. On the other hand, collective behaviour refers to the property of the plasma at equilibrium to influence a distant plasma regions once locally disturbed. The plasma consists of charged particles influenced by applied electric and magnetic fields and induces electric and magnetic fields in return. This makes describing the behavior of a plasma quite complex and models such as the magnetohydrodynamic model in 1.8 are applied to simplify the problem.

C.0.2 Plasma Motion

The ions and electrons in the plasma can undergo gyration (or cyclotron motion), drift motion, and a bounce motion (or mirror motion) as illustrated in Figure C.1 re-drawn from (Koskinen & Kilpua, 2021).

¹Although his 50's notation was quite ugly, it was one of the revolutionary papers in the world of physics!

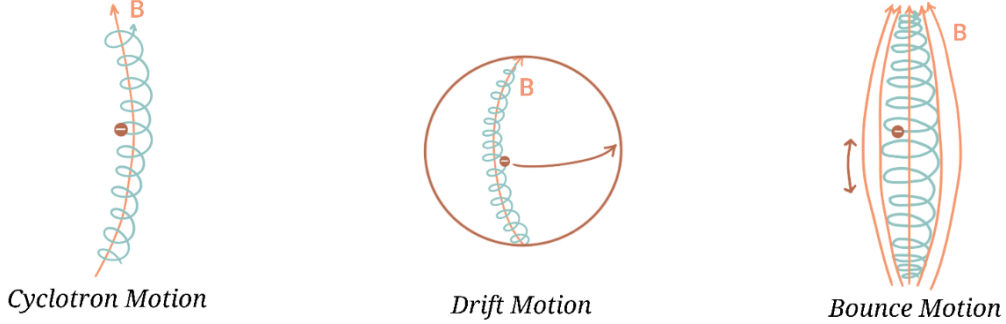


Figure C.1: Motion of an electron in the magnetic field.

- **Cyclotron Motion:** As a result of the Lorentz force,

$$\vec{F} = q\vec{E} + q\vec{v} \times \vec{B}, \quad (\text{C.1})$$

a moving charged particle gyrates around a field line with radius called the *Larmor radius* where \vec{E} is the electric field, q is the charge of the particle, \vec{v} is the velocity of the particle, and \vec{B} is the magnetic field. The Larmor radius is given as:

$$r_L = \frac{mv_\perp}{|q|\vec{B}}, \quad (\text{C.2})$$

where m is the mass of the particle, and v_\perp is the velocity component perpendicular to the magnetic field.

The frequency of the gyration motion is given by:

$$\omega = \frac{|q|\vec{B}}{m}. \quad (\text{C.3})$$

- **Drift Motion:** Any force acting perpendicular to the magnetic field can cause the particle to drift (e.g. the gradient of the magnetic field, the curvature of the field line, gravity, etc.) with a velocity:

$$\vec{v}_D = \frac{\vec{F} \times \vec{B}}{qB^2}, \quad (\text{C.4})$$

where \vec{F} is the general force.

A special force that causes electrons and ions to drift in the same direction is the electric force $\vec{F} = q\vec{E}$ (as the charge will cancel). This force will not generate an electric current upon the drift motion, since ions and electrons will move together.

- **Bounce Motion:** This is the motion when charged particles bounce along the magnetic field line as in Figure C.1. This is the result of the invariant quantity μ called the *magnetic moment* and is given by:

$$\mu = \frac{mv_{\perp}^2}{2B}. \quad (\text{C.5})$$

When the particle moves from a region with weak magnetic field to a region with strong one, its total energy must be conserved:

$$E = \frac{1}{2}mv_{\parallel}^2 + \frac{1}{2}mv_{\perp}^2. \quad (\text{C.6})$$

For μ to be invariant, v_{\perp} must increase when the magnitude of \vec{B} increases. Consequently, v_{\parallel} must decrease for the energy to be constant. Which makes the particle bounce back².

²This is the basic principle for what is called *plasma confinement*.

Appendix **D**

The MHD Wave Equation

Under the assumptions of the MHD model, The MHD wave equation can be obtained using the following *magnetohydrodynamic* equations:

The Continuity Equation:

$$\frac{\partial \rho_m}{\partial t} + \vec{\nabla} \cdot (\rho_m \vec{V}) = 0, \quad (\text{D.1})$$

The Equation of State:

$$\frac{d}{dt} \left(\frac{\vec{P}}{\rho_m^\gamma} \right) = 0 \rightarrow \vec{P} = C \rho_m^\gamma, \quad (\text{D.2})$$

The Equation of Motion¹:

$$\rho_m \left(\frac{\partial \vec{V}}{\partial t} + (\vec{V} \cdot \vec{\nabla}) \vec{V} \right) = \vec{J} \times \vec{B} - \vec{\nabla} \vec{P}, \quad (\text{D.3})$$

Ampere's Law:

$$\vec{\nabla} \times \vec{B} = \mu_0 \vec{J}, \quad (\text{D.4})$$

Faraday's Law:

$$\vec{\nabla} \times \vec{E} = - \frac{\partial \vec{B}}{\partial t}, \quad (\text{D.5})$$

¹Or, The Momentum Equation. It is also worth mentioning that the second and fourth terms here should be neglected under the assumption of cold and incompressible plasma. However, they will be kept in this discussion to get the most general solution and will be discarded later.

Ohm's Law:

$$\vec{E} + \vec{V} \times \vec{B} = \eta \vec{J}, \quad (\text{D.6})$$

where ρ_m is the mass density, \vec{V} is the centre of mass velocity, \vec{P} is the pressure, γ is the ratio of the specific heat under constant pressure to the specific heat under constant volume (C_p/C_v), \vec{J} is the current density, \vec{B} is the magnetic field, \vec{E} is the electric field, η is the resistivity, and μ_0 is the permeability of free space.

It is worth noting that we can obtain the induction equation in Equation (1.1) by using Ohm's law, Ampere's law, and Faraday's law:

$$\vec{\nabla} \times \vec{E} + \vec{\nabla} \times \vec{V} \times \vec{B} = \eta(\vec{\nabla} \times \vec{J}) \rightarrow \frac{\partial \vec{B}}{\partial t} = \eta \nabla^2 \vec{B} + \vec{\nabla} \times (\vec{V} \times \vec{B}).$$

Under the infinite conductivity condition ($\eta \rightarrow 0$):

$$\frac{\partial \vec{B}}{\partial t} = \vec{\nabla} \times \vec{V} \times \vec{B}.$$

Following the assumption of an adiabatic process and taking the gradient of the equation of state,

$$\vec{\nabla} \vec{P} = C \vec{\nabla} \rho_m^\gamma = C \gamma \rho_m^{\gamma-1} \vec{\nabla} \rho_m = \frac{\gamma(C \rho_m^\gamma)}{\rho_m} \vec{\nabla} \rho_m.$$

Using Equation (D.2),

$$\vec{\nabla} \vec{P} = \frac{\gamma \vec{P}}{\rho_m} \vec{\nabla} \rho_m \rightarrow \vec{\nabla} \vec{P} = v_s^2 \vec{\nabla} \rho_m, \quad (\text{D.7})$$

where $v_s = \sqrt{(\gamma \vec{P}/\rho_m)}$ is the speed of sound.

Now, the goal is to replace \vec{J} and \vec{E} by using the Equations (D.7) and (D.4) and substituting them into the equation of motion in Equation (D.3):

$$\rho_m \left(\frac{\partial \vec{V}}{\partial t} + (\vec{V} \cdot \vec{\nabla}) \vec{V} \right) = \frac{(\vec{\nabla} \times \vec{B})}{\mu_0} \times \vec{B} - v_s^2 \vec{\nabla} \rho_m.$$

Hence the equations now become:

$$\frac{\partial \rho_m}{\partial t} + \vec{\nabla} \cdot (\rho_m \vec{V}) = 0, \quad (\text{D.8})$$

$$\rho_m \left(\frac{\partial \vec{V}}{\partial t} + (\vec{V} \cdot \vec{\nabla}) \vec{V} \right) = \frac{(\vec{\nabla} \times \vec{B})}{\mu_0} \times \vec{B} - v_s^2 \vec{\nabla} \rho_m, \quad (\text{D.9})$$

$$\vec{\nabla} \times \vec{V} \times \vec{B} = \frac{\partial \vec{B}}{\partial t}. \quad (\text{D.10})$$

When a small transverse disturbance is applied to the plasma, the linearized first-order perturbations of the variables become:

$$\vec{B}(\vec{r}, t) = B_0 + \delta \vec{b}(\vec{r}, t),$$

$$\rho_m(\vec{r}, t) = \rho_0 + \tilde{\rho}_m(\vec{r}, t),$$

$$\vec{V}(\vec{r}, t) = \vec{v}(\vec{r}, t),$$

where B_0 , ρ_0 , δb , $\tilde{\rho}_m$ and \vec{v} are the unperturbed ambient magnetic field, the equilibrium density, the perturbation of the magnetic field, the perturbation in plasma density, and the velocity of the plasma perpendicular to the magnetic field respectively.

Substituting each of the variables into Equation (D.8) and Equation (D.10):

$$\begin{aligned} \frac{\partial \tilde{\rho}_m}{\partial t} + \rho_0 \vec{\nabla} \cdot \vec{v} + \vec{\nabla} \cdot (\tilde{\rho}_m \vec{v}) &= 0, \\ \frac{\partial \tilde{\rho}_m}{\partial t} + \rho_0 \vec{\nabla} \cdot \vec{v} &= 0, \end{aligned} \quad (\text{D.11})$$

while the cancelled term has a negligible effect (i.e. it is a second-order perturbation).

Doing the same thing for Equation (D.9) and removing all the non-linear perturbation terms:

$$(\tilde{\rho}_m + \rho_0) \left(\frac{\partial \vec{v}}{\partial t} + \vec{v} \cdot \vec{\nabla} \vec{v} \right) = \tilde{\rho}_m \cancel{\frac{\partial \vec{v}}{\partial t}} + \rho_0 \frac{\partial \vec{v}}{\partial t} = \frac{1}{\mu_0} \vec{\nabla} \times (\vec{B}_0 + \delta \vec{b}) \times (\vec{B}_0 + \delta \vec{b}) - v_s^2 \vec{\nabla} \tilde{\rho}_m.$$

Expanding the right-hand side of the equation,

$$\rho_0 \frac{\partial \vec{v}}{\partial t} = \frac{1}{\mu_0} \left[\underbrace{\vec{\nabla} \times \vec{B}_0 \times \vec{B}_0}_{\text{Term 1}} + \underbrace{\vec{\nabla} \times \delta \vec{b} \times \vec{B}_0}_{\text{Term 2}} + \underbrace{\vec{\nabla} \times \vec{B}_0 \times \delta \vec{b}}_{\text{Term 3}} + \underbrace{\vec{\nabla} \times \delta \vec{b} \times \delta \vec{b}}_{\text{Term 4}} \right] - v_s^2 \vec{\nabla} \tilde{\rho}_m.$$

It is clear why the first and the fourth terms get cancelled. However, the third term gets cancelled because $\vec{\nabla} \times \vec{B}_0 = 0$. Therefore,

$$\begin{aligned}\rho_0 \frac{\partial \vec{v}}{\partial t} &= \frac{1}{\mu_0} \vec{\nabla} \times \vec{\delta b} \times \vec{B}_0 - v_s^2 \vec{\nabla} \tilde{\rho}_m \\ \rho_0 \frac{\partial \vec{v}}{\partial t} + v_s^2 \vec{\nabla} \tilde{\rho}_m + \vec{B}_0 \times \frac{(\vec{\nabla} \times \vec{\delta b})}{\mu_0} &= 0.\end{aligned}\quad (\text{D.12})$$

Now for Equation (D.10),

$$\begin{aligned}\vec{\nabla} \times \vec{v} \times (\vec{B}_0 + \vec{\delta b}) &= \vec{\nabla} \times (\vec{v} \times \vec{B}_0 + \cancel{\vec{v} \times \vec{\delta b}}) = \frac{\partial}{\partial t}(\vec{\delta b}) \\ \vec{\nabla} \times (\vec{v} \times \vec{B}_0) &= \frac{\partial}{\partial t}(\vec{\delta b}).\end{aligned}\quad (\text{D.13})$$

Taking the time derivative of both sides of Equation (D.12),

$$\rho_0 \frac{\partial^2 \vec{v}}{\partial t^2} + v_s^2 \vec{\nabla} \frac{\partial \tilde{\rho}_m}{\partial t} + \frac{\vec{B}_0}{\mu_0} \times \left(\vec{\nabla} \times \frac{\partial}{\partial t}(\vec{\delta b}) \right) = 0. \quad (\text{D.14})$$

Using Equation (D.11) and Equation (D.13) and substituting them in Equation (D.14),

$$\begin{aligned}\frac{\partial^2 \vec{v}}{\partial t^2} - v_s^2 \vec{\nabla}(\vec{\nabla} \cdot \vec{v}) + \frac{\vec{B}_0}{\sqrt{\mu_0 \rho_0}} \times \left(\vec{\nabla} \times \vec{\nabla} \times \vec{v} \times \frac{\vec{B}_0}{\sqrt{\mu_0 \rho_0}} \right) &= 0, \\ \boxed{\frac{\partial^2 \vec{v}}{\partial t^2} - v_s^2 \vec{\nabla}(\vec{\nabla} \cdot \vec{v}) + v_A \times (\vec{\nabla} \times \vec{\nabla} \times \vec{v} \times v_A)} &= 0\end{aligned}\quad (\text{D.15})$$

where $v_A = \vec{B}_0 / \sqrt{\mu_0 \rho_0}$ is the *Alfven velocity*.

Appendix **E**

EM Waves Reflection

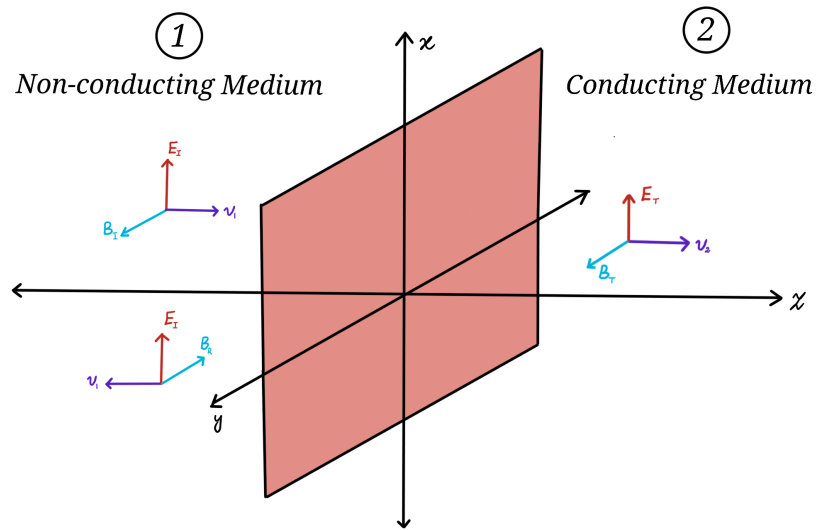


Figure E.1: The boundary layer between region 1 (vacuum in this discussion) and the conducting medium of region 2 (the ionosphere).

Following (Griffiths, 2017) to exhibit the mirror-like boundary effect, we consider the boundary conditions of an electromagnetic wave propagating at the boundary of vacuum to a conducting material (illustrated in Figure E.1):

$$(i) \epsilon_0 E_1^\perp - \epsilon_2 E_2^\perp = \sigma_f, \quad (ii) B_1^\perp - B_2^\perp = 0, \quad (iii) \epsilon_0 E_1^{\parallel} - \epsilon_2 E_2^{\parallel} = 0, \quad (iv) \frac{1}{\mu_0} B_1^{\parallel} - \frac{1}{\mu_2} B_2^{\parallel} = K \times \hat{n},$$

where ϵ_0 and ϵ_2 are the permittivities of the first¹ and second medium, μ_0 and μ_2 are the permeability of the first and second medium, σ_f and K are the free surface charge and surface current, and \perp and \parallel signs denote the perpendicular

¹Which is the vacuum in this scenario.

and parallel components relative to the boundary layer.

From the illustration in Figure E.1 (which considers normal incidence), the reflected, incident, and transmitted electric and magnetic fields are²:

Incident fields:

$$E_I(z, t) = E_{0I} e^{i(k_1 z - \omega t)} \hat{e}_x \quad B_I(z, t) = \frac{1}{v_1} E_{0I} e^{i(k_1 z - \omega t)} \hat{e}_y, \quad (\text{E.1})$$

Reflected fields:

$$E_R(z, t) = E_{0R} e^{i(-k_1 z - \omega t)} \hat{e}_x \quad B_R(z, t) = -\frac{1}{v_1} E_{0R} e^{i(k_1 z - \omega t)} \hat{e}_y, \quad (\text{E.2})$$

Transmitted fields:

$$E_T(z, t) = E_{0T} e^{i(k_2 z - \omega t)} \hat{e}_x \quad B_T(z, t) = \frac{1}{v_2} E_{0T} e^{i(k_2 z - \omega t)} \hat{e}_y. \quad (\text{E.3})$$

Be noted that all the components of the electric and magnetic fields above are complex.

Since $E_1^\perp = E_2^\perp = B_1^{\parallel\parallel} = B_2^{\parallel\parallel} = 0$, σ_f becomes 0 according to condition (i), and condition (ii) is directly becomes satisfied. Now, at $z = 0$, condition (iii) implies that:

$$E_{0I} + E_{0R} = E_{0T}. \quad (\text{E.4})$$

Assuming that $K = 0$, condition (iv) becomes:

$$\frac{1}{\mu_0} \left(\frac{E_{0I}}{v_1} - \frac{E_{0R}}{v_1} \right) = \frac{1}{\mu_2} \left(\frac{E_{0T}}{v_2} \right),$$

$$E_{0I} - E_{0R} = \frac{\mu_0 v_1}{\mu_2 v_2} E_{0T}.$$

By defining $\zeta \equiv \frac{\mu_0 v_1}{\mu_2 v_2}$ and establishing the relationship between the reflected wave and the incident wave, and the transmitted wave and the incident wave using Equation (E.4):

$$E_{0T} = \left(\frac{2}{1 + \zeta} \right) E_{0I} \quad E_{0R} = \left(\frac{1 - \zeta}{1 + \zeta} \right) E_{0I}. \quad (\text{E.5})$$

²Notice that $\vec{B} = \frac{1}{v} \vec{k} \times \vec{E}$ for an electromagnetic wave.

For a perfect conductor, the conductivity is assumed to be infinite. Hence, $k_2 \rightarrow \infty$ and $v_2 \rightarrow 0$ and by applying L'Hôpital's rule, Equation (E.5) becomes:

$$E_{0T} = 0 \quad E_{0R} = -E_{0I}. \quad (\text{E.6})$$

Likewise,

$$B_{0T} = 0 \quad B_{0R} = -B_{0I}. \quad (\text{E.7})$$

Appendix F

Digital Signal Processing (DSP)

Digital Signal Processing (DSP) is a multi-stage process for which an analog signal can be digitized and modified by applying some mathematical operations and certain algorithms to extract informative data. Some stages in DSP are performed using hardware (e.g. transducer¹ and Analog to Digital Converter (ADC)), while other stages can be done using software (e.g. some algorithms and filters). DSP has many applications in electronics, communications, tomography, cartography, speech recognition, seismology, geomagnetism, and more (Thankachan, 2019).

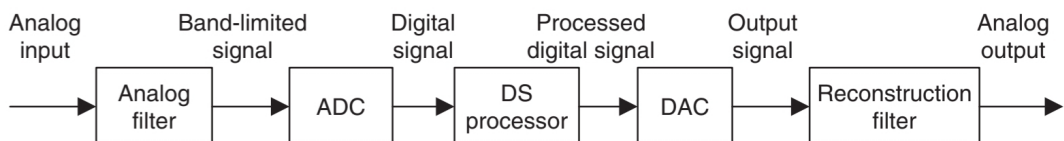


Figure F.1: An illustration for the process of DSP.

The main stages of the DSP involve: filtering an analog signal, digitizing it, performing few DSP operations, converting the digital signal back to analog signal, and smoothing and preparing the signal. These stages are illustrated in the diagram shown in Figure F.1.

In this chapter some overall important topics in DSP are discussed on the basis of (Tan & Jiang, 2013) and (Lu et al., 2020).

¹The sensor that converts a non-electrical analog signal into electrical one like sound.

F.1 Digitizing the Analog Signal

A continuous analog signal can be recorded via an analog to digital converter (ADC) at even intervals called the "sampling rate" (or sampling frequency). The sampling rate can be thought of as the rate in which someone is taking snapshots of a wave. The more snapshots he or she takes, the more resolvable is the collected signal. In geomagnetic data, the sampling frequency can range from 1 second to a month("IAGA 2002 Data Exchange Format", 2024). However, the sampling frequency imposes some limitations for the information that could be extracted from the signal. This is known as the "Nyquist Criteria".

F.1.1 Nyquist Sampling Theorem

The Nyquist sampling criteria implies that for a sampling rate f_s , the sampling rate has to be greater than or equal to $2f_{\max}$, where f_{\max} is the highest frequency of interest in the signal. In other words:

$$f_s \geq 2f_{\max} \text{ (or) } f_{\text{Nyquist}} \geq f_{\max}, \quad (\text{F.1})$$

where the Nyquist frequency $f_{\text{Nyquist}} = f_s/2$.

However, if someone were to use a sampling rate that is *less* than twice the highest frequency contained in the signal, then the shape and frequency of the waveform will be diminished in what is called "aliasing".

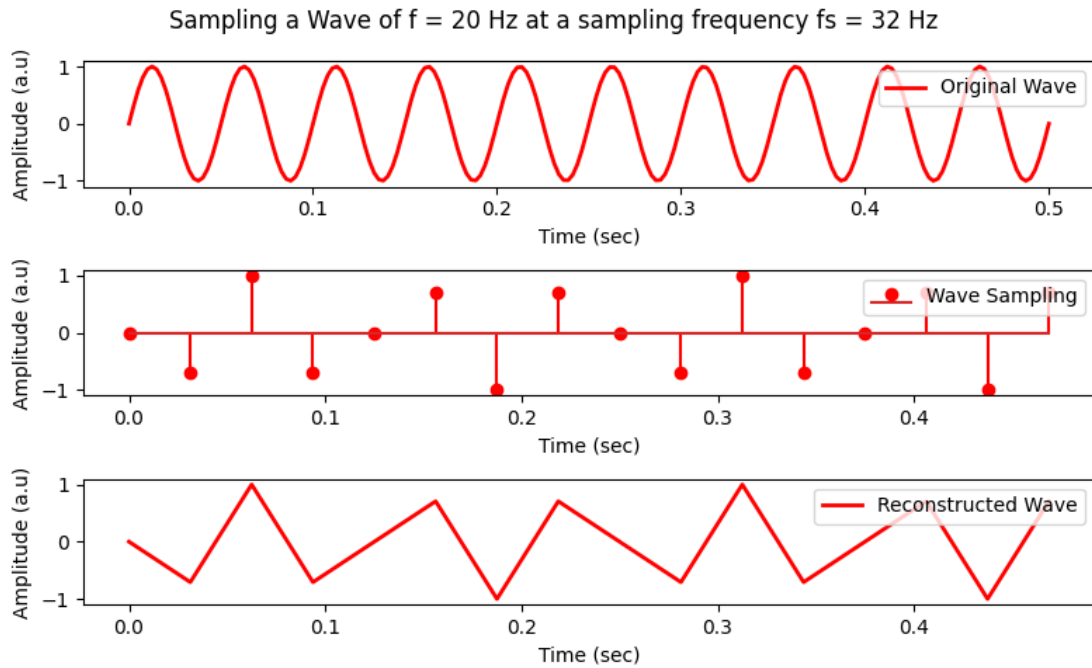


Figure F.2: When the Nyquist criteria is not satisfied, the reconstructed wave cannot be used to give information about the original wave.

In Figure F.2, the frequency of a sinusoidal wave is 20 Hz, while the sampling frequency of this continuous wave is 32 Hz (less than $2f_{\max}$, which is 40 Hz in this case). The reconstructed wave in Figure F.2 clearly shows that the information of the original signal is lost.

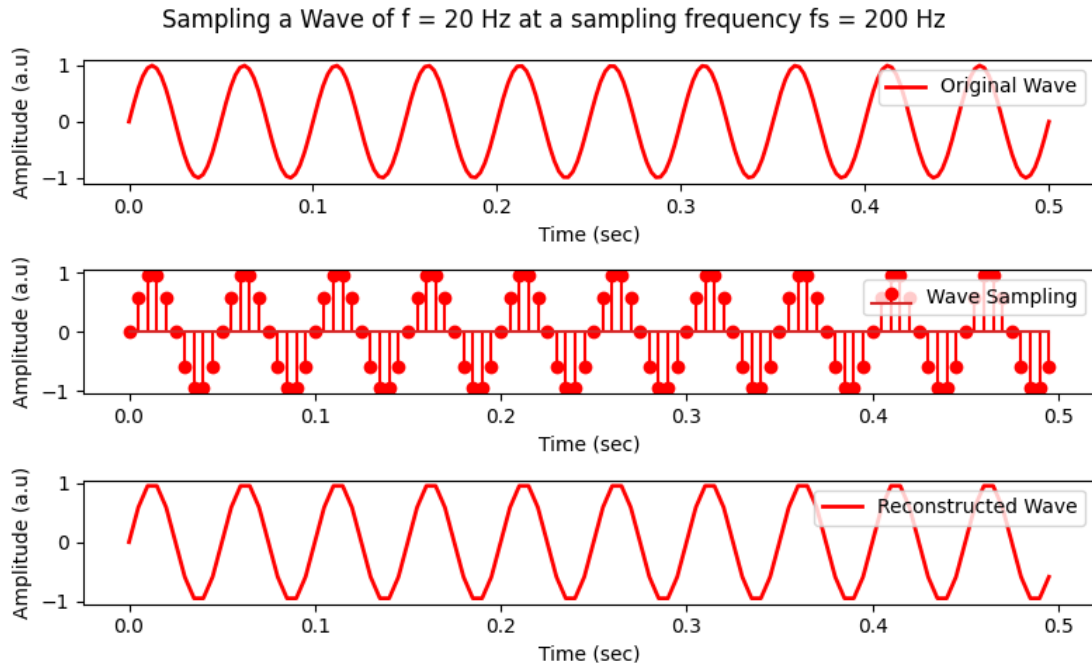


Figure F.3: When the Nyquist criteria is satisfied, the reconstructed wave can be used to give some information about the original wave.

On the other hand, Figure F.3 shows the case where the Nyquist criteria is satisfied. The reconstructed wave is very close to the original wave, and the higher is the sampling frequency the closer the reconstructed wave gets to the original one.

To avoid aliasing, usually an analog filter called *anti-aliasing filter* is used to eliminate the frequencies higher than twice the maximum frequency of interest².

It is worth noting that the digitizing process involve sampling and quantization together. This can be seen clearly if the first two blocks in Figure F.1 is further divided as in Figure F.4. The sampling is the process discussed above, while quantization is the process where the amplitude of the analog signal is being digitized as fixed multi-levels of amplitude as seen in Figure F.5. In this process, the amplitude of the signal is being approximated to the nearest level.

²Although this is not perfect as will be discussed in the next chapter. Some percentage of aliasing will always be there

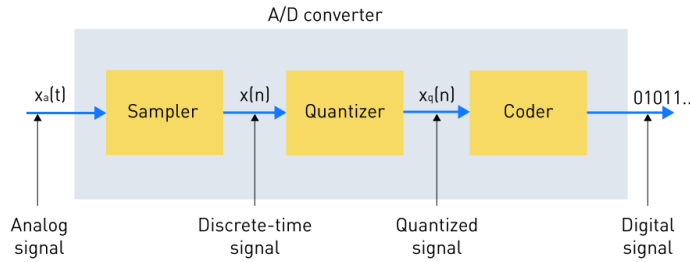


Figure F.4: Further dividing the Analog to Digital Converter (ADC) block. Source: monolithicpower.com

This approximation step loses some information of the amplitude³. Although the amplitude and the time are quantized at this stage, the signal cannot be called *digitized*, unless each level is given a certain number of bits.

In general:

$$\text{Number of levels} = 2^n, \quad (\text{F.2})$$

where n is the number of bits.

The signal to quantization noise ratio is defined as:

$$\left(\frac{S}{N}\right)_{dB} = 6.02n + 1.8 + 10\log\left(\frac{f_s}{2}\right) \quad (\text{F.3})$$

Which tells that the accuracy of the quantization step can be enhanced by increasing the number of levels and the sampling frequency.

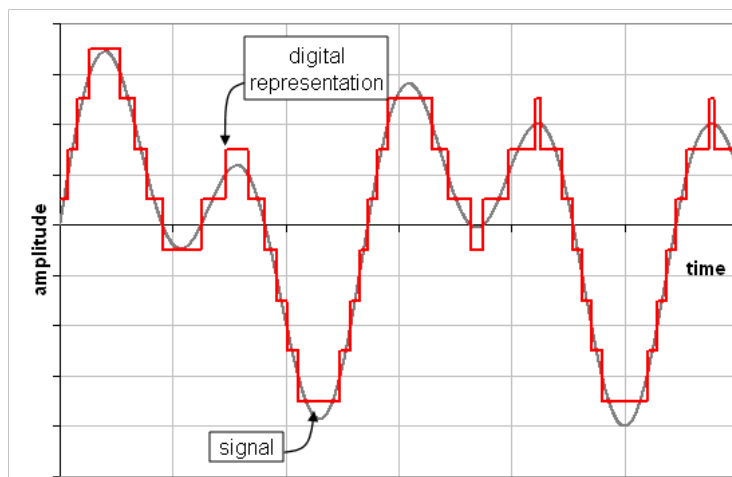


Figure F.5: The quantization of an analog signal. Source: trentsclassassignment.weebly.com

³Even though it can be negligible in some cases, one should be aware that this is still a loose process.

F.2 Signal Filtering

Filtering the sampled data is a very important step in the process of DSP. The two main classes of filters are the analog filters and digital filters. While analog filters represent the hardware circuits that operate upon an input continuous signal; digital filters are mathematical operations that act on the discrete sampled data of the continuous signal to suppress some frequencies or perform certain phase changes. Basic digital filters types include: high-pass filters, low-pass filters, band-pass filters, and band-stop⁴ filters (see Figure F.6).

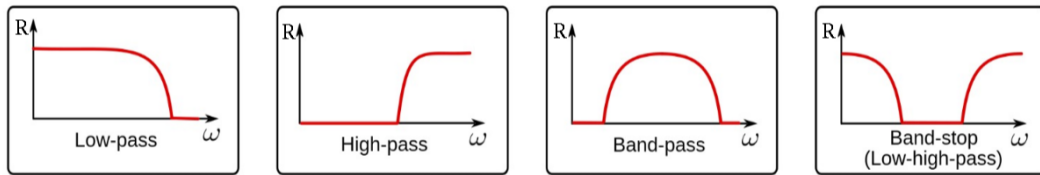


Figure F.6: The different types of filters used in digital signal processing analysis. Source: norwegiancreations.com

F.2.1 Low-pass Filter

When a discrete signal is processed via a low-pass filter, the frequencies higher than a determined frequency called the cutoff-frequency f_c will be attenuated and the output signal will consist of those frequencies that are lower than the cutoff-frequency⁵. This can be useful when a study of a certain signal takes the low frequency signals to be of main interest and discard high-frequency data from the signal (i.e. reduce the high frequency noise). Another application of these filters involves avoiding aliasing by removing the frequencies that do not satisfy the Nyquist criteria as described in F.1.1.

F.2.2 High-pass Filter

In some applications, high frequency phenomena in a signal can be of main interest. In this case, a high-pass filter is applied for the sampled data to extract the data of frequencies higher than the cutoff-frequency and discard those that are lower.

F.2.3 Band-pass Filter

In geomagnetic studies, seismology, audio engineering, and other applications that involve filtering a data that fall in a determined frequency band, the best choice of filter is the band-pass filter. This filter can be considered as a combination of low-pass filter and high-pass filter.

⁴Some times called notch filter or band-rejection filter.

⁵Although this is actually an idealized scenario.

F.2.4 Band-stop Filter

This type of filters operates opposite to the way that band-pass filters do. When a band of frequencies is taken as an input, this filter removes these frequencies from the signal returning the signal of frequencies excluding them.

F.3 Filters Characteristics

There are various designs and algorithms of filters. Commonly used filters include: Butterworth, Chebyshev, Bessel, Elliptic, etc. However, these filters share some common characteristics for their overall functionalities (see Figure F.7).

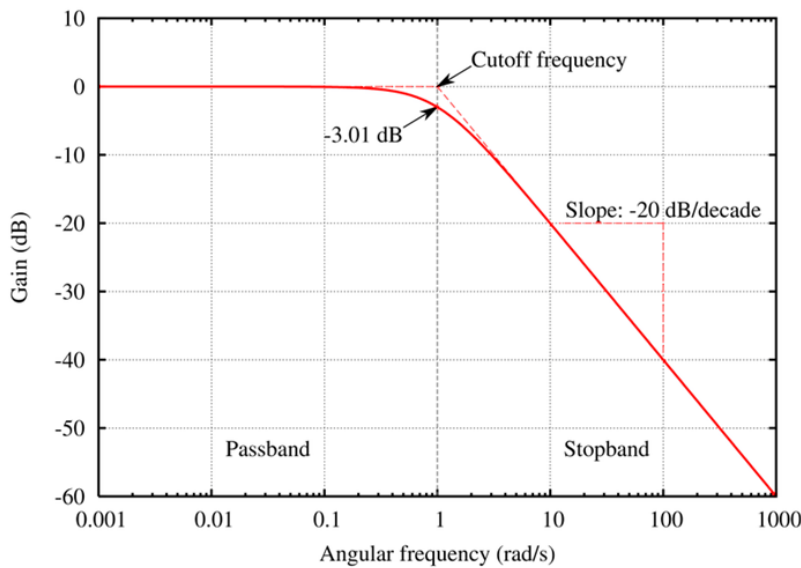


Figure F.7: Main features of the low-pass filter. Source: training.dewesoft.com

Some of these characteristics are:

- **Type:** high-pass, low-pass, band-pass, band-stop, etc.
- **Cut-off frequency:** which is defined as the frequency where the signal is -3 dB attenuated⁶. It is worth mentioning that for non-ideal filters, the cutoff frequency does not sharply cuts the unwanted frequencies. Instead, it rolls off them.
- **Order:** which determines the steepness (or slope) of the filter measured in dB/decade where the decade is defined as a factor of 10 of the frequency⁷. The order of any digital filter is defined by the slope of its roll-off region.

⁶Gain or attenuation in dB (decibels) = $20\log(A)$, where A is the attenuation ratio.

⁷For example, from 10 Hz to 100 Hz is one decade. While from 10 Hz to 1000 Hz is two decades.

- **Response:** Finite Impulse Response (FIR) or Infinite Impulse Response (IIR) filters. The differences between these types is summarized in Table F.1.

Feature	FIR Filters	IIR Filters
Stability	Stable	Can be unstable
Phase Response	Can be adapted to linear	Usually non-linear
Computational	Requires more computational power	Requires less computational power
Design Complexity	Easy to design	Complex
Applications	Phase-sensitive systems	Real-time systems

Table F.1: The difference between FIR and IIR filters.

F.4 Smoothing and Noise Reduction

Reserving some important features of a signal can sometimes require smoothing out the signal or reducing the noise involved in it. Many techniques can be performed for such problems. One can use the filtering method to exclude unwanted frequencies from the signal. On the other hand, the *Moving Average* is one of the statistical techniques used for such tasks as well. The *Simple Moving Average* takes some n odd and adjacent values of the signal and replace them with their average, and then moves to the other n values and do the same thing. There are various types of the *Moving Average* method. These types differ in their complexity and computational power needed. Interpolating or adding some additional data in-place of missing points can sometimes be considered as part of smoothing or de-noising a digital signal. linear or cubic interpolations are usually used for these purposes.

F.5 Transforming Signals

One common practice in DSP is to take the signal from a time domain, into a frequency domain. When a certain quantity varies with time, sometimes it is very difficult to get useful information from the time variation only. Hence, as seen in Figure F.8 it is useful to perform what is known as *transformations* to understand the constituent frequencies of a signal.

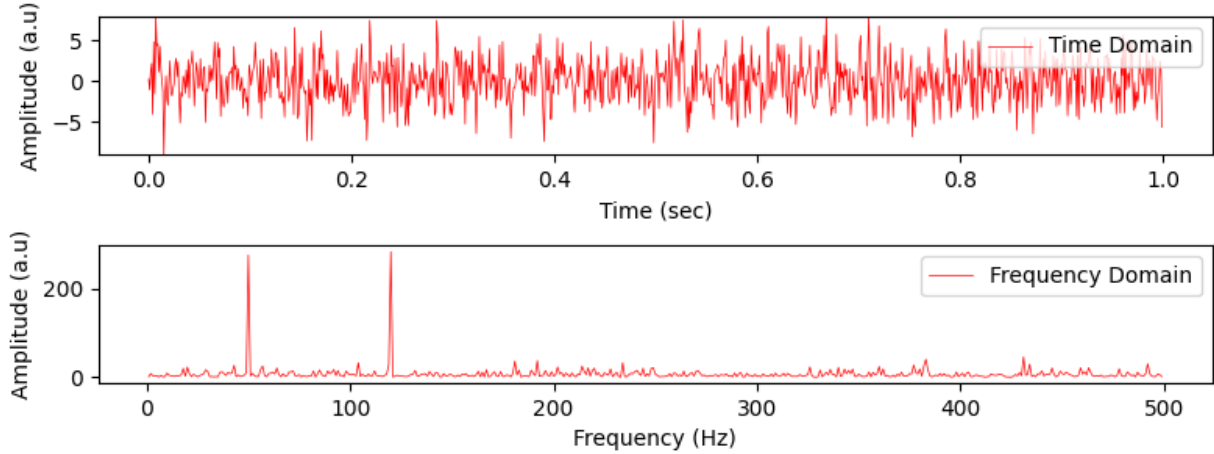


Figure F.8: Time varying signal transformed into the frequency domain. The frequency domain (upon applying the Fourier transformation) clearly shows two dominant frequencies in the signal.

The commonly used transforms include: Fourier transform (FT), discrete Fourier transform (DFT), Laplace's transform, z-transform, Hadamard transform, Walsh transform, Haar Transform, etc (Thankachan, 2019).

The Fourier transform (FT) is defined as (Islam & Islam, 2019):

$$F(\omega) = \int_{-\infty}^{\infty} f(t) e^{-i\omega t} dt, \quad (\text{F.4})$$

where $f(t)$ is the signal in the time domain and $F(\omega)$ is the signal in the frequency domain.

The Fourier transform is useful when the time domain signal is continuous. However, it is very common to encounter discrete digitized signal $x[n]$ that its frequency signal $x[k]$ spectrum is of interest. Hence, the discrete Fourier transform (DFT) for a finite signal interval is given by (Islam & Islam, 2019):

$$x[k] = \sum_{n=0}^{N-1} x[n] e^{-i \frac{2\pi}{N} n k}, \quad (\text{F.5})$$

where k is the number of cycles and N is the number of data points (and k/N is the sinusoid frequency).

F.6 FFT and STFT Algorithms

If one were to use the DFT in Equation (F.5) directly, the computational power that will be required would be very high, making it impractical. An algorithm called the *fast Fourier transform* (FFT) makes use of symmetries in the DFT to efficiently apply the DFT for the entire signal.

For non-stationary signals (i.e. when the frequency changes over time), the short-time Fourier transform (STFT) algorithm is applied for the signal. In this algorithm, the signal is divided into equal overlapping segments where the FT is applied for each segment. Each of the segments is windowed (i.e. multiplied by a window function) with a function that makes the amplitude at the edges of the segment approach zero in a smooth style. This is important to reduce the broadening of the frequency lines that is called *leakage*.

The STFT is given by (Moura et al., 2023) as:

$$F(\tau, \omega) = \int_{-\infty}^{\infty} f(t)w(t - \tau)e^{-i\omega t}dt, \quad (\text{F.6})$$

where $w(t - \tau)$ is the window function centered at time τ .

Examples of window functions are as follows: Hamming, Hann, and Blackman-Harris windows (Thankachan, 2019). Other leakage reduction methods involve increasing the number of data points or extending the observation window. This trades frequency resolution for time resolution, as longer observation windows provide better frequency precision at the expense of temporal detail.

F.7 Welch's Method

Another method that is more robust for non-stationary signals is called the *Welch's method*. It is similar to the STFT with the exception that the periodograms are now averaged⁸ (Welch, 1967), resulting in a smoother frequency spectrum compared to the FFT method. It provides a better power resolution to the disadvantage of a lower frequency resolution⁹ (Jwo et al., 2021).

⁸And with no time information as in the dynamic spectrum.

⁹As the frequency resolution degrades with decreasing number of data points.

Appendix G

Supplementary Codes

```
[1]: import pandas as pd
import numpy as np
import matplotlib.pyplot as plt
import scipy.signal as sci
import matplotlib.image as mpimg
from scipy.stats import linregress
import mplcursors
import matplotlib.cm as cm
from matplotlib.colors import Normalize
%matplotlib inline
```

Functions

```
[3]: def file_read_sw(fileName, path = ''):
    destination = path + fileName
    data = pd.read_csv(destination, sep='\s+')#delim_whitespace=True)
    data.columns = 'Year', 'DOY', 'HR', 'MN', 'Timeshift', 'Bx', 'By', 'Bz', ↴
    ↴'Vx', 'Vy', 'Vz', 'Rho', 'Temp', 'P', 'AL'
    return data

def file_read_AL(fileName, path = ''):
    destination = path + fileName
    data = pd.read_fwf(destination, sep = '\s+', header = None)
    data.columns = ['Date', 'Time', 'DOY', 'AE', 'AU', 'AL', 'AO']
    data['Hour'] = pd.to_datetime(data['Time'], format='%H:%M:%S.%f').dt.hour
    data['Min'] = pd.to_datetime(data['Time'], format='%H:%M:%S.%f').dt.minute
    data['Sec'] = pd.to_datetime(data['Time'], format='%H:%M:%S.%f').dt.second
    return data

def IAGA_file_read(fileName, path = ''):
    destination = path + fileName
    data = pd.read_fwf(destination, sep = '\t')
    data.columns = ['Date', 'Time', 'DOY', 'H', 'D', 'Z', 'F']
    data['Hour'] = pd.to_datetime(data['Time'], format='%H:%M:%S.%f').dt.hour
    data['Min'] = pd.to_datetime(data['Time'], format='%H:%M:%S.%f').dt.minute
    data['Sec'] = pd.to_datetime(data['Time'], format='%H:%M:%S.%f').dt.second
    return data

def day(df):
    return df['DOY'] - 59

def IAGA_file_read2(fileName, path = ''):
    destination = path + fileName
    data = pd.read_fwf(destination, sep = '\t')
    data.columns = ['Date', 'Time', 'DOY', 'X', 'Y', 'Z', 'F']
```

```

data['Hour'] = pd.to_datetime(data['Time'], format='%H:%M:%S.%f').dt.hour
data['Min'] = pd.to_datetime(data['Time'], format='%H:%M:%S.%f').dt.minute
data['Sec'] = pd.to_datetime(data['Time'], format='%H:%M:%S.%f').dt.second
return data

def bandpass_filter(data, min, max, fs, order=4):
    low = 2*(min/fs)
    high = 2*(max/fs)
    b, a = sci.butter(order, [low, high], btype='band')
    ready = sci.filtfilt(b, a, data)
    return ready

def lowpass_filter(data, max, fs, order=4):
    max = 2*(max/fs)
    b, a = sci.butter(order, max, btype='low')
    ready = sci.filtfilt(b, a, data)
    return ready

def isnan(df):
    if np.isnan(df):
        return 0
    else:
        return 1

def smooth(x):
    percentage = 0.005
    window_lengths = 51 #int(len(x)*percentage) # previously
    polyorders = 3
    amp_max1 = x.max()
    y = sci.savgol_filter(x, window_length=window_lengths, polyorder=polyorders, mode = 'interp')
    amp_max2 = y.max()
    factor = amp_max1/amp_max2
    y = y*factor
    return y

def count(df):
    if (df['MLT']*15 > 0) & (df['MLT']*15 <= 45):
        return 1
    elif (df['MLT']*15 > 45) & (df['MLT']*15 <= 90):
        return 2
    elif (df['MLT']*15 > 90) & (df['MLT']*15 <= 135):
        return 3
    elif (df['MLT']*15 > 135) & (df['MLT']*15 <= 180):
        return 4
    elif (df['MLT']*15 > 180) & (df['MLT']*15 <= 225):
        return 5

```

```

    elif (df['MLT']*15 > 225) & (df['MLT']*15 <= 270):
        return 6
    elif (df['MLT']*15 > 270) & (df['MLT']*15 <= 315):
        return 7
    else:
        return 8

<>:3: SyntaxWarning: invalid escape sequence '\s'
<>:9: SyntaxWarning: invalid escape sequence '\s'
<>:3: SyntaxWarning: invalid escape sequence '\s'
<>:9: SyntaxWarning: invalid escape sequence '\s'
C:\Users\Amal Marzooq\AppData\Local\Temp\ipykernel_25720\3726734472.py:3:
SyntaxWarning: invalid escape sequence '\s'
    data = pd.read_csv(destination, sep='\s+')#delim_whitespace=True)
C:\Users\Amal Marzooq\AppData\Local\Temp\ipykernel_25720\3726734472.py:9:
SyntaxWarning: invalid escape sequence '\s'
    data = pd.read_fwf(destination, sep = '\s+', header = None)

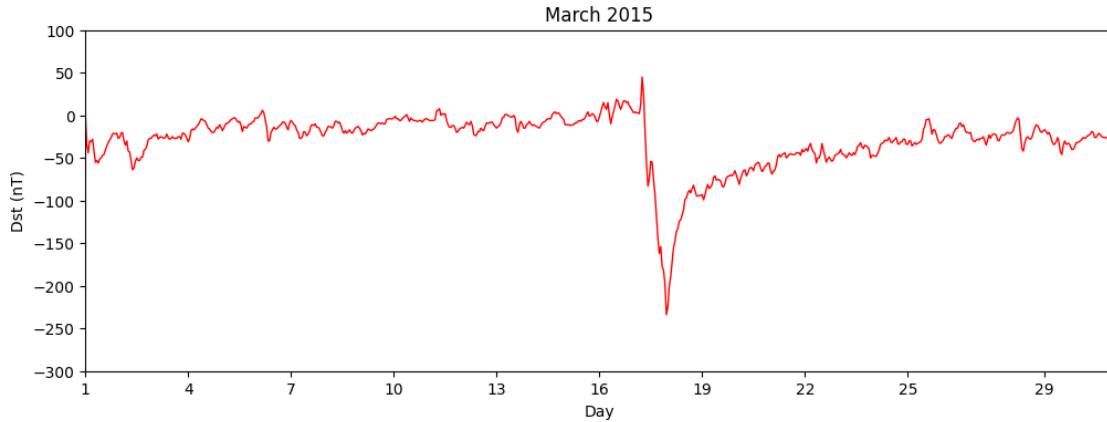
```

Overall Storm Features

The Dst Index

[6]: dst = pd.read_csv('new.csv', header = None, names = ['hour', 'dst', 'time'])

[7]: %%matplotlib qt
plt.figure(figsize = (12,4))
plt.plot(dst['time'], dst['dst'], linewidth = 1, c= 'r')
#plt.axvspan(17, 22, color='yellow', alpha=0.3, label='Highlighted Region')
plt.xlim(1,31)
plt.ylabel('Dst (nT)')
plt.xlabel('Day')
plt.yticks([100, 50, 0, -50, -100, -150, -200, -250, -300])
plt.xticks([1, 4, 7, 10, 13, 16, 19, 22, 25, 29])
mplcursors.cursor(hover=True);
plt.title('March 2015')
plt.show()
plt.savefig('Dst.png')



```
[8]: sw = file_read_sw('SW.txt')
sw['time'] = sw['HR'] + sw['MN']/60
sw['day'] = sw.apply(day, axis = 1)

sw['Bx'] = sw['Bx'].mask(sw['Bx'] >= 9999.99).interpolate('linear')
sw['By'] = sw['By'].mask(sw['By'] >= 9999.99).interpolate('linear')
sw['Bz'] = sw['Bz'].mask(sw['Bz'] >= 9999.99).interpolate('linear')
sw['Vx'] = sw['Vx'].mask(sw['Vx'] >= 99999.9).interpolate('linear')
sw['Vy'] = sw['Vy'].mask(sw['Vy'] >= 99999.9).interpolate('linear')
sw['Vz'] = sw['Vz'].mask(sw['Vz'] >= 99999.9).interpolate('linear')
sw['Rho'] = sw['Rho'].mask(sw['Rho'] >= 999.99).interpolate('linear')
sw['Temp'] = sw['Temp'].mask(sw['Temp'] >= 999999.).interpolate('linear')
sw['P'] = sw['P'].mask(sw['P'] >= 99.99).interpolate('linear')
sw['AL'] = sw['AL'].mask(sw['AL'] >= 99999).interpolate('linear')
```

```
[9]: data_ASC = IAGA_file_read(fileName = 'data/ASC/asc20150317psec.txt')
data_GUA = IAGA_file_read(fileName = 'data/GUA/gua20150317vsec.txt')
data_DLT = IAGA_file_read2(fileName = 'data/DLT/dlt20150317qsec.txt')
data_KOU = IAGA_file_read2(fileName = 'data/KOU/kou20150317qsec.txt')
```

```
[10]: # Extracting the data of interest and reforming time:
myTable_ASC = pd.DataFrame()
myTable_ASC['tm'] = data_ASC['Sec']/3600 + data_ASC['Min']/60 + data_ASC['Hour']
myTable_ASC['H'] = data_ASC['H'] #np.sqrt(data['X']**2+data['Y']**2)
myTable_ASC

# Replace missing values (>= 8e4) with NaN -> IAGA standards: nulls are assigned ↴ the value 88888 or 99999:
myTable_ASC = myTable_ASC.mask(myTable_ASC > 80000)

myTable_ASC['H'] = myTable_ASC['H'] - myTable_ASC['H'].mean(skipna = True) ↴
#returns the mean while skipping nan values
```

```

#-----

myTable_GUA = pd.DataFrame()
myTable_GUA['tm'] = data_GUA['Sec']/3600 + data_GUA['Min']/60 + data_GUA['Hour']
myTable_GUA['H'] = data_GUA['H'] #np.sqrt(data['X']**2+data['Y']**2)
myTable_GUA

# Replace missing values (>= 8e4) with NaN -> IAGA standards: nulls are assigned
→the value 88888 or 99999:

myTable_GUA = myTable_GUA.mask(myTable_GUA > 80000)

myTable_GUA['H'] = myTable_GUA['H'] - myTable_GUA['H'].mean(skipna = True)
→#returns the mean while skipping nan values

#-----
```

```

myTable_DLT = pd.DataFrame()
myTable_DLT['tm'] = data_DLT['Sec']/3600 + data_DLT['Min']/60 + data_DLT['Hour']
myTable_DLT['H'] = np.sqrt(data_DLT['X']**2+data_DLT['Y']**2)
myTable_DLT

# Replace missing values (>= 8e4) with NaN -> IAGA standards: nulls are assigned
→the value 88888 or 99999:

myTable_DLT = myTable_DLT.mask(myTable_DLT > 80000)

myTable_DLT['H'] = myTable_DLT['H'] - myTable_DLT['H'].mean(skipna = True)
→#returns the mean while skipping nan values

#-----
```

```

myTable_KOU = pd.DataFrame()
myTable_KOU['tm'] = data_KOU['Sec']/3600 + data_KOU['Min']/60 + data_KOU['Hour']
myTable_KOU['H'] = np.sqrt(data_KOU['X']**2+data_KOU['Y']**2)
myTable_KOU

# Replace missing values (>= 8e4) with NaN -> IAGA standards: nulls are assigned
→the value 88888 or 99999:

myTable_KOU = myTable_KOU.mask(myTable_KOU > 80000)

myTable_KOU['H'] = myTable_KOU['H'] - myTable_KOU['H'].mean(skipna = True)
→#returns the mean while skipping nan values
```

[11]:

```

start = 0
end = 24

duration_ASC = (myTable_ASC['tm'] > start) & (myTable_ASC['tm'] < end)
```

```
Bh_ASC = myTable_ASC['H'][duration_ASC]
tm_ASC = myTable_ASC['tm'][duration_ASC]
tm_ASC = tm_ASC.reset_index(drop=True)
Bh_ASC = Bh_ASC.interpolate('linear')
tm_ASC = tm_ASC.interpolate('linear')

duration_GUA = (myTable_GUA['tm'] > start) & (myTable_GUA['tm'] < end)
Bh_GUA = myTable_GUA['H'][duration_GUA]
tm_GUA = myTable_GUA['tm'][duration_GUA]
tm_GUA = tm_GUA.reset_index(drop=True)
Bh_GUA = Bh_GUA.interpolate('linear')
tm_GUA = tm_GUA.interpolate('linear')

duration_DLT = (myTable_DLT['tm'] > start) & (myTable_DLT['tm'] < end)
Bh_DLT = myTable_DLT['H'][duration_DLT]
tm_DLT = myTable_DLT['tm'][duration_DLT]
tm_DLT = tm_DLT.reset_index(drop=True)
Bh_DLT = Bh_DLT.interpolate('linear')
tm_DLT = tm_DLT.interpolate('linear')

duration_KOU = (myTable_KOU['tm'] > start) & (myTable_KOU['tm'] < end)
Bh_KOU = myTable_KOU['H'][duration_KOU]
tm_KOU = myTable_KOU['tm'][duration_KOU]
tm_KOU = tm_KOU.reset_index(drop=True)
Bh_KOU = Bh_KOU.interpolate('linear')
tm_KOU = tm_KOU.interpolate('linear')
```

SW Parameters and Stations Plots

```
[13]: %%matplotlib qt
# Making sure the data is fine:
plt.figure(figsize=(10,8))

plt.subplot(5,1,1)
x = sw[sw['day'] == 17]['time']
y = sw[sw['day'] == 17]['Bz']
plt.plot(x,y, linewidth = 0.7, c = 'red')
plt.xlim(0,max(x))
plt.xlabel('Time (UT)')
plt.ylabel('IMF Bz (nT)')
plt.title('Date: 17-03-2015')
mplcursors.cursor(hover=True);

# plt.subplot(5,1,1)
# x = sw[sw['day'] == 17]['time']
# y = sw[sw['day'] == 17]['Vz']
```

```

# plt.plot(x,y, linewidth = 0.7, c = 'red')
#plt.xlim(0,max(x))
#plt.xlabel('Time (UT)')
#plt.ylabel('Vz (km/s)')
#plt.title('Date: 17-03-2015')
#mplcursors.cursor(hover=True);

# plt.subplot(5,1,1)
#x = sw[sw['day'] == 17]['time']
#y = sw[sw['day'] == 17]['Vx']
#plt.plot(x,y, linewidth = 0.7, c = 'red')
#plt.xlim(0,max(x))
#plt.xlabel('Time (UT)')
#plt.ylabel('Vx (km/s)')
#plt.title('Date: 17-03-2015')
#mplcursors.cursor(hover=True);

# plt.subplot(5,1,1)
#x = sw[sw['day'] == 17]['time']
#y = sw[sw['day'] == 17]['Vy']
#plt.plot(x,y, linewidth = 0.7, c = 'red')
#plt.xlim(0,max(x))
#plt.xlabel('Time (UT)')
#plt.ylabel('Vy (km/s)')
#plt.title('Date: 17-03-2015')
#mplcursors.cursor(hover=True);

# plt.subplot(5,1,1)
#x = sw[sw['day'] == 17]['time']
#y = sw[sw['day'] == 17]['AL']
#plt.plot(x,y, linewidth = 0.7, c = 'red')
#plt.xlim(0,max(x))
#plt.xlabel('Time (UT)')
#plt.ylabel('AL (nT)')
#plt.title('Date: 17-03-2015')
#mplcursors.cursor(hover=True);

plt.subplot(5,1,2)
plt.plot(tm_ASC, Bh_ASC, 'blue', linewidth = 0.7)
plt.xlabel('Time (UT)')
plt.ylabel('H (nT), ASC')
#plt.title('ASC')
plt.xlim(0,max(tm_ASC))
#plt.axvspan(4.5, 5.0, alpha = 0.5, color = '#FFFF00')

```

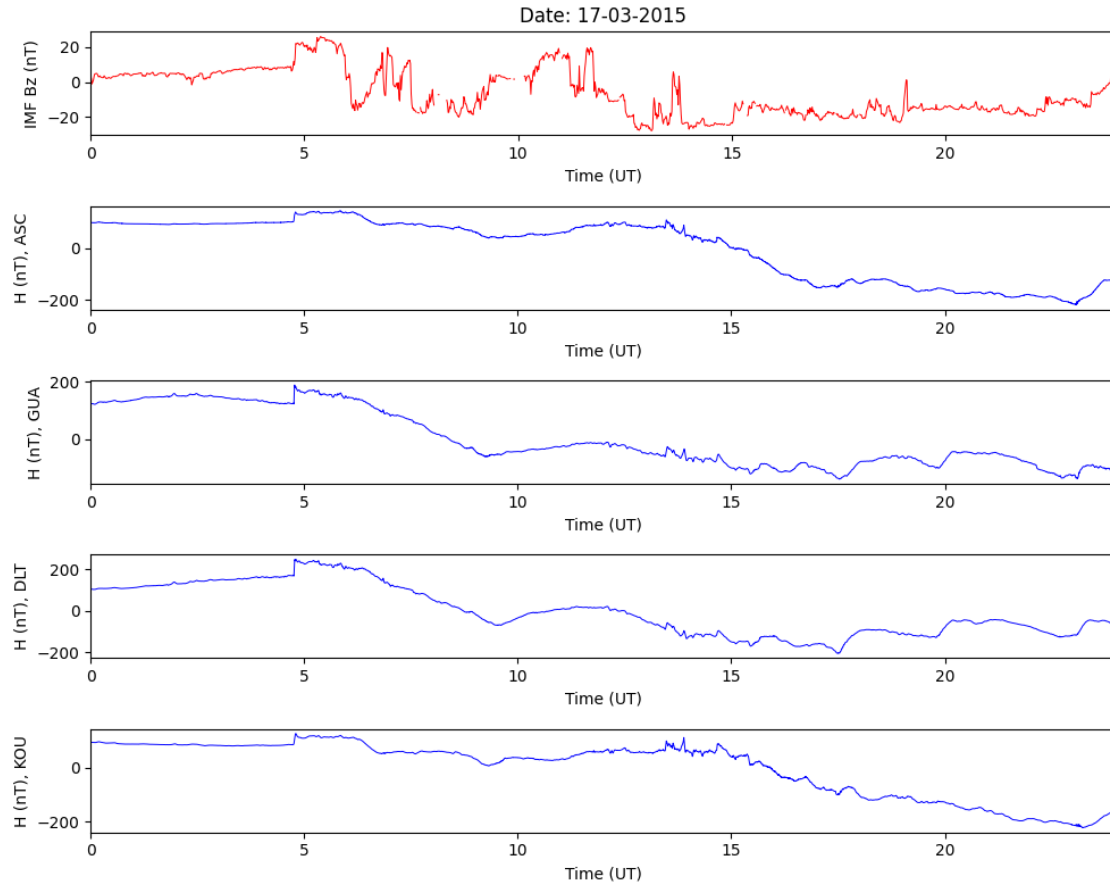
```
plt.subplot(5,1,3)
plt.plot(tm_GUA, Bh_GUA, 'blue', linewidth = 0.7)
plt.xlabel('Time (UT)')
plt.ylabel('H (nT), GUA')
#plt.title('GUA')
plt.xlim(0,max(tm_GUA))
#plt.axvspan(4.5, 5.0, alpha = 0.5, color = '#FFFF00')

plt.subplot(5,1,4)
plt.plot(tm_DLT, Bh_DLT, 'blue', linewidth = 0.7)
plt.xlabel('Time (UT)')
plt.ylabel('H (nT), DLT')
#plt.title('DLT')
plt.xlim(0,max(tm_DLT))
#plt.axvspan(4.5, 5.0, alpha = 0.5, color = '#FFFF00')

plt.subplot(5,1,5)
plt.plot(tm_KOU, Bh_KOU, 'blue', linewidth = 0.7)
plt.xlabel('Time (UT)')
plt.ylabel('H (nT), KOU')
#plt.title('KOU')
plt.xlim(0,max(tm_KOU))
#plt.axvspan(4.5, 5.0, alpha = 0.5, color = '#FFFF00')

plt.tight_layout()
#plt.savefig('AL.png')
plt.show()
```

<Figure size 640x480 with 0 Axes>



The SSC Analysis

```
[15]: start = 4
end = 6

duration_ASC = (myTable_ASC['tm'] > start) & (myTable_ASC['tm'] < end)
Bh_ASC = myTable_ASC['H'][duration_ASC]
tm_ASC = myTable_ASC['tm'][duration_ASC]
tm_ASC = tm_ASC.reset_index(drop=True)
Bh_ASC = Bh_ASC.interpolate('linear')
tm_ASC = tm_ASC.interpolate('linear')

duration_GUA = (myTable_GUA['tm'] > start) & (myTable_GUA['tm'] < end)
Bh_GUA = myTable_GUA['H'][duration_GUA]
tm_GUA = myTable_GUA['tm'][duration_GUA]
tm_GUA = tm_GUA.reset_index(drop=True)
Bh_GUA = Bh_GUA.interpolate('linear')
tm_GUA = tm_GUA.interpolate('linear')
```

```

duration_DLT = (myTable_DLT['tm'] > start) & (myTable_DLT['tm'] < end)
Bh_DLT = myTable_DLT['H'][duration_DLT]
tm_DLT = myTable_DLT['tm'][duration_DLT]
tm_DLT = tm_DLT.reset_index(drop=True)
Bh_DLT = Bh_DLT.interpolate('linear')
tm_DLT = tm_DLT.interpolate('linear')

duration_KOU = (myTable_KOU['tm'] > start) & (myTable_KOU['tm'] < end)
Bh_KOU = myTable_KOU['H'][duration_KOU]
tm_KOU = myTable_KOU['tm'][duration_KOU]
tm_KOU = tm_KOU.reset_index(drop=True)
Bh_KOU = Bh_KOU.interpolate('linear')
tm_KOU = tm_KOU.interpolate('linear')

```

[16]:

```

fs = 1
plt.figure(figsize=(12,10))

pi2_ASC = bandpass_filter(Bh_ASC, 0.002, 0.025, fs)

plt.subplot(6,2,1)
plt.plot(tm_ASC, pi2_ASC, 'r', linewidth=0.7)
plt.title('ASC')
plt.xlabel('Time (UT)')
plt.ylabel('H (nT)')

plt.subplot(6,2,2)
nfft = 2**9
f,t,p = sci.spectrogram(pi2_ASC, fs = fs, nperseg = 2**8, noverlap = 0.45*nfft, nfft = nfft)
t = t/3600 + start
plt.pcolormesh(t, f*1000, 10*np.log10(p), shading='gouraud', cmap='jet')
plt.ylim(0,40)
plt.ylabel('Frequency (mHz)')
plt.xlabel('Time (UT)')
plt.colorbar(label='Power (dB/Hz)')
plt.clim(-20,15)
plt.title('ASC')

pi2_GUA = bandpass_filter(Bh_GUA, 0.002, 0.025, fs)

plt.subplot(6,2,3)
plt.plot(tm_GUA, pi2_GUA, 'r', linewidth=0.7)
plt.title('GUA')
plt.xlabel('Time (UT)')
plt.ylabel('H (nT)')

```

```

plt.subplot(6,2,4)
nfft = 2**9
f,t,p = sci.spectrogram(pi2_GUA, fs = fs, nperseg = 2**8, noverlap = 0.45*nfft, nfft = nfft)
t = t/3600 + start
plt.pcolormesh(t, f*1000, 10*np.log10(p), shading='gouraud', cmap='jet')
plt.ylim(0,40)
plt.ylabel('Frequency (mHz)')
plt.xlabel('Time (UT)')
plt.colorbar(label='Power (dB/Hz)')
plt.clim(-20,15)
plt.title('GUA')

pi2_DLT = bandpass_filter(Bh_DLT, 0.002, 0.025, fs)

plt.subplot(6,2,5)
plt.plot(tm_DLT, pi2_DLT, 'r', linewidth=0.7)
plt.title('DLT')
plt.xlabel('Time (UT)')
plt.ylabel('H (nT)')

plt.subplot(6,2,6)
nfft = 2**9
f,t,p = sci.spectrogram(pi2_DLT, fs = fs, nperseg = 2**8, noverlap = 0.45*nfft, nfft = nfft)
t = t/3600 + start
plt.pcolormesh(t, f*1000, 10*np.log10(p), shading='gouraud', cmap='jet')
plt.ylim(0,40)
plt.ylabel('Frequency (mHz)')
plt.xlabel('Time (UT)')
plt.colorbar(label='Power (dB/Hz)')
plt.clim(-20,15)
plt.title('DLT')

pi2_KOU = bandpass_filter(Bh_KOU, 0.002, 0.025, fs)

plt.subplot(6,2,7)
plt.plot(tm_KOU, pi2_KOU, 'r', linewidth=0.7)
plt.title('KOU')
plt.xlabel('Time (UT)')
plt.ylabel('H (nT)')

plt.subplot(6,2,8)
nfft = 2**9
f,t,p = sci.spectrogram(pi2_KOU, fs = fs, nperseg = 2**8, noverlap = 0.45*nfft, nfft = nfft)
t = t/3600 + start

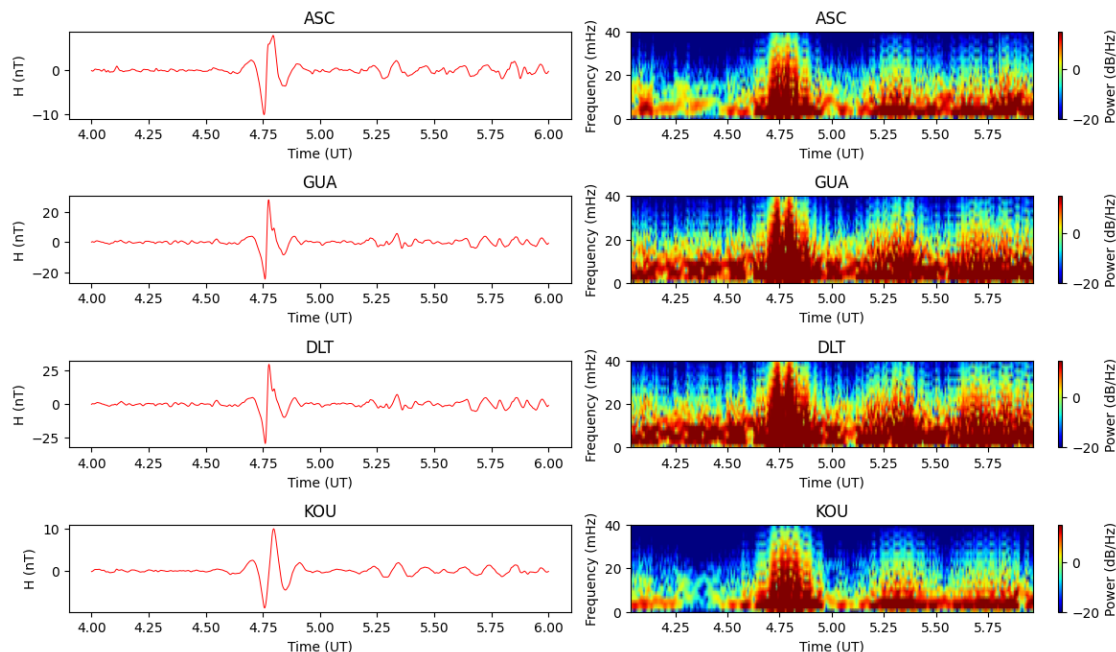
```

```

plt.pcolormesh(t, f*1000, 10*np.log10(p), shading='gouraud', cmap='jet')
plt.ylim(0,40)
plt.ylabel('Frequency (mHz)')
plt.xlabel('Time (UT)')
plt.colorbar(label='Power (dB/Hz)')
plt.clim(-20,15)
plt.title('KOU')

plt.tight_layout()
plt.savefig('ssc.png')
plt.show()

```



The Pi2 Signal

[18]:

```

data_ASC = IAGA_file_read(fileName = 'data/ASC/asc20150316psec.txt')
data_GUA = IAGA_file_read(fileName = 'data/GUA/gua20150316vsec.txt')
data_DLT = IAGA_file_read2(fileName = 'data/DLT/dlt20150316qsec.txt')
data_KOU = IAGA_file_read2(fileName = 'data/KOU/kou20150316qsec.txt')

```

[19]:

```

# Extracting the data of interest and reforming time:
myTable_ASC = pd.DataFrame()
myTable_ASC['tm'] = data_ASC['Sec']/3600 + data_ASC['Min']/60 + data_ASC['Hour']
myTable_ASC['H'] = data_ASC['H'] #np.sqrt(data['X']**2+data['Y']**2)
myTable_ASC

```

```

# Replace missing values (>= 8e4) with NaN -> IAGA standards: nulls are assigned
# to the value 88888 or 99999:
myTable_ASC = myTable_ASC.mask(myTable_ASC > 80000)

myTable_ASC['H'] = myTable_ASC['H'] - myTable_ASC['H'].mean(skipna = True)
#returns the mean while skipping nan values

#-----

myTable_GUA = pd.DataFrame()
myTable_GUA['tm'] = data_GUA['Sec']/3600 + data_GUA['Min']/60 + data_GUA['Hour']
myTable_GUA['H'] = data_GUA['H'] #np.sqrt(data['X']**2+data['Y']**2)
myTable_GUA

# Replace missing values (>= 8e4) with NaN -> IAGA standards: nulls are assigned
# to the value 88888 or 99999:
myTable_GUA = myTable_GUA.mask(myTable_GUA > 80000)

myTable_GUA['H'] = myTable_GUA['H'] - myTable_GUA['H'].mean(skipna = True)
#returns the mean while skipping nan values

#-----

myTable_DLT = pd.DataFrame()
myTable_DLT['tm'] = data_DLT['Sec']/3600 + data_DLT['Min']/60 + data_DLT['Hour']
myTable_DLT['H'] = np.sqrt(data_DLT['X']**2+data_DLT['Y']**2)
myTable_DLT

# Replace missing values (>= 8e4) with NaN -> IAGA standards: nulls are assigned
# to the value 88888 or 99999:
myTable_DLT = myTable_DLT.mask(myTable_DLT > 80000)

myTable_DLT['H'] = myTable_DLT['H'] - myTable_DLT['H'].mean(skipna = True)
#returns the mean while skipping nan values

#-----

myTable_KOU = pd.DataFrame()
myTable_KOU['tm'] = data_KOU['Sec']/3600 + data_KOU['Min']/60 + data_KOU['Hour']
myTable_KOU['H'] = np.sqrt(data_KOU['X']**2+data_KOU['Y']**2)
myTable_KOU

# Replace missing values (>= 8e4) with NaN -> IAGA standards: nulls are assigned
# to the value 88888 or 99999:
myTable_KOU = myTable_KOU.mask(myTable_KOU > 80000)

```

```
myTable_KOU['H'] = myTable_KOU['H'] - myTable_KOU['H'].mean(skipna = True)
    ↵#returns the mean while skipping nan values
```

```
[20]: start = 2
end = 4

duration_ASC = (myTable_ASC['tm'] > start) & (myTable_ASC['tm'] < end)
Bh_ASC = myTable_ASC['H'][duration_ASC]
tm_ASC = myTable_ASC['tm'][duration_ASC]
tm_ASC = tm_ASC.reset_index(drop=True)
Bh_ASC = Bh_ASC.interpolate('linear')
tm_ASC = tm_ASC.interpolate('linear')

duration_GUA = (myTable_GUA['tm'] > start) & (myTable_GUA['tm'] < end)
Bh_GUA = myTable_GUA['H'][duration_GUA]
tm_GUA = myTable_GUA['tm'][duration_GUA]
tm_GUA = tm_GUA.reset_index(drop=True)
Bh_GUA = Bh_GUA.interpolate('linear')
tm_GUA = tm_GUA.interpolate('linear')

duration_DLT = (myTable_DLT['tm'] > start) & (myTable_DLT['tm'] < end)
Bh_DLT = myTable_DLT['H'][duration_DLT]
tm_DLT = myTable_DLT['tm'][duration_DLT]
tm_DLT = tm_DLT.reset_index(drop=True)
Bh_DLT = Bh_DLT.interpolate('linear')
tm_DLT = tm_DLT.interpolate('linear')

duration_KOU = (myTable_KOU['tm'] > start) & (myTable_KOU['tm'] < end)
Bh_KOU = myTable_KOU['H'][duration_KOU]
tm_KOU = myTable_KOU['tm'][duration_KOU]
tm_KOU = tm_KOU.reset_index(drop=True)
Bh_KOU = Bh_KOU.interpolate('linear')
tm_KOU = tm_KOU.interpolate('linear')
```

```
[21]: fs = 1
plt.figure(figsize=(10,10))

plt.subplot(6,1,1)
x = sw[(sw['day'] == 16)&(sw['time']>= start)&(sw['time']<=end)][['time']]
y = sw[(sw['day'] == 16)&(sw['time']>= start)&(sw['time']<=end)][['AL']]
plt.plot(x,y, linewidth = 0.7, c = 'red')
plt.xlim(start,end)
plt.xlabel('Time (UT)')
plt.ylabel('AL (nT)')
plt.title('Date: 16-03-2015')
mplcursors.cursor(hover=True);
```

```
pi2_ASC = bandpass_filter(Bh_ASC, 0.002, 0.025, fs)

plt.subplot(6,1,2)
plt.plot(tm_ASC, pi2_ASC, 'r', linewidth=0.7)
plt.title('ASC')
plt.xlabel('Time (UT)')
plt.ylabel('H (nT)')
plt.xlim(start,end)

pi2_GUA = bandpass_filter(Bh_GUA, 0.002, 0.025, fs)

plt.subplot(6,1,3)
plt.plot(tm_GUA, pi2_GUA, 'r', linewidth=0.7)
plt.title('GUA')
plt.xlabel('Time (UT)')
plt.ylabel('H (nT)')
plt.xlim(start,end)

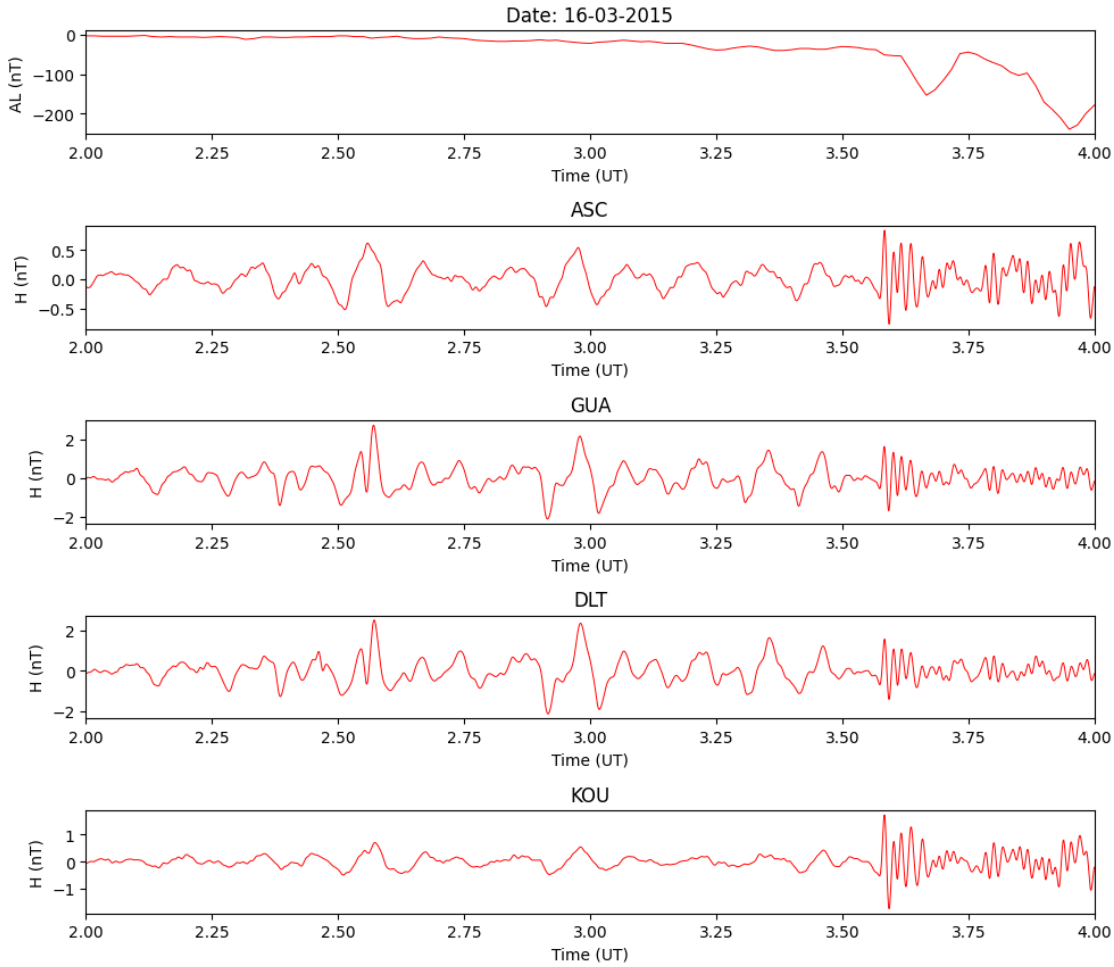
pi2_DLT = bandpass_filter(Bh_DLT, 0.002, 0.025, fs)

plt.subplot(6,1,4)
plt.plot(tm_DLT, pi2_DLT, 'r', linewidth=0.7)
plt.title('DLT')
plt.xlabel('Time (UT)')
plt.ylabel('H (nT)')
plt.xlim(start,end)

pi2_KOU = bandpass_filter(Bh_KOU, 0.002, 0.025, fs)

plt.subplot(6,1,5)
plt.plot(tm_KOU, pi2_KOU, 'r', linewidth=0.7)
plt.title('KOU')
plt.xlabel('Time (UT)')
plt.ylabel('H (nT)')
plt.xlim(start,end)

plt.tight_layout()
plt.savefig('pictures/Storm_analysis/pi2-16-3-2015.png')
plt.show()
```



MLT of Stations

```
[23]: # Load the image
image = mpimg.imread('pictures/earth3.png')

i = 4.8

#for i in range(24):
sec = 0
min = 0
hour = i
UT = hour + min/60 + sec/3600
r = [1, 1, 1, 1]

N_pole = -72.649
ASC = 57.47
```

```

GUA = -143.51
DLT = -178.93
KOU = -20.46
long = [ASC, GUA, DLT, KOU]

MLT_ASC = (UT + ASC/15 + N_pole/15)
MLT_GUA = (UT + GUA/15 + N_pole/15)
MLT_DLT = (UT + DLT/15 + N_pole/15)
MLT_KOU = (UT + KOU/15 + N_pole/15)
MLT = [MLT_ASC, MLT_GUA, MLT_DLT, MLT_KOU]

theta = []
for i in MLT:
    if i > 24:
        theta.append(i - 24)
    elif i < 0:
        theta.append(i + 24)
    else:
        theta.append(i)

fig, ax = plt.subplots(subplot_kw={'projection': 'polar'}, figsize = (8,8))
ax.set_theta_direction(1)
ax.plot(theta[0]*((15*np.pi)/180), r[0], 'o', markersize = 8, label = f'ASC_{theta[0]:.3} MLT', c = 'blue')
ax.plot(theta[1]*((15*np.pi)/180), r[1], 'o', markersize = 8, label = f'GUA_{theta[1]:.3} MLT', c = 'green')
ax.plot(theta[2]*((15*np.pi)/180), r[2], 'o', markersize = 8, label = f'DLT_{theta[2]:.3} MLT', c = 'red')
ax.plot(theta[3]*((15*np.pi)/180), r[3], 'o', markersize = 8, label = f'KOU_{theta[3]:.3} MLT', c = 'purple')
plt.legend() #bbox_to_anchor=(1.5, 1.1))
ax.set_rmax(2)
ax.set_rticks([0.5, 1, 1.5, 2])

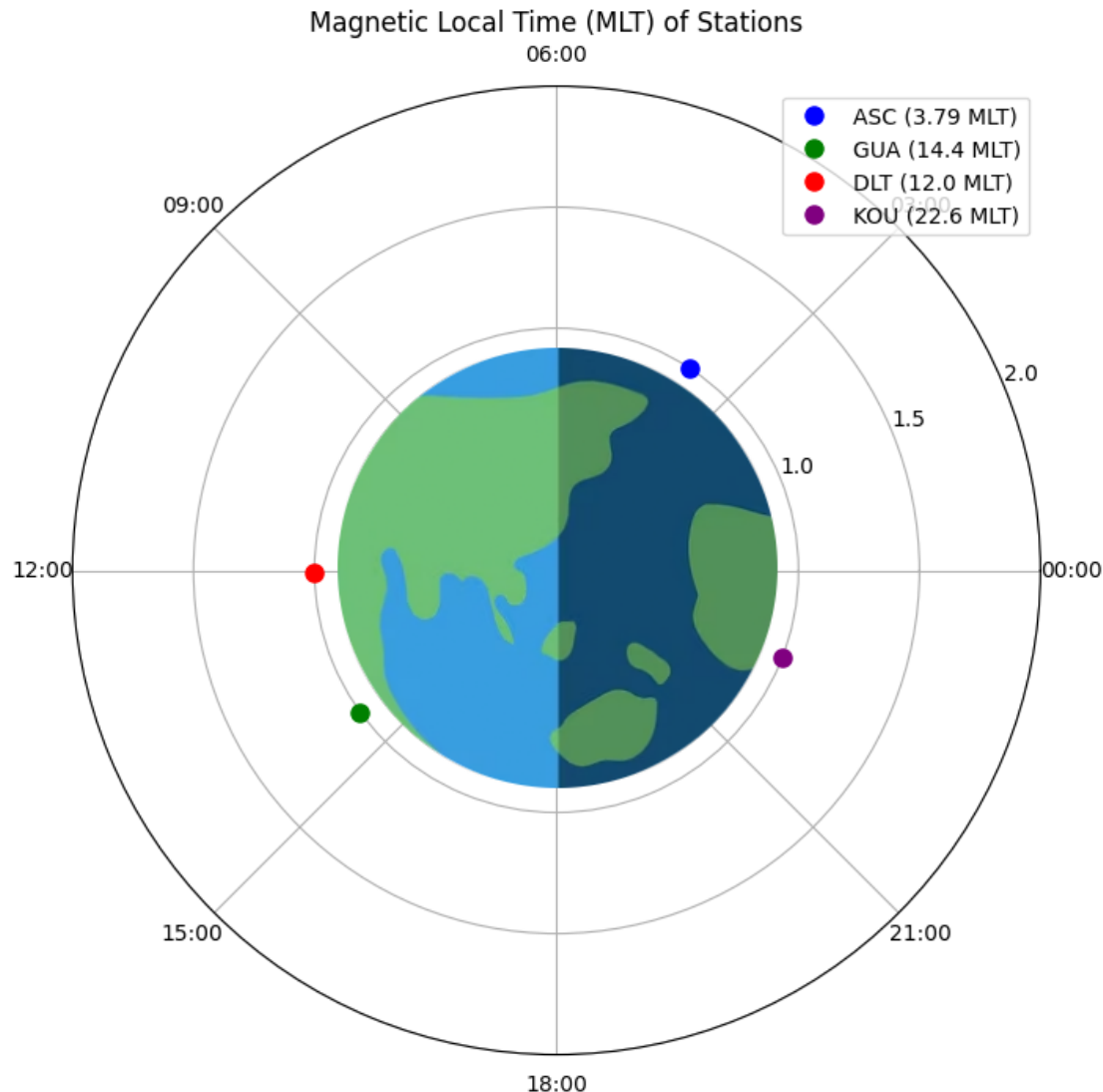
ax.set_xticks(np.linspace(0, 2 * np.pi, 8, endpoint=False)) # ticks positions
ax.set_xticklabels(['00:00', '03:00', '06:00', '09:00', '12:00', '15:00', '18:00', '21:00'])

# Set the position for the image
earth = fig.add_axes([0.338, 0.322, 0.35, 0.35], anchor='C', zorder=1) # [left, bottom, width, height]

earth.imshow(image)
earth.axis('off')

```

```
ax.set_title("Magnetic Local Time (MLT) of Stations")
plt.savefig('5-4.png')
plt.show()
```



Field-line Resonance Feature

```
[25]: data = IAGA_file_read(fileName = 'data/ASC/asc20150316psec.txt')

# Extracting the data of interest and reforming time:
myTable = pd.DataFrame()
myTable['tm'] = data['Sec']/3600 + data['Min']/60 + data['Hour']
myTable['H'] = data['H'] #np.sqrt(data['X']**2+data['Y']**2)
```

```

myTable

# Replace missing values (>= 8e4) with NaN -> IAGA standards: nulls are assigned
# to the value 88888 or 99999:
myTable = myTable.mask(myTable > 80000)

myTable['H'] = myTable['H'] - myTable['H'].mean(skipna = True) #returns the mean
# while skipping nan values

start = 14
end = 22
duration = (myTable['tm'] > start) & (myTable['tm'] < end)
Bh = myTable['H'][duration]
tm = myTable['tm'][duration]
tm = tm.reset_index(drop=True)
Bh = Bh.interpolate('linear')
tm = tm.interpolate('linear')

fs = 1
Bh = lowpass_filter(Bh, 0.1, fs)
# For Pc3 (22-100 mHz)
pc3 = bandpass_filter(Bh, 0.022, 0.1, fs)
pc3 = smooth(pc3)

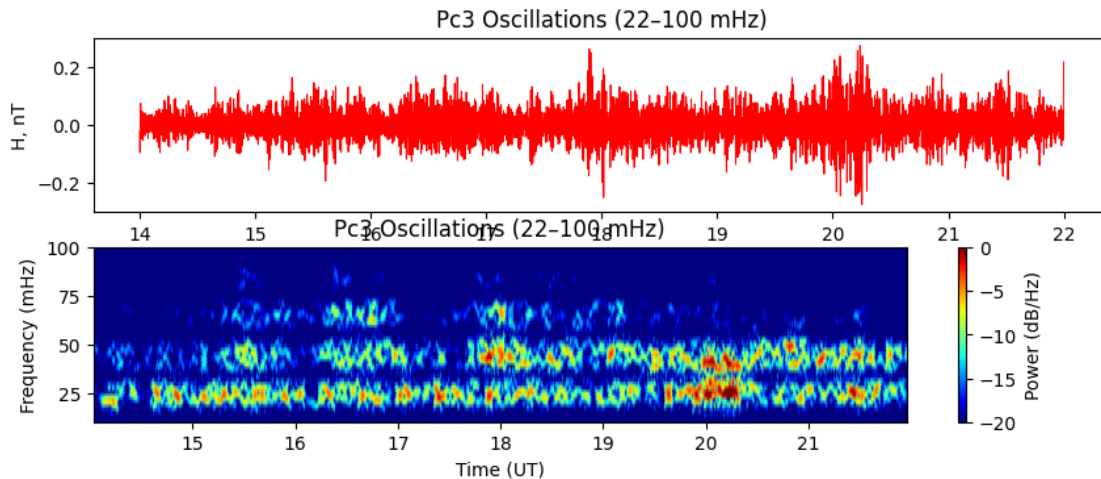
plt.figure(figsize=(10,10))

# Pc3 Signal
plt.subplot(5,1,1)
plt.plot(tm, pc3, 'r', linewidth=0.7)
plt.title('Pc3 Oscillations (22-100 mHz)')
plt.xlabel('Time in UT')
plt.ylabel('H, nT')

# Pc3 spectrogram:
plt.subplot(5,1,2)
fs = 1
nfft = 2**9
f,t,p = sci.spectrogram(pc3, fs = fs, nperseg = 2**8, noverlap = 0.45*nfft, nfft
# = nfft)
t = t/3600 + start
plt.pcolormesh(t, f*1000, 10*np.log10(p), shading='gouraud', cmap='jet')
plt.ylim(10,100)
plt.ylabel('Frequency (mHz)')
plt.xlabel('Time (UT)')
plt.colorbar(label='Power (dB/Hz)')
plt.clim(-20,0)
plt.title('Pc3 Oscillations (22-100 mHz)')

```

```
plt.show()  
plt.tight_layout()
```



The MLT Distribution of Pulsations

```
[27]: data = pd.read_csv("data/dataset.csv")
       data['date'] = pd.to_datetime(data['date'])
       data
```

```
[27]: Unnamed: 0      date    type   amplitude   start(UT)   end(UT)   Middle(UT) \
0          0 2015-03-14  pc4     0.540     23.521    23.653    23.587
1          1 2015-03-14  pc4     2.360     23.224    23.432    23.328
2          2 2015-03-14  pc3     0.324     23.248    23.316    23.282
3          3 2015-03-14  pc3     0.118     23.592    23.648    23.620
4          4 2015-03-14  pc4     0.314     0.127     0.258     0.193
..        ...
763       1211 2015-03-17  pc5     2.350     18.466    19.268    18.867
764       1214 2015-03-18  pc5     1.510     0.095     0.810     0.453
765       1219 2015-03-18  pc5     1.210     14.242    14.566    14.404
766       1220 2015-03-18  pc5     1.640     14.863    15.293    15.078
767       1223 2015-03-18  pc5     2.370     19.755    19.952    19.854

      Station code  latitude  longitude ...   SN        Bz        Vx \
0           ASC    -2.73     57.47 ...  55  1.381295 -462.652973
1           ASC    -2.73     57.47 ...  55  0.996939 -471.225260
2           ASC    -2.73     57.47 ...  55  0.886018 -472.438144
3           ASC    -2.73     57.47 ...  55  1.391707 -465.023529
4           ASC    -2.73     57.47 ...  55  0.943093 -477.306280
..        ...

```

```

763      KOU    14.27    -20.46 ... 38  0.837840 -472.457562
764      KOU    14.27    -20.46 ... 41  0.808771 -472.023567
765      KOU    14.27    -20.46 ... 41  0.100464 -478.008933
766      KOU    14.27    -20.46 ... 41  0.708000 -466.993036
767      KOU    14.27    -20.46 ... 41  0.426562 -462.296324

          Vy      Vz      Rho      Temp       P       AL   \
0  -11.241081 -10.874595 7.019135 99050.800000 2.552216 -151.029167
1  -14.555363 -10.767820 6.885952 100189.850694 2.567405 -165.655556
2  -12.882474 -11.036082 7.009175 100205.572917 2.605670 -172.183333
3  -10.842647 -10.832353 7.038382 99252.000000 2.548529 -146.733333
4  -14.042029 -10.124638 6.924928 118331.714976 2.734638 -129.883333
...
763  -9.935930 -13.457195 7.385738 97548.487580 3.018863 -123.874830
764  -14.674886 -9.603003 7.362002 109669.640511 2.786351 -125.316279
765  -2.830521 -14.271464 7.632705 109517.077114 3.412084 -207.587719
766  -3.253214 -15.526429 8.299607 101796.230357 3.543179 -197.837179
767  -14.437868 -8.027206 7.062059 83021.148148 2.748382 -97.911111

      MLT
0    22.575067
1    22.316067
2    22.270067
3    22.608067
4    23.181067
...
763  12.659733
764  18.245733
765  8.196733
766  8.870733
767  13.646733

```

[768 rows x 22 columns]

[28]: `data.groupby(['Station code'])['type'].count()`

[28]: Station code

ASC	165
DLT	185
GUA	205
KOU	213

Name: type, dtype: int64

[29]: `Quiet = data[(data['kp'] < 4) & (data['type'] != 'pi2') & (data['date'].dt.day < 17)]`

[30]: `Quiet.count()`

```
[30]: Unnamed: 0      358
date          358
type          358
amplitude    358
start(UT)    358
end(UT)      358
Middle(UT)   358
Station code 358
latitude     358
longitude    358
day          358
kp           358
SN           358
Bz           358
Vx           358
Vy           358
Vz           358
Rho          358
Temp         358
P            358
AL           358
MLT          358
dtype: int64
```

```
[31]: ang = Quiet.apply(count, axis = 1)
counts = ang.value_counts().sort_index(ascending=True)

angles = np.arange(0, 360, 45)

r = [2,2,2,2,2,2,2,2]

# Converting angles to radians for the polar plot
angles_rad = np.deg2rad(angles)

# Assigning counts for color intensity
norm = Normalize(vmin=np.min(counts), vmax=np.max(counts))
colors = cm.Blues(norm(counts))

# Create polar plot
fig, ax = plt.subplots(subplot_kw={'projection': 'polar'}, figsize = (8,8))
bars = ax.bar(angles_rad, r, color=colors, edgecolor='none', width=np.
              →deg2rad(45), alpha=0.85, align='edge')

ax.set_rticks([2])
ax.set_yticklabels([])
ax.set_xticks(np.linspace(0, 2 * np.pi, 8, endpoint=False)) # ticks positions
```

```
ax.set_xticklabels(['00:00', '03:00', '06:00', '09:00', '12:00', '15:00', '18:  
↪00', '21:00'])

# Setting the position for the image
earth = fig.add_axes([0.261, 0.32, 0.35, 0.35], anchor='C', zorder=1) # [left, u  
↪bottom, width, height]

earth.imshow(image)
earth.axis('off')

# Adding a colorbar
sm = plt.cm.ScalarMappable(cmap=cm.Blues, norm=norm)
sm.set_array([])
plt.colorbar(sm, ax=ax, label="Number of Evnts")

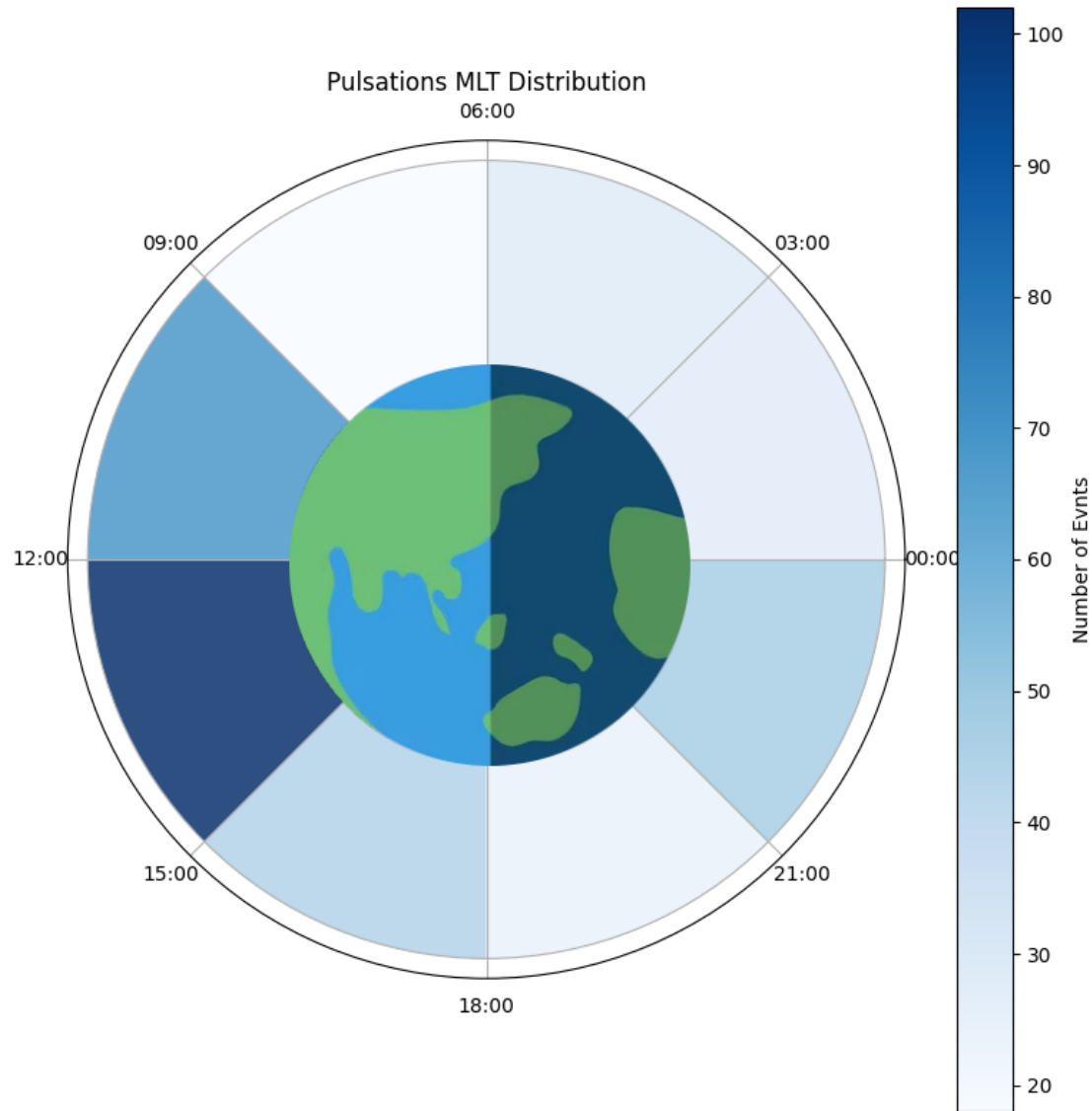
ax.set_title("Pulsations MLT Distribution")
plt.tight_layout()
plt.savefig('MLT distribution.png')
plt.show()
```

C:\Users\Amal Marzooq\AppData\Local\Temp\ipykernel_25720\2883423712.py:38:

UserWarning: This figure includes Axes that are not compatible with
tight_layout, so results might be incorrect.

 plt.tight_layout()

<Figure size 640x480 with 0 Axes>



The SW Parameters Scatter Plots

```
[33]: from scipy.signal import welch
seg = 3600
days = []
for i in range(1,8):
    days.append(i)

amplitudes = []
sw_velocity = []
sw_B = []
```

```

sw_T = []
sw_DP = []
sw_P = []
sw_R = []

days = [14, 15, 16, 17, 18]
for day in days:

    data_ASC = IAGA_file_read(fileName = f'data/ASC/asc201503{day}psec.txt')

    # Extracting the data of interest and reforming time:
    myTable_ASC = pd.DataFrame()
    myTable_ASC['tm'] = data_ASC['Sec']/3600 + data_ASC['Min']/60 + data_ASC['Hour']
    myTable_ASC['H'] = data_ASC['H'] #np.sqrt(data['X']**2+data['Y']**2)
    myTable_ASC

    # Replace missing values (>= 8e4) with NaN -> IAGA standards: nulls are assigned the value 88888 or 99999:
    myTable_ASC = myTable_ASC.mask(myTable_ASC > 80000)

    myTable_ASC['H'] = myTable_ASC['H'] - myTable_ASC['H'].mean(skipna = True) #returns the mean while skipping nan values

    start = 0
    end = 24

    duration_ASC = (myTable_ASC['tm'] > start) & (myTable_ASC['tm'] < end)
    Bh_ASC = myTable_ASC['H'][duration_ASC]
    tm_ASC = myTable_ASC['tm'][duration_ASC]
    tm_ASC = tm_ASC.reset_index(drop=True)
    Bh_ASC = Bh_ASC.interpolate('linear')
    tm_ASC = tm_ASC.interpolate('linear')

    # Filtered data:
    fs = 1.0 # Sampling frequency (Hz)
    pc3_ASC = bandpass_filter(Bh_ASC, 0.022, 0.1, fs)
    pc4_ASC = bandpass_filter(Bh_ASC, 0.007, 0.022, fs)
    pc5_ASC = bandpass_filter(Bh_ASC, 0.002, 0.007, fs)

    time = tm_ASC
    signal = pc3_ASC
    tm = tm_ASC

    # Define frequency band for Pc3 waves
    f_min, f_max = 0.022, 0.1#

```

```

# Segment signal into chunks for analysis
interval_length = int(seg) # 100-second intervals
num_intervals = len(signal) // interval_length

for i in range(num_intervals):

    start = i * interval_length
    end = start + interval_length
    segment = signal[start:end]

    # For solar wind velocity
    sw_velocity_avg_x = np.abs(sw[(sw['day'] == day)&(sw['time'] >
    tm[start])&(sw['time'] < tm[end])]['Vx']).mean()
    sw_velocity_avg_y = np.abs(sw[(sw['day'] == day)&(sw['time'] >
    tm[start])&(sw['time'] < tm[end])]['Vy']).mean()
    sw_velocity_avg_z = np.abs(sw[(sw['day'] == day)&(sw['time'] >
    tm[start])&(sw['time'] < tm[end])]['Vz']).mean()
    sw_velocity_avg = np.sqrt(sw_velocity_avg_x**2 + sw_velocity_avg_y**2 +
    sw_velocity_avg_z**2)
    sw_velocity.append(sw_velocity_avg)

    # For IMF magnitude
    sw_Bx = np.abs(sw[(sw['day'] == day)&(sw['time'] >
    tm[start])&(sw['time'] < tm[end])]['Bx']).mean(skipna = True)
    sw_By = np.abs(sw[(sw['day'] == day)&(sw['time'] >
    tm[start])&(sw['time'] < tm[end])]['By']).mean(skipna = True)
    sw_Bz = np.abs(sw[(sw['day'] == day)&(sw['time'] >
    tm[start])&(sw['time'] < tm[end])]['Bz']).mean(skipna = True)
    sw_B_avg = np.sqrt(sw_Bx**2 + sw_By**2 + sw_Bz**2)
    sw_B.append(sw_B_avg)

    # For solar wind temperature
    sw_Temp = np.abs(sw[(sw['day'] == day)&(sw['time'] >
    tm[start])&(sw['time'] < tm[end])]['Temp']).mean(skipna = True)
    sw_T.append(sw_Temp)

    # For solar wind dynamical pressure
    sw_pressure = np.abs(sw[(sw['day'] == day)&(sw['time'] >
    tm[start])&(sw['time'] < tm[end])]['P']).mean(skipna = True)
    sw_DP.append(sw_pressure)

    # For pressure variation

```

```

    sw_Rho = np.abs(sw[(sw['day'] == day)&(sw['time'] >
    ↵tm[start])&(sw['time'] < tm[end])]['Rho']).mean(skipna = True)
    sw_Vx = np.abs(sw[(sw['day'] == day)&(sw['time'] >
    ↵tm[start])&(sw['time'] < tm[end])]['Vx']).mean(skipna = True)
    sw_pres = 0.5*sw_Rho*sw_Vx**2*1e-6 # (converted to nPa)
    sw_P.append(sw_pres)

    # For solar wind density
    sw_density = np.abs(sw[(sw['day'] == day)&(sw['time'] >
    ↵tm[start])&(sw['time'] < tm[end])]['Rho']).mean(skipna = True)
    sw_R.append(sw_density)

    ↵
    ↵#-----#
    ↵

    frequencies, psd = welch(segment, fs, nperseg=2**9)

    # Integrate PSD over the desired frequency band
    band_indices = np.logical_and(frequencies >= f_min, frequencies <= f_max)
    wave_power = np.trapz(psd[band_indices], frequencies[band_indices])
    wave_amplitude = np.sqrt(wave_power)

    amplitudes.append(wave_amplitude)

    #
    # Compute FFT
    fft_result = np.fft.fft(segment)
    fft_freqs = np.fft.fftfreq(len(segment), d=1/fs)
    #

    # Compute Power Spectral Density (PSD)
    psd = np.abs(fft_result)**2 / len(segment)
    #

    # Select frequency band for Pc4 waves
    band_indices = (fft_freqs >= f_min) & (fft_freqs <= f_max)
    wave_power = np.sum(psd[band_indices]) # Sum power in the band
    #

    # Calculating the amplitude
    amplitude = np.sqrt(wave_power)
    amplitudes.append(amplitude)
    #-----#
df = pd.DataFrame()
df['amp'] = amplitudes
df['V'] = sw_velocity
df['B'] = sw_B
df['T'] = sw_T
df['DP']= sw_DP
df['P'] = sw_P

```

```

df['R'] = sw_R

#df = df[(df['amp'] > 0.3) & (df['amp'] < 10)]
df = df.dropna()

# Create scatter plot
plt.figure(figsize=(8, 8))
plt.subplot(2,2,1)

# Fitting the data with a linear regression:
amp = np.array(df['amp'])
val = np.array(df['V'])
m, c, r_value, p_value, std = linregress(val, amp)
y = m*np.abs(val) + c

plt.scatter(val, amp, alpha=0.7, edgecolor='k')
plt.plot(val, y, color='black', label='Linear fit', linewidth = 1)

equation_text = f'y = {m:.4f}x + {c:.4f} \n $R^2$ = {r_value**2:.4f}' 
plt.text(0.55, 0.85, equation_text, transform=plt.gca().transAxes, fontsize=6, color='black')
plt.xlabel('V (km/s)')
plt.ylabel('Amplitude (nT)')
plt.title('Solar Wind Speed')

plt.subplot(2,2,2)

# Fitting the data with a linear regression:
amp = np.array(df['amp'])
val = np.array(df['B'])
m, c, r_value, p_value, std = linregress(val, amp)
y = m*np.abs(val) + c

plt.scatter(val, amp, alpha=0.7, edgecolor='k')
plt.plot(val, y, color='black', label='Linear fit', linewidth = 1)

equation_text = f'y = {m:.4f}x + {c:.4f} \n $R^2$ = {r_value**2:.4f}' 
plt.text(0.55, 0.85, equation_text, transform=plt.gca().transAxes, fontsize=6, color='black')
plt.xlabel('B (nT)')
plt.ylabel('Amplitude (nT)')
plt.title('IMF B Magnitude ')

plt.subplot(2,2,3)

# Fitting the data with a linear regression:
amp = np.array(df['amp'])

```

```

val = np.array(df['T'])
m, c, r_value, p_value, std = linregress(val, amp)
y = m*np.abs(val) + c

plt.scatter(val, amp, alpha=0.7, edgecolor='k')
plt.plot(val, y, color='black', label='Linear fit', linewidth = 1)

equation_text = f'y = {m:.4f}x + {c:.4f} \n $R^2$ = {r_value**2:.4f}'
plt.text(0.55, 0.85, equation_text, transform=plt.gca().transAxes, fontsize=6, color='black')

plt.xlabel('T (K)')
plt.ylabel('Amplitude (nT)')
plt.title('Solar Wind Temperature')

plt.subplot(2,2,4)

# Fitting the data with a linear regression:
amp = np.array(df['amp'])
val = np.array(df['P'])
m, c, r_value, p_value, std = linregress(val, amp)
y = m*np.abs(val) + c

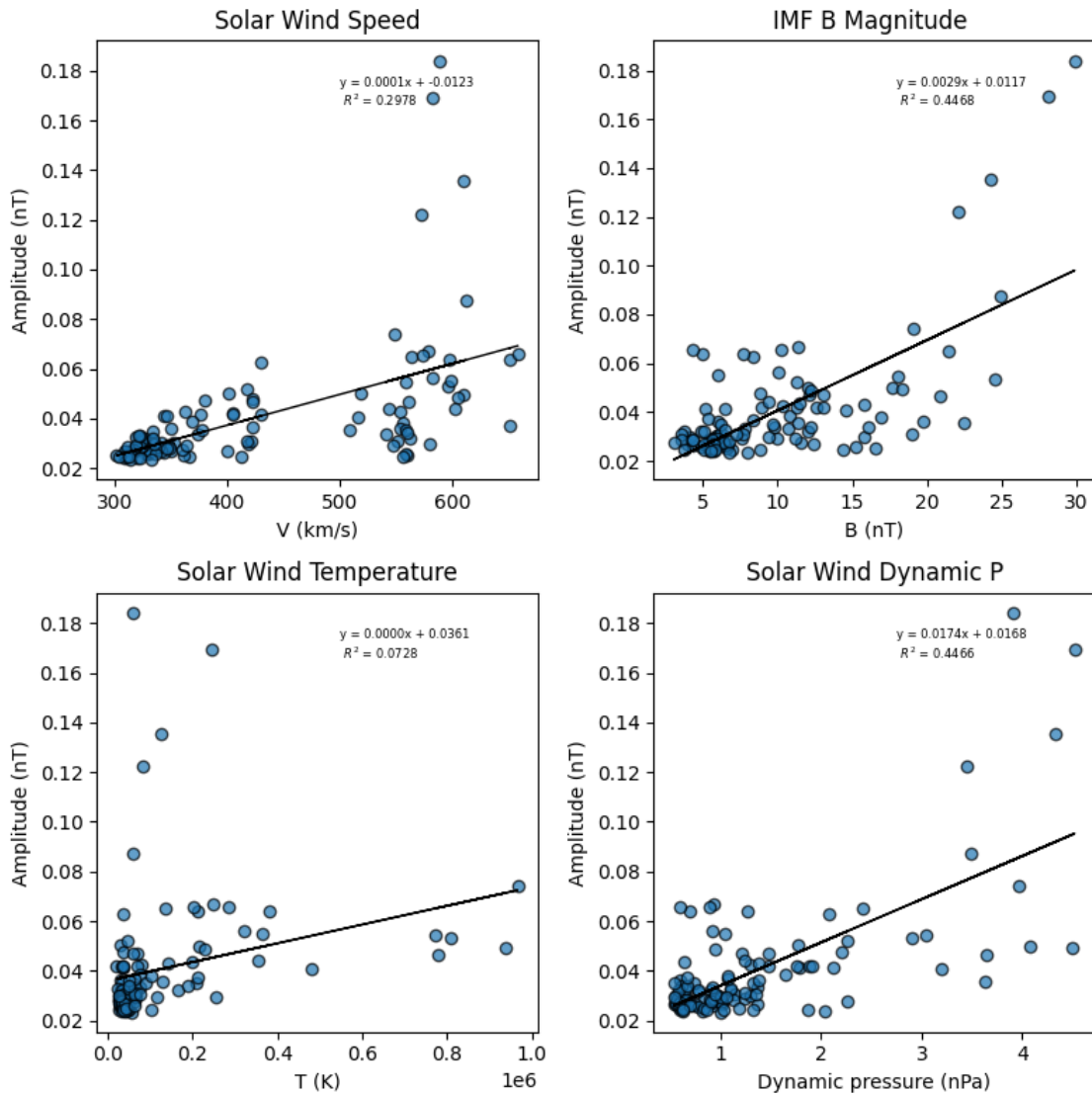
plt.scatter(val, amp, alpha=0.7, edgecolor='k')
plt.plot(val, y, color='black', label='Linear fit', linewidth = 1)

equation_text = f'y = {m:.4f}x + {c:.4f} \n $R^2$ = {r_value**2:.4f}'
plt.text(0.55, 0.85, equation_text, transform=plt.gca().transAxes, fontsize=6, color='black')

plt.xlabel('Dynamic pressure (nPa)')
plt.ylabel('Amplitude (nT)')
plt.title('Solar Wind Dynamic P')

plt.tight_layout()
plt.savefig('sw parameters.png')
plt.show()

```



Bibliography

- Akay, I. G., Kaymaz, Z., & Sibeck, D. G. (2019). Magnetotail boundary crossings at lunar distances: ARTEMIS observations. *Journal of Atmospheric and Solar-Terrestrial Physics*, 182, 45–60. <https://doi.org/10.1016/j.jastp.2018.11.002>
- Alfvén, H. (1942). Existence of Electromagnetic-Hydrodynamic waves. *Nature*, 150(3805), 405–406. <https://doi.org/10.1038/150405d0>
- Anderson, B. J. (1990). Ultra-low-frequency magnetic pulsations in the earth's magnetosphere. *Johns Hopkins APL technical digest*, 11, 239–254. <https://ntrs.nasa.gov/search.jsp?R=19910041034>
- Baker, D. N., Pulkkinen, T. I., Angelopoulos, V., Baumjohann, W., & McPherron, R. L. (1996). Neutral line model of substorms: Past results and present view. *Journal of Geophysical Research Atmospheres*, 101(A6), 12975–13010. <https://doi.org/10.1029/95ja03753>
- Baker, K. B., & Wing, S. (1989). A new magnetic coordinate system for conjugate studies at high latitudes. *Journal of Geophysical Research Atmospheres*, 94(A7), 9139–9143. <https://doi.org/10.1029/ja094ia07p09139>
- Borovsky, J. E., & Valdivia, J. A. (2018). The Earth's Magnetosphere: A Systems Science Overview and Assessment. *Surveys in Geophysics*, 39(5), 817–859. <https://doi.org/10.1007/s10712-018-9487-x>
- Boteler, D. H. (2019). A 21st century view of the March 1989 magnetic Storm. *Space Weather*, 17(10), 1427–1441. <https://doi.org/10.1029/2019sw002278>
- Bulusu, J., Chakravartula, P. S., Arora, K., & Rao, K. (2020). Statistical characteristics of low latitude Pc4s: Influence of solar wind and IMF parameters. *Advances in Space Research*, 65(7), 1685–1700. <https://doi.org/10.1016/j.asr.2020.01.001>
- Campbell, W., & Banerjee, S. (1998). Introduction to geomagnetic fields. *Physics Today*, 51, 55. <https://doi.org/10.1063/1.882493>
- Chen, F. F. (1984, January). *Introduction to plasma physics and controlled fusion*. <https://doi.org/10.1007/978-1-4757-5595-4>
- Coxon, J. C., Jackman, C. M., Freeman, M. P., Forsyth, C., & Rae, I. J. (2016). Identifying the magnetotail lobes with Cluster magnetometer data. *Journal of Geophysical Research Space Physics*, 121(2), 1436–1446. <https://doi.org/10.1002/2015ja022020>

- Dormy, E. (2006). The origin of the Earth's magnetic field: fundamental or environmental research? *Europhysics news*, 37(2), 22–25. <https://doi.org/10.1051/epn:2006202>
- Dungey, J. W. (1961). Interplanetary magnetic field and the auroral zones. *Physical Review Letters*, 6(2), 47–48. <https://doi.org/10.1103/physrevlett.6.47>
- Ganushkina, N. Y., Liemohn, M. W., & Dubyagin, S. (2018). Current systems in the Earth's magnetosphere. *Reviews of Geophysics*, 56(2), 309–332. <https://doi.org/10.1002/2017rg000590>
- GEOMAGNETIC INDICES BULLETIN* (tech. rep.). (2010, August). NATIONAL GEOPHYSICAL DATA CENTER.
- Gilbert, C. (2017). The kelvin-helmholtz instability in space. <https://api.semanticscholar.org/CorpusID:199456876>
- Gough, H., & Orr, D. (1984). The effect of damping on geomagnetic pulsation amplitude and phase at ground observatories. *Planetary and Space Science*, 32(5), 619–628. [https://doi.org/10.1016/0032-0633\(84\)90112-0](https://doi.org/10.1016/0032-0633(84)90112-0)
- Griffiths, D. J. (2017, June). *Introduction to Electrodynamics*. Cambridge University Press.
- Guo, Y., Ni, B., Fu, S., Wang, D., Shprits, Y. Y., Zhelavskaya, I. S., Feng, M., & Guo, D. (2021). Identification of controlling geomagnetic and solar wind factors for magnetospheric chorus intensity using feature selection techniques. *Journal of Geophysical Research Space Physics*, 127(1). <https://doi.org/10.1029/2021ja029926>
- Haq Wani, I., Saini, S., Sethi, M., & Angotra, P. (2021). A REVIEW OF IONOSPHERIC LAYERS AND GEOMAGNETIC STORMS. *Journal of Emerging Technologies and Innovative Research (JETIR)*, 8(8).
- Haralambous, H., & Papadopoulos, H. (2009). 24-Hour neural network congestion models for High-Frequency broadcast users. *IEEE Transactions on Broadcasting*, 55(1), 145–154. <https://doi.org/10.1109/tbc.2009.2013890>
- Heyns, M. J., Lotz, S. I., & Gaunt, C. T. (2020). Geomagnetic pulsations driving geomagnetically induced currents. *Space Weather*, 19(2). <https://doi.org/10.1029/2020sw002557>
- Houston, S. C. (2023, January). What are the Van Allen radiation belts? <https://spacecenter.org/what-are-the-van-allen-radiation-belts/>
- Hruška, A. (1969). On the interpretation of some observed features of geomagnetic pulsations. *Planetary and Space Science*, 17(12), 1937–1940. [https://doi.org/10.1016/0032-0633\(69\)90131-7](https://doi.org/10.1016/0032-0633(69)90131-7)
- IAGA 2002 Data Exchange Format. (2024, August). <https://www.ncei.noaa.gov/services/world-data-system/v-data-working-group/iaga-2002-data-exchange-format>
- Islam, S., & Islam, M. (2019). A comparative study on discrete fourier transformation for digital signal analysis. *01*, 18–26.
- Jwo, D.-J., Chang, W.-Y., & Wu, I.-H. (2021). Windowing techniques, the Welch method for improvement of power spectrum estimation. *Computers, materials continua/Computers, materials continua (Print)*, 67(3), 3983–4003. <https://doi.org/10.32604/cmc.2021.014752>
- Kamide, Y., Yokoyama, N., Gonzalez, W., Tsurutani, B. T., Daglis, I. A., Brekke, A., & Masuda, S. (1998). Two-step development of geomagnetic storms. *Journal of Geophysical Research Atmospheres*, 103(A4), 6917–6921. <https://doi.org/10.1029/97ja03337>
- Kepko, L., Spence, H. E., & Singer, H. J. (2002). ULF waves in the solar wind as direct drivers of magnetospheric pulsations. *Geophysical Research Letters*, 29(8). <https://doi.org/10.1029/2001gl014405>

- Kim, K.-C., Shprits, Y., Lee, J., & Hwang, J. (2013). Empirically modeled global distribution of magnetospheric chorus amplitude using an artificial neural network. *Journal of Geophysical Research Space Physics*, 118(10), 6243–6253. <https://doi.org/10.1002/jgra.50595>
- Kivelson, M. G., & Southwood, D. J. (1985). Resonant ULF waves: A new interpretation. *Geophysical Research Letters*, 12(1), 49–52. <https://doi.org/10.1029/gl012i001p00049>
- Kivelson, M. G., & Southwood, D. J. (1986). Coupling of global magnetospheric MHD eigenmodes to field line resonances. *Journal of Geophysical Research Atmospheres*, 91(A4), 4345–4351. <https://doi.org/10.1029/ja091ia04p04345>
- Kivelson, M. G., & Zu-Yin, P. (1984). The Kelvin-Helmholtz instability on the magnetopause. *Planetary and Space Science*, 32(11), 1335–1341. [https://doi.org/10.1016/0032-0633\(84\)90077-1](https://doi.org/10.1016/0032-0633(84)90077-1)
- Koskinen, H. E. J., & Kilpua, E. K. J. (2021, October). *Physics of Earth's radiation belts*. <https://doi.org/10.1007/978-3-030-82167-8>
- Kozlovskaya, E., & Kozlovsky, A. (2012). Influence of high-latitude geomagnetic pulsations on recordings of broadband force-balanced seismic sensors. *Geoscientific instrumentation, methods and data systems*, 1(2), 85–101. <https://doi.org/10.5194/gi-1-85-2012>
- Laundal, K. M., & Richmond, A. D. (2016). Magnetic Coordinate systems. *Space Science Reviews*, 206(1-4), 27–59. <https://doi.org/10.1007/s11214-016-0275-y>
- Liu, W., Sarris, T. E., Li, X., Elkington, S. R., Ergun, R., Angelopoulos, V., Bonnell, J., & Glassmeier, K. H. (2009). Electric and magnetic field observations of Pc4 and Pc5 pulsations in the inner magnetosphere: A statistical study. *Journal of Geophysical Research Atmospheres*, 114(A12). <https://doi.org/10.1029/2009ja014243>
- Lu, H., Xiaoyu, Y., Haodong, W., Jin, L., Xuejiao, M., & Caihong, Z. (2020). Research on Application of Digital Signal Processing Technology in Communication. *IOP Conference Series Materials Science and Engineering*, 799(1), 012026. <https://doi.org/10.1088/1757-899x/799/1/012026>
- Mayaud, P. N. (1980, January). *Derivation, meaning, and use of geomagnetic indices*. <https://doi.org/10.1029/gm022>
- Moura, S. W. N., Di Carlo Silva Santos, R., Da Silva Picanço, G. A., Teixeira, M. F. B., & Machado, J. R. M. (2023). Analysis of Pc3 And Pc4 Geomagnetic Pulsations over the Amazon Region. *Brazilian Journal of Geophysics*, 41(2). <https://doi.org/10.22564/brjg.v41i2.2302>
- Nykyri, K. (2024). On the Importance of the Kelvin-Helmholtz Instability on Magnetospheric and Solar Wind Dynamics During High Magnetic Shear. *Geophysical Research Letters*, 51(8). <https://doi.org/10.1029/2024gl108605>
- Pitout, F., & Bogdanova, Y. V. (2021). The polar cusp seen by Cluster. *Journal of Geophysical Research Space Physics*, 126(9). <https://doi.org/10.1029/2021ja029582>
- Rabie, E., Hafez, A. G., Saad, O. M., El-Sayed, A.-H. M., Abdelrahman, K., & Al-Otaibi, N. (2020). Geomagnetic micro-pulsation automatic detection via deep learning approach guided with discrete wavelet transform. *Journal of King Saud University - Science*, 33(1), 101263. <https://doi.org/10.1016/j.jksus.2020.101263>
- Regi, M. (2016). Ulf power fluctuations in the solar-wind parameters and their relationship with the relativistic electron flux at the geosynchronous orbit. *Il Nuovo Cimento C*. <https://doi.org/10.1393/ncc/i2016-16285-x>

- Rostoker, G., Akasofu, S.-I., Foster, J., Greenwald, R., Lui, A., Kamide, Y., Kawasaki, K., & McPherron, R. (1980). Magnetospheric substorms - definition and signatures. *Journal of Geophysical Research*, 85, 1663–1668. <https://doi.org/10.1029/JA085iA04p01663>
- Simha C, P., Katlamudi, M. R., & Bulusu, J. (2023). Low latitude pi2 pulsations at desalpar, gujarat, india: A statistical analysis of the influences of magnetic storms/substorms, seasons, and solar cycles. *Journal of Atmospheric and Solar-Terrestrial Physics*, 252, 106145. <https://doi.org/https://doi.org/10.1016/j.jastp.2023.106145>
- Singh, R. (2019, February). *Coupling of the solar driven prolonged and transient processes to the equatorial and low latitude ionosphere* [Doctoral dissertation]. <https://doi.org/10.13140/RG.2.2.29064.55041>
- Sinha, A. K., & Rajaram, R. (2014). Dominance of toroidal oscillations in dawn/dusk sectors: A consequence of solar wind pressure variation. *Earth Planets and Space*, 55(2), 93–104. <https://doi.org/10.1186/bf03351736>
- Sinha, A. K., Yeoman, T. K., Wild, J. A., Wright, D. M., Cowley, S. W. H., & Balogh, A. (2005). Evidence of transverse magnetospheric field line oscillations as observed from Cluster and ground magnetometers. *Annales Geophysicae*, 23(3), 919–929. <https://doi.org/10.5194/angeo-23-919-2005>
- Sisan, D. R., Shew, W. L., & Lathrop, D. P. (2003). Lorentz force effects in magneto-turbulence. *Physics of The Earth and Planetary Interiors*, 135(2-3), 137–159. [https://doi.org/10.1016/s0031-9201\(02\)00212-1](https://doi.org/10.1016/s0031-9201(02)00212-1)
- Song, Y., & Lysak, R. L. (2023). A mechanism of the auroral substorm expansion onset: electric discharge in the double layer. *Frontiers in Astronomy and Space Sciences*, 10. <https://doi.org/10.3389/fspas.2023.1296626>
- Southwood, D. (1968). The hydromagnetic stability of the magnetospheric boundary. *Planetary and Space Science*, 16(5), 587–605. [https://doi.org/10.1016/0032-0633\(68\)90100-1](https://doi.org/10.1016/0032-0633(68)90100-1)
- Takahashi, K., & Heilig, B. (2019). L versus time structures of dayside magnetic pulsations detected by the European Quasi-Meridional Magnetometer Array. *Journal of Geophysical Research Space Physics*, 124(8), 6566–6584. <https://doi.org/10.1029/2019ja026796>
- Tan, L., & Jiang, J. (2013, February). *Digital Signal Processing: Fundamentals and applications*. <http://ci.nii.ac.jp/ncid/BB13248327>
- Thankachan, D. (2019). Innovative trends in digital signal processing. 3, 58–59.
- Thomas, N., Shiokawa, K., & Vichare, G. (2019). Comprehensive study of Low-Latitude PI2 pulsations using observations from multisatellite swarm mission and Global Network of Ground Observatories. *Journal of Geophysical Research Space Physics*, 124(3), 1966–1991. <https://doi.org/10.1029/2018ja026094>
- Uruba, V. (2018). On Reynolds number physical interpretation. *AIP conference proceedings*. <https://doi.org/10.1063/1.5049926>
- Welch, P. (1967). The use of fast Fourier transform for the estimation of power spectra: A method based on time averaging over short, modified periodograms. *IEEE Transactions on Audio and Electroacoustics*, 15(2), 70–73. <https://doi.org/10.1109/tau.1967.1161901>
- Zanandrea, A., Neto, C. R., Rosa, R. R., & Ramos, F. F. (2000). Analysis of geomagnetic pulsations using multi-wavelets spectral and polarization method. *Physica A Statistical Mechanics and its Applications*, 283(1-2), 175–180. [https://doi.org/10.1016/s0378-4371\(00\)00148-5](https://doi.org/10.1016/s0378-4371(00)00148-5)